12-2020

Sparse Bases and Bayesian Inference of Electromagnetic Scattering

John Lee

SPARSE BASES AND BAYESIAN INFERENCE OF ELECTROMAGNETIC SCATTERING

DISSERTATION

John Lee, Contractor, Riverside Research

AFIT-ENG-DS-20-D-010

DEPARTMENT OF THE AIR FORCE
AIR UNIVERSITY

AIR FORCE INSTITUTE OF TECHNOLOGY

Wright-Patterson Air Force Base, Ohio

The views expressed in this dissertation are those of the author and do not reflect the official policy or position of the United States Air Force, the Department of Defense, or the United States Government.

AFIT-ENG-DS-20-D-010

SPARSE BASES AND BAYESIAN INFERENCE OF ELECTROMAGNETIC SCATTERING

DISSERTATION

Presented to the Faculty

Graduate School of Engineering and Management

Air Force Institute of Technology

Air University

Air Education and Training Command

in Partial Fulfillment of the Requirements for the

Degree of Doctor of Philosophy in Electrical Engineering

John Lee, B.S.E.E, M.S.E.E.

Contractor, Riverside Research

December 2020

AFIT-ENG-DS-20-D-010

SPARSE BASES AND BAYESIAN INFERENCE OF ELECTROMAGNETIC SCATTERING

John Lee, B.S.E.E, M.S.E.E.
Contractor, Riverside Research

Committee Membership:

Peter J. Collins, Ph.D.
Chairman

Julie A. Jackson, Ph.D.
Member

Matthew C. Fickus, Ph.D.
Member

Michael A. Marciniak, Ph.D.
Dean's Representative

ADEDEJI B. BADIRU, Ph.D.
Dean, Graduate School of Engineering and Management

Abstract

Many approaches in Computational Electromagnetics (CEM) rely on the decomposition of complex radiation and scattering behavior with a set of basis vectors. Accurate estimation of the quantities of interest can be synthesized through a weighted sum of these vectors. In addition to basis decompositions, sparse signal processing techniques developed in the Compressive Sensing (CS) community can be leveraged when only a small subset of the basis vectors are required to sufficiently represent the quantity of interest. We investigate several concepts in which novel bases are applied to common electromagnetic problems and leverage the sparisty property to improve performance and/or reduce computational burden.

The first concept explores the use of multiple types of scattering primitives to reconstruct scattering patterns of electrically large targets. Using a combination of isotropic point scatterers and wedge diffraction primitives as our bases, a 40% reduction in reconstruction error can be achieved.

Next, a sparse basis is used to improve Direction of Arrival (DOA) estimation. We implement the Block-Sparse Bayesian Learning (BSBL) technique to determine the angle of arrival of multiple incident signals with only a single snapshot of data from an arbitrary arrangement of non-isotropic antennas. This is an improvement over the current state-of-the-art, where restrictions on the antenna type, configuration, and a priori knowledge of the number of signals are often assumed.

Lastly, we investigate the feasibility of a basis set to reconstruct the scattering patterns of electrically small targets. The basis is derived from the Theory of Characteristic Modes (TCM) and can capture non-localized scattering behavior. Preliminary results indicate that this basis may be used in an interpolation and extrapolation scheme to generate scattering patterns over multiple angles.

To Mom, Dad, and the brothers. The American Dream is alive and well.

Acknowledgments

I would like to extend my deepest thanks to my advisor, Dr. Collins, for his guidance and insight. His unwavering encouragement over the last four years was a critical factor in this effort. I would also like to thank the members of the committee, Dr. Jackson and Dr. Fickus, for their dedication to improving the quality of my work. I am truly grateful to the committee's advisement as well as their engaging coursework. Respectively and respectfully, they are AFIT's Knott, Jakowatz, and Strang.

I would also like to thank my colleagues in the New York, Champaign, and Dayton offices for their support and patience. This opportunity would not have been possible without them. I would like to thank Joe S. for providing the spark at the very beginning of this journey and Ron A. for keeping the bar high. I would like to thank my AFIT cohort for their camaraderie and for being great wingmen and wingwomen during my time there.

Lastly, I would like to thank my friends and family for their unconditional support and love.

John Lee

Table of Contents

Page

Abstract iv

Dedication v

Acknowledgments vi

Table of Contents vii

List of Figures ix

List of Tables xiii

List of Acronyms xiv

I. Introduction 1

1.1 Motivation 1
1.2 Problem Statement 2
1.3 Research Overview 5

II. Literature Review 8

2.1 Compressed Sensing 8
2.2 Sparse Representations in ISAR Reconstruction 14
2.3 Bayesian Inference 17
2.4 Theory of Characteristic Modes 21

III. Sparse Representation of Targets with Mixed Scattering Primitives 27

3.1 Optimization Framework 30
3.2 Numerical Experiments 33
3.2.1 Flat Plate 34
3.2.2 Angled Plate 37
3.3 Sparse Reconstruction Considerations for Compressive Sensing 43
3.4 Conclusion 46

Page

IV. Direction of Arrival via Block-Sparse Bayesian Learning with Polarized Non-Uniform Arrays 47

4.1 Introduction 47
4.2 Problem Formulation 49
4.2.1 Snapshot Model for Arbitrary Arrays 49
4.2.2 Steering Vector Orthogonalization (SVO) 50
4.2.3 BCS and BSBL for Complex Weights 51
4.3 Simulation Results 52
4.3.1 Approach 52
4.3.2 SVO Validation 54
4.3.3 Impact of Signal and Array Variations on Steering Vector Orthogonalization (SVO) 56
4.4 Conclusion 60

V. Scattering Interpolation via Theory of Characteristic Modes 62

5.1 Introduction 62
5.2 Theoretical Framework 62
5.3 Methodology 65
5.4 Numerical Experiments and Observations 71
5.4.1 Reference Data Discrepancies 71
5.4.2 Replication of Prior Results 72
5.4.3 RCS Predictions via Eigenvalue Interpolation 77
5.4.4 Mode-Tracking Ambiguities 82
5.4.5 Interpolation and Extrapolation via Characteristic Mode Analysis (CMA) as a Sparse Basis 83
5.5 Areas for Future Investigation 91

VI. Conclusions 94

Appendix A: Scattering Primitives Based on an Approximation to Physical Optics Solutions 99

Appendix B: Non-Linear, Constrained Minimization of Primitive Spatial Parameters 102

List of Figures

Figure Page

1.1 F-16 under test and evaluation in an anechoic chamber [1]. 3

2.1 Recovery of a sparse signal $\mathbf{x}$ with minimal measurements, $\mathbf{y}$ and $\mathbf{A}$. . . 8

2.2 Single-Pixel sensor. Copyright 2007 IEEE [2]. 9

2.3 ISAR image aberrations from a PEC cylindrical cavity [3]. 15

2.4 RCS of PEC sphere as a function of circumference. 22

2.5 Characteristic modes of a plate. 24

3.1 Far-Field approximation of a (a) Isotropic Point Scatterer (IPS) and (b) Wedge Diffraction Primitive (WDP). 29

3.2 Optimization Framework. 31

3.3 Flat plate and angled plate test geometries. 33

3.4 Reference, WDP and IPS solutions for a flat plate (magnitude). Discrepancies between the reference and WDP solution (top) are corrected with an IPS solution (middle) to yield low reconstruction error (bottom). 35

3.5 Relative error norm of the flat plate. 36

3.6 Active IPSs for $\phi \in [0°, 270°]$ (red vectors) and $\phi \in [270°, 360°]$ (green vectors). 38

3.7 Discontinuities in non-dihedral sector of IPS solution due to interior IPS contributions. 39

3.8 Reference, WDP and IPS solutions for an angled plate (magnitude only). Discrepancies between the reference data and WDP solution (top) are corrected with an IPS solution (middle) to yield low reconstruction error (bottom). 40

3.9 Relative error norm of the angled plate. 42

Figure Page

3.10 Robustness of proposed and traditional method solutions for $\lambda/3$ to $\lambda/5$ discretizations of the flat plate. 44

3.11 Robustness of proposed and traditional method solutions for $\lambda/3$ to $\lambda/5$ discretizations of the angled plate. 45

4.1 Reference coordinate system: a notional seven-element linear dipole array has two incident signals $\mathbf{s}_1$ and $\mathbf{s}_2$, with directions θ_1 and θ_2, and polarizations ψ_1 and ψ_2, respectively. 53

4.2 (a) Ideal linear, (b) Perturbed linear, and (c) Perturbed conformal array configurations. Feed locations are projected onto Cartesian planes to indicate the non-uniform separation of the array elements in (b) and (c). 54

4.3 SVO validation: (a) Bayesian Compressive Sensing (BCS) without SVO, (b) BCS with SVO, (c) BSBL without SVO, and (d) BSBL with SVO. Accurate reconstruction is achieved with SVO-BSBL, while others show significant false estimation errors. 56

4.4 Ideal linear array performance, noise variance=0. For SVO-BSBL, accurate DOA estimates are achieved in most angle and polarization permutations except near end-fire and closely separated sectors. 58

4.5 Perturbed linear array performance, noise variance=10^{-3}. DOA estimates improve under both methods, but SVO-BSBL continues to exhibit better performance than SVO-BCS. 59

4.6 Perturbed conformal array performance, noise variance=10^{-3}. Further improvements in DOA estimation are seen in the end-fire and closely separated sectors of the SVO-BSBL result. 60

5.1 NASA Almond geometry. 66

5.2 Trajectory of the first 50 eigenvalues of the NASA Almond. 67

Figure Page

5.3 Characteristic currents of the first mode for (a) 0.5 GHz, (b) 0.525 GHz, (c) 1.2 GHz, (d) 1.225 GHz, (e) 1.975 GHz, and (f) 2 GHz. 68

5.4 Comparison of characteristic fields (magnitude) from the first mode for 0.5, 0.525, 1.2, 1.225, 1.975, and 2 GHz. 69

5.5 Sparsity of significant modes. The number of modes with high modal significance values drops off quickly for all frequencies of interest. 70

5.6 Reference dataset is overpredicting by 20 dB. 71

5.7 CMA reconstruction for 1200MHz using first 16 modes. 73

5.8 RCS predictions from MATLAB (top), CMA reconstructed (middle), and the magnitude difference (bottom). 74

5.9 Radar Cross Section (RCS) Reconstruction with first 24 modes. 75

5.10 RCS Reconstruction with first three modes. 76

5.11 Modal significance for NASA Almond. 76

5.12 Performance of Interpolation of CMA eigenvalues. 78

5.13 Performance of Interpolation of CMA eigenvalues ($\mathbf{E}^i_{\tan}$ recalculated). . . 80

5.14 Comparison of the phase of the characteristic fields from the first (top), second (middle), and third (bottom) modes for 0.5, 0.525, 1.2, 1.225, 1.975, and 2 GHz. 81

5.15 Eigenvalues for NASA Almond. 82

5.16 Ambiguity in mode tracking. 83

5.17 Scattering estimate from CMA-BSBL interpolation (19 uniform samples). 85

5.18 Modal significance estimate from CMA-BSBL interpolation (19 uniform samples). 86

5.19 Scattering estimate from CMA-BSBL interpolation (20 random samples). 87

Figure Page

5.20 Modal significance estimate from CMA-BSBL interpolation (20 random samples). 88

5.21 CMA-BSBL 1.2 GHz extrapolation ($0° - 90°$). 89

5.22 50 trials of CMA-BSBL 1.2 GHz extrapolation ($0° - 90°$). 90

5.23 CMA-BSBL 1.95 GHz extrapolation over one frequency with measurements between $31° - 151°$. 90

5.24 CMA-BSBL 1.95 GHz extrapolation over five frequencies with measurements between $31° - 151°$. 91

A.1 Plate and Dihedral geometry. 99

A.2 MoM vs approximated PO solution of a 2×1 m plate at (top) and 1×1 m dihedral (bottom) at 1GHz, $\phi\phi$ polarization. 101

List of Tables

Table Page

3.1 Relative Error and (total point scatterer count) of $\lambda/3$ discretized geometries 43

List of Acronyms

Acronym	Definition
BCS	Bayesian Compressive Sensing
BPDN	Basis Pursuit Denoising
BSBL	Block-Sparse Bayesian Learning
CEM	Computational Electromagnetics
CMA	Characteristic Mode Analysis
CS	Compressive Sensing
CS	Compressive Sensing
DCT	Discrete Cosine Transform
DOA	Direction of Arrival
DOA	Direction of Arrival
DOD	Department of Defense
ESPRIT	Estimation of Signal Parameters via Rotational Invariance Technique
GTD	Geometrical Theory of Diffraction
IPS	Isotropic Point Scatterer
ISAR	Inverse Synthetic Aperture Radar
LASSO	Least Absolute Shrinkage And Selection Operator
MAP	Maximum a Posteriori
ML	Machine Learning
MMV	Multiple Measurement Vector
MOM	Method of Moments
MP	Matching Pursuit
MRI	Magnetic Resonance Imaging
MUSIC	Multiple Signal Classification

Acronym	Definition
PEC	Perfect Electric Conductor
PO	Physical Optics
RCS	Radar Cross Section
RIP	Restricted Isometry Property
RVM	Relevance Vector Machine
RWG	Rao-Wilton-Glisson
SAR	Synthetic Aperture Radar
SMV	Single Measurement Vector
SVM	Support Vector Machine
SVO	Steering Vector Orthogonalization
TCM	Theory of Characteristic Modes
UTD	Uniform Theory of Diffraction
WDP	Wedge Diffraction Primitive

SPARSE BASES AND BAYESIAN INFERENCE OF ELECTROMAGNETIC SCATTERING

I. Introduction

1.1 Motivation

Radar Cross Section (RCS) reduction is a critical technology for the Department of Defense (DOD) that has provided significant advantages for our military. It has allowed us global access, precision delivery of munitions, and serves as a formidable deterrence to our adversaries. However, stealth is not a static capability. Since the inception of radar, there have been concurrent efforts in developing increasingly effective signature control methods to defeat detection, as well as developing advanced radar systems to detect increasingly elusive threats. This race to mitigate and/or detect these vanishingly small signals has led to many innovations in materials science, radar design, signal processing and a host of other adjacent fields.

Innovations in one field in particular, Computational Electromagnetics (CEM), often come in lockstep with advances in RCS design. Any modern aircraft program with signature control requirements will rely heavily on modeling and simulation to achieve its objectives. As the complexity of aircraft design and the sensitivity of threat radars increased, so too have the demands on the formulations and supporting algorithms that are used to simulate electromagnetic scattering.

The accuracy and tractability of a simulation generally comes at the cost of computational burden; therefore, significant efforts have been made to increase simulation efficiency via code optimization and judicious approximations of the relevant physics of electromagnetic scattering. In some circumstances, the availability

of computational resources can enable higher accuracy predictions, while in others the resources are utilized to generate coarse predictions for larger or more complex designs.

While modeling and simulation offer rapid design iteration, most programs also depend on physical measurements to test and validate these designs. Again, with increasing complexity of aircraft design and capabilities of threat systems, tolerances for modern aircraft are often very tight and require extensive measurements to ensure that a manufactured article performs within specifications and is consistent with results generated from simulations. Given the current state of fabrication, installation, and integration of materials and subsystems, physical measurements are a necessary diagnostic and validation tool, especially during the later stages of a program's acquisition lifecycle.

Incidentally, this requirement leads to the burden of measuring and characterizing objects that have inherently been designed to be nearly undetectable. The U.S. Government funds and maintains testing facilities that have been designed to support the unique needs of DOD programs (see Figure 1.1). Nevertheless, there are a limited number of these facilities and the execution of the requisite measurements can be both time- and cost-prohibitive. These limited resources are an impediment to the lifecycle of many programs because there are no feasible alternatives for validating the performance of a design. As a result, the DOD is frequently seeking methods to expedite the validation process [4].

1.2 Problem Statement

It is clear that the validation of a system relies on accurate measurements of the quantities of interest. Because measurements of the relevant quantities are often intractable, we seek to establish and/or improve on methods where the number

Figure 1.1: F-16 under test and evaluation in an anechoic chamber [1].

of measurements can be minimized. Recently, the CEM community has sought to leverage the developments of sparse signal processing within the Compressive Sensing (CS) community to expand the capabilities and applications of CEM tools. These developments have enabled many innovations in sensor design, defect detection, and the the ability to accurately and reliably reconstruct signals from a very limited number of samples [5]. Applications of traditional CS theory can only be realized if there exists a sparse basis representation of the signal of interest. In order to reliably recover a signal with very few measurements, the signal must also be amenable to a compact representation where only a limited subset of basis vectors is required to adequately represent the signal. Because of this constraint, there has been strong interest in developing efficient bases for relevant electromagnetic quantities of interest.

With respect to improving the efficiency of the measurement and validation process, one notable effort is to use CEM prediction codes to augment the physical measurements that are performed on a radar instrumentation range. Rather than

relying solely on measurements of the physical target from a range, a surrogate CEM model is used to provide predictions for analysis and validation. The critical element to this approach is to synthesize a CEM model that sufficiently represents the physical article. In practice, there are several complications that must be overcome to make this a viable technique and the most effective implementations have leveraged concepts from sparse signal reconstruction and CS to achieve favorable results [6, 7].

It is important to note that the ubiquity of CEM in aircraft system design and the demand for timely results also mean that formulations are often tailored to only address a specific class of problems. For example, the Method of Moments (MOM) approach is a full-wave technique to solve radiation and scattering problems by discretizing the device into a mesh of edge elements and representing the current distribution over the device with basis functions across each edge. The distribution of currents can be solved by enforcing boundary conditions on the total fields and ultimately requires solving a large system of linear equations. Although this method is theoretically accurate at all scales (with respect to the electrical size of the problem), the fidelity afforded by this method is unnecessary at high frequencies where specular scattering is the dominant behavior. Determining the currents on an electrically large body with this method quickly becomes intractable because of the computational cost of solving for the set of linear equations (i.e., inverting or otherwise decomposing a large matrix). Therefore, alternate (and more efficient) asymptotic formulations such as Physical Optics (PO) and Uniform Theory of Diffraction (UTD) are applied instead. An important consequence of this is that a sparse basis may only be applicable for a certain class of problems.

Another effort to minimize validation measurements relates to the subsystems installed on an airframe. Specifically, there exist radar warning systems that require precise antenna placement on the airframe because the underlying Direction of

Arrival (DOA) algorithms require a known (and usually uniform) separation between the antennas. These restrictions may incur time-consuming rework on installation and ultimately increase the time and resources expended on measurement range validation. One way to expedite the validation process is to utilize a more robust DOA algorithm that would relax the design and system integration constraints of these systems.

In conjunction with the efforts to generate electromagnetic predictions from surrogate CEM models of a physical target, we note that frequency domain methods, such as MOM, generally require a full matrix decomposition for every frequency of interest. Intuitively, we assume that the scattering behavior varies smoothly as a function of frequency and that standard interpolation techniques should perform adequately when approximating the scattering response for frequencies that are not computed explicitly. However, certain targets that have strong resonant responses may not be captured well with this approach. An interpolation scheme that takes into account these resonances may be able to provide more accurate results.

1.3 Research Overview

Provided with the context that sparse bases have the potential to address several common problems that are encountered in the measurement and validation process, our research investigates the use of novel bases in three thrust areas. These applications share the overarching theme of leveraging CEM to reduce the burden of physical measurements.

The first thrust area pertains to the field of Synthetic Aperture Radar (SAR) and Inverse Synthetic Aperture Radar (ISAR) imaging. In these radar applications, traditional processing techniques use the backprojection algorithm to translate phase history measurements into downrange and cross-range locations and to synthesize images of the target scene. Under this application, there is an implicit assumption

that all scatterers in the scene behave as isotropic point scatterers. However, in reality, an object's scattering response varies with respect to the incident angle and the returns may not have direct, single-bounce paths back to the sensor. As a result, SAR and ISAR processing may introduce blurs, shadowing effects, and phantom returns into the image.

These imaging artifacts are particularly troublesome when ISAR is implemented in radar ranges. ISAR processing with instrumentation radars is used as a diagnostic tool to locate regions of a target that have significant contributions to the overall signature. Because of this, advanced ISAR processing techniques have been proposed (and implemented) to mitigate these artifacts. One of the most promising approaches utilizes a collection of of scattering primitives to effectively filter out true target returns from nuisance returns. The filtering process is performed via an l_1-minimization process, which favors sparse solutions (solution vectors with very few non-zero elements). The performance of this approach relies heavily on providing bases that can efficiently represent these effects (i.e., canonical scattering behavior and contamination sources); therefore, the development of these types of bases is an active area of research [8]. We investigate the use of several non-isotropic scattering centers as basis sets that are to be used in conjunction with standard isotropic point scatterer basis. These findings were published in [9].

The next thrust area addresses the DOA problem. Here, the goal is to provide an accurate estimate of the angle of arrival of one or more signals impinging on an array of antennas. There is a rich body of relevant literature to this problem [10–19], but to the author's knowledge, many of these approaches suffer from limitations that are not easily overcome when they are applied in practice. Many techniques impose assumptions on the configuration of antennas and the number of simultaneous incident signals. We develop an alternative to these techniques that enables DOA estimation

to be performed with an arbitrary array of polarized, non-isotropic antennas. Sparsity in this case is enforced with the assumption that the number of incident signals is less than the number of discretized sectors of the angle space [20]. These findings will be submitted to IEEE Sensors Journal.

The final thrust addresses the feasibility of representing electrically small scatterers with entire-domain basis functions. As stated previously, the traditional MOM formulation discretizes a target via a mesh and the distribution of current across the edges of the mesh. The advantage to this approach over high frequency methods is that MOM is able to model non-localized scattering behavior caused by surface waves traveling over the body. Literature dating back to the 1970s suggest that the current distributions are not arbitrary and can be further decomposed into discrete resonant distributions [21]. This decomposition, known as the Theory of Characteristic Modes (TCM) and Characteristic Mode Analysis (CMA), has gained interest recently. We provide a preliminary investigation into the feasibility of using these modes as a sparse basis. While our exploration of this basis may also find utility in the first thrust area as another basis, we limit our analysis to the frequency interpolation problem. We demonstrate that the characteristic modes for a common scattering calibration target vary smoothly and interpolate the values to generate scattering patterns for frequencies that were not calculated directly via MOM.

Due to the range of topics covered in these efforts, the organization of this document follows the scholarly article format. We provide an assessment of the literature in each of these areas in Chapter 2. Our contribution in each of the three thrust areas are documented in Chapters 3, 4, and 5. Finally, a summary of our developments and findings, as well as avenues for future investigation are compiled in Chapter 6.

II. Literature Review

2.1 Compressed Sensing

There is an extensive body of literature covering the theory and applications of Compressive Sensing (CS), specifically in computational electromagnetics (a recent review of these applications is summarized in [5]). Fundamentally, CS theory asserts that a sufficiently sparse signal of interest can be recovered with fewer measurements than dictated by the Nyquist-Shannon theorem [22]. This claim has far-reaching implications and can substantially affect every aspect of the signal measurement process in many domains, including how sensors are designed and how the signals are processed into relevant data for analysis.

The key concept of CS begins with a linear model, $\mathbf{y} = \mathbf{A}\mathbf{x}$, and can be represented visually, shown in Figure 2.1, where $\mathbf{y}$ is a vector of measurements

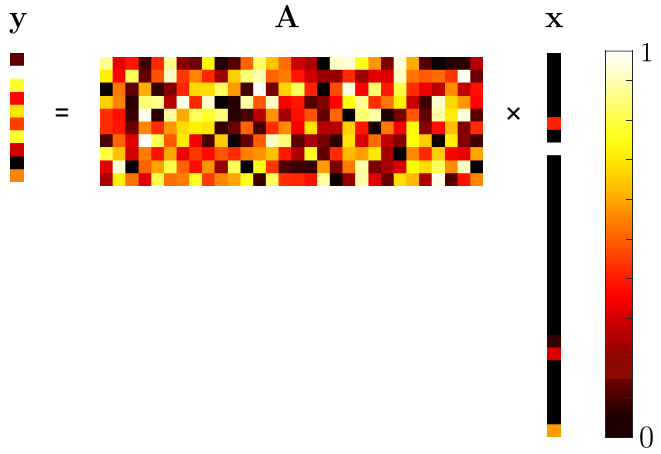

Figure 2.1: Recovery of a sparse signal $\mathbf{x}$ with minimal measurements, $\mathbf{y}$ and $\mathbf{A}$.

that are synthesized from a measurement process represented by $\mathbf{A}$ that operates on a sparse signal $\mathbf{x}$ (and possibly with additive noise, ϵ). From a linear algebra

perspective, a unique solution to $\mathbf{x}$ when given $\mathbf{y}$ and $\mathbf{A}$ is not possible because the system is underdetermined (by definition, $\mathbf{x} = \mathbf{A}^{-1}\mathbf{y}$, but $\mathbf{A}$ is not square and therefore not invertible). While this is true in the general sense, a solution can be recovered when additional constraints are imposed on the composition of $\mathbf{A}$ and $\mathbf{x}$. Namely, $\mathbf{x}$ must be sparse (shown in Figure 2.1 as a vector that consists of mostly zeros) and that $\mathbf{A}$ adheres to the Restricted Isometry Property (RIP) which describes that all subsets (of a certain size) of the columns of $\mathbf{A}$ have a certain degree of orthogonality (shown in Figure 2.1 as a matrix of random values) [23].

The field gained significant attention when seminal works had proven that a signal can be successfully recovered, even in the presence of noise, when the signal is sufficiently sparse and the measurement operator obeys the RIP [24, 25]. This concept was demonstrated experimentally in various contexts, including a single-pixel imaging sensor [26]. The experimental setup, shown in Figure 2.2, uses a digital micromirror device (DMD Array) that is driven by a random number generator (RNG) to reflect light from the scene to a single photodiode. Each combination is recorded as a single measurement and the process is repeated with additional randomly generated arrangements of elements from the mirror array. From these measurements, an image can be reconstructed where the resolution of the image (the number of pixels) exceeds the number of measurements taken.

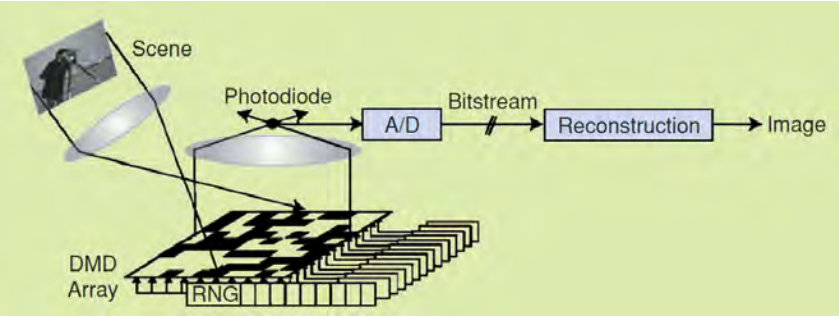

Figure 2.2: Single-Pixel sensor. Copyright 2007 IEEE [2].

The arbitrary selection of mirrors contributing to each measurement is an important aspect of the device as it provides a level of incoherency between the measurements. This is a desirable trait because the incoherency is directly related to the RIP [23] and effectively maximizes the amount of information collected from each measurement. We note that most of the early theoretical work often assumes $\mathbf{A}$ is a random matrix and overlooks the difficulty of creating an appropriate $\mathbf{A}$ that adheres to the RIP. While the single-pixel sensor achieved this by driving the mirror array with a random number generator, an analogous measurement setup would be difficult to achieve in traditional radar applications.

Radar range facilities usually follow a methodical approach in their measurement processes (often a raster scan over the angles of interest) and the signal generators generally only operate with chirped waveforms that sweep the frequencies of interest. Moreover, most radar facilities are only equipped to perform monostatic measurements where the transmitter and receiver are co-located. Further, rotations of the device under test are often limited to a fixed axis of rotation and are intentionally performed slowly so that multiple radar pulses can be processed and integrated together to mitigate noise in the measurements. These restrictions make it particularly difficult to implement a measurement regimen in existing facilities that is amenable to the CS recovery. In light of this, it has been shown through numerical experiments that non-conventional signal waveforms, signal processing techniques, and measurement geometries may offer viable alternatives to estimating electromagnetic quantities of interest [27–29].

Up to this point, the discussion of CS has been limited to what is referred to as the *sampling problem*. That is, the applications thus far have been focused on how measurements are to be performed such that $\mathbf{A}$ adheres to the RIP. A complementary problem is the *recovery problem* which relates to the issue of generating an estimate

of the signal $\mathbf{x}$ after the measurements are collected. A wide variety of approaches exist and the literature in this area tends to focus on developing and characterizing the performance of recovery algorithms used to synthesize these estimates.

The sparsest solution is the $\mathbf{x}$ with the fewest non-zero elements, which can be determined via the l_0 quasi-norm, i.e.:

$$\text{minimize } ||\mathbf{x}||_0 \text{ subject to } \mathbf{Ax} = \mathbf{y} \tag{2.1}$$

where $||\cdot||_0$ represents the norm $(\sum_{i=1}^{N} |x_i|^p)^{1/p}$ with $p \rightarrow 0^+$. However, it has been shown that determining a solution via l_0 minimization is generally an NP-hard problem [23].

Algorithms to determine a sparse solution for $\mathbf{x}$ is an active area of research and is constantly evolving. In one reference [30], the algorithms largely fall into three categories: convex optimization methods (via l_1 optimization), greedy methods, and most recently, Bayesian methods. A large portion of the existing literature that is relevant to our applications of CS principles has historically favored convex optimization over greedy methods. Convex methods have shown to be more resilient to noisy measurements and more robust in cases where $\mathbf{A}$ are not optimally orthogonal (or when the matrix is an overcomplete dictionary) [31]. Greedy methods, such as Matching Pursuit (MP), are iterative methods that select a vector from the basis that maximizes the correlation between the vector and the residual from the previous iteration step.

The popularity of the convex optimization approaches stems from early developments that had indicated the solutions to the l_0 and l_1 minimization problems are equivalent when the solution is sufficiently sparse and $\mathbf{A}$ is sufficiently RIP [32]. With $p = 1$ in Equation (2.1), this result means an intractable NP-hard problem can now be solved in polynomial-time with readily available methods developed by the convex optimization community. The problem is recast as the Basis Pursuit

Denoising (BPDN) problem:

$$\text{minimize } ||\mathbf{x}||_1 \text{ subject to } ||\mathbf{Ax} - \mathbf{y}||_2 \leq \sigma \tag{2.2}$$

where an additional variable σ is introduced as a noise threshold on the measurements, or as the Least Absolute Shrinkage And Selection Operator (LASSO) problem:

$$\text{minimize } ||\mathbf{Ax} - \mathbf{y}||_2 \text{ subject to } ||\mathbf{x}||_1 \leq \tau \tag{2.3}$$

where the additional variable τ is introduced as a sparsity threshold on the estimate [33]. The most popular solvers that we encountered during our literature review are SPGL1 and L1MAGIC, although we note that there are numerous alternatives, including entire software libraries of solvers dedicated to convex optimization and l_1 norm solutions [34–37].

Equally important, convex optimization approaches maintain adequate performance when $\mathbf{A}$ is an overcomplete dictionary. In other words, it is not required for $\mathbf{A}$ to consist of basis vectors that are perfectly orthogonal in order for convex optimization approaches to converge to a solution. In most of the publications relating to Inverse Synthetic Aperture Radar (ISAR) reconstruction via a forward model (the first of our thrust areas), the use of multiple types of primitives requires the use of an overcomplete dictionary and precludes the use of any algorithmic approach other than convex optimization [6]. In the work by Lahaie et al., which we attempt to build upon, they formulate their problem as a BPDN and dictionary editing problem and led us to focusing on the SPGL1 routine exclusively for our efforts in this research area.

Of the three classes of recovery algorithms, the Bayesian methods have seen the most activity in recent literature. These methods assert that estimation can be performed even in the absence of a RIP-compliant $\mathbf{A}$. This further relaxation of the requirements to implement CS principles uses prior knowledge of the sparse

signal distribution to generate sparse solutions [38]. Some of the algorithms under this category include Bayesian Compressive Sensing (BCS) and Block-Sparse Bayesian Learning (BSBL), both of which are derived from work from Tipping and the concept of the Relevance Vector Machine (RVM) [39].

The Bayesian approaches appear to have developed through the confluence of the CS and machine learning communities. We note from the previous assertions that effective application of CS principles may solely rely on the existence of a sparse basis and the pursuit of such bases extend beyond the research area of CS. The general problem of determining more compact representations of data from a given domain is also a critical problem in machine learning, where information from a high-dimensional vector space needs to be distilled with a transformation into a lower-dimensional vector space. In fact, the genesis of RVM relates to a popular, non-Bayesian approach in machine learning, the Support Vector Machine (SVM). These similarities may explain why most of the leading researchers in CS have also made significant contributions in the machine learning literature and vice versa.

We recall the early theoretical developments in CS had not only presumed an $\mathbf{A}$ that complies with the RIP, but that a sparse basis for the signal of interest $\mathbf{x}$ naturally exists, as well. This is readily satisfied in certain radar applications where there are very few targets with respect to the number of bins in the discretized search space, such as search radars and sea-based Synthetic Aperture Radar (SAR) collections in open water. Such instances of natural sparsity can be exploited in a relatively straightforward manner. However, in conjunction with sparse signal transformations, CS principles are applicable in less intuitive situations, as well. This is clear in the domain of natural images, where an intricate image can usually be compressed with the Discrete Cosine Transform (DCT) or wavelet basis (the underpinnings of the

JPEG and JPEG2000 standards, respectively), and imaging with Magnetic Resonance Imaging (MRI).

In practice, the $\mathbf{A}$ matrix represents a measurement process of a quantity in a sparse domain, but if the signal is not naturally sparse, the signal must be transformed into a suitable sparse basis and it must be measured appropriately in that basis. Therefore much of the literature that involves applied research of CS theory decompose the $\mathbf{A}$ matrix as $\mathbf{A} = \mathbf{\Phi\Psi}$, where $\mathbf{\Phi}$ is referred to as the sampling matrix and $\mathbf{\Psi}$ represents the transformation from the sparse basis $\mathbf{x}$. With regard to the Bayesian approaches, the burden then lies in the development of sparse bases $\mathbf{\Psi}$ that can efficiently represent electromagnetic quantities of interest.

2.2 Sparse Representations in ISAR Reconstruction

The developments within the literature have guided the trajectory of our research efforts. The first area of investigation is aimed at providing an additional sparse basis to the overcomplete dictionary approach to ISAR in [6]. This is affirmed by one of their more recent contributions [8] which showed that utilizing additional scattering bases (cavity returns in their study) can improve the performance of their BPDN-based reconstruction technique for removing nuisance returns in ISAR measurements. According to their dictionary-editing process, the measurements are reconstructed via BPDN with an overcomplete dictionary of bases representing scattering and nuisance bases. Once a sparse vector $\mathbf{x}$ is estimated, the nuisance bases are removed from $\mathbf{A}$ and the remaining bases are multiplied with a truncated $\mathbf{x}$ to yield, ideally, a clearer image with contamination from the nuisance sources removed.

Their work pursued a cavity basis due to the fact that cavity returns are not represented well (sparsely) by the isotropic point scatterer basis used for scattering returns. These returns appear as diffuse regions around the feature because multiple reflections of the incident field within the cavity will delay the returns back to the

receiver. The delays are not accurately accounted for in the backprojection algorithm and incorrectly resolves the spatial location of the scattering source. This effect is shown in Figure 2.3 which depicts the Radar Cross Section (RCS) returns from a 12 inch PEC pipe (capped at one end) as a function of aspect angle and range. Aberrations are clearly visible downrange of the pipe when the aperture of the cavity is visible to the transmitter/receiver. Conversely, at aspect angles where the cavity is shielded from direct illumination, the downrange trace shows the expected behavior. Because the energy from the cavity returns is non-localized, it would not be well-characterized with the isotropic point scatterer basis and would be incorrectly associated with one of the nuisance bases in the dictionary instead.

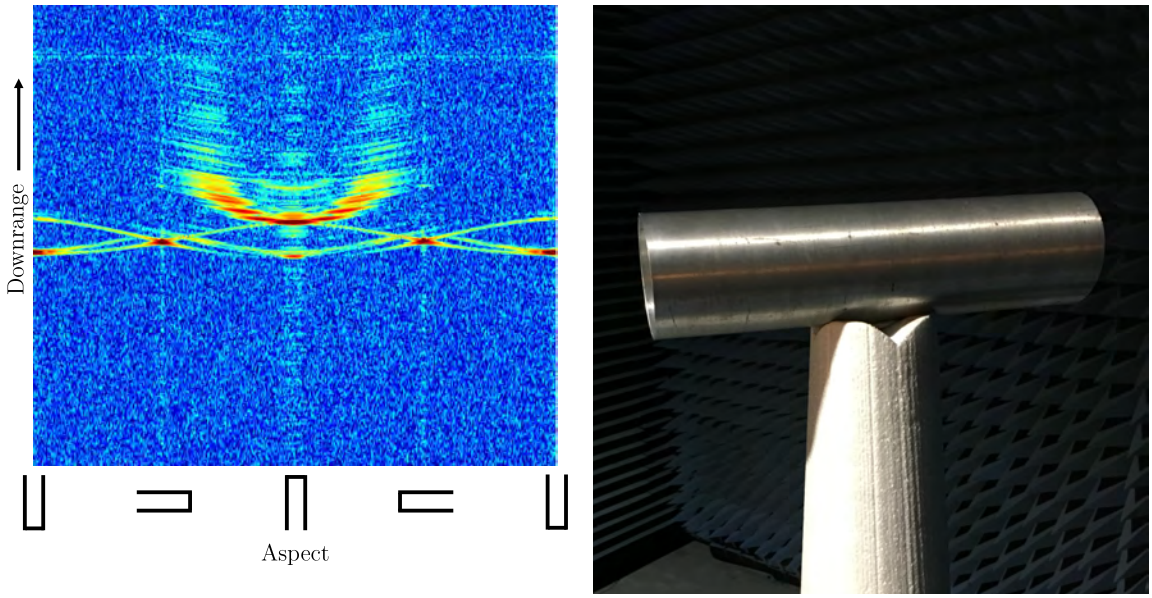

Figure 2.3: ISAR image aberrations from a PEC cylindrical cavity [3].

Similar in intent of the cavity basis development, our efforts in the first thrust area concentrated on developing bases for flat plates and dihedral responses. Their utility extends beyond ISAR image reconstruction and the provenance of this basis

development comes from efforts in the SAR processing and feature extraction communities. There, SAR phase history data is processed to infer properties of targets captured in the scene. This would enable capabilities, such as target and threat identification.

Contributions from [40, 41] were the starting point of our investigation into the feasibility of such a basis, where 3D bistatic scattering center models were developed for a series of canonical geometries. We note that additional developments on feature extraction with these primitives utilized CS principles in [42] (and a similar effort in [43]). They also observed that adherence to the RIP is difficult with the proposed bases and instead appealed to structured dictionaries to overcome this issue. In those efforts, an overcomplete dictionary consists of multiple subdictionaries and the underdetermined system can be regularized by imposing sparsity constraints within a subdictionary. Ultimately, the aim of their approach is slightly different from our ISAR application. In contrast to a blind reconstruction for features embedded in ISAR data, our ISAR reconstruction problem can leverage a priori knowledge of where the scattering centers may be located, which dramatically simplifies the search space and alleviates the issues encountered in a blind reconstruction. Specifically, [7] encodes this a priori information as a cloud of candidate point scatterers that are conformal to the target's exterior surfaces.

The canonical scattering models developed in [41] were based on Physical Optics (PO) theory and our initial investigation used a modified version of these models (simplified to 2D and monostatic) to reconstruct RCS predictions generated from a Method of Moments (MOM) code. These primitives were also used in conjunction with an optimization framework that attempted to estimate the spatial location of the scatterers in the scene. These efforts were met with limited success due to several issues with the validity of the analytic solutions at modest grazing angles and with

how spatially distributed scattering behavior cannot be approximated accurately as localized behavior. These findings are documented in Appendix A and Appendix B where we concluded that an alternative analytic solution should be investigated and the spatial estimation framework should be omitted because it was beyond the scope of our investigation of developing sparse bases.

The subsequent effort, documented in Chapter 3, uses analytic solutions derived from Uniform Theory of Diffraction (UTD) instead of PO from the initial investigation. Analogous to the cavity basis effort, the combination of two scattering primitives — wedge diffraction primitives and isotropic point scatterers — is used to reconstruct far-field monostatic scattering patterns of several target geometries. This combination shows promise in addressing the shortcomings of traditional approaches that only use a single type of primitive (e.g., approximations in analytic solutions, slow convergence). Similar to previous efforts, an l_1-norm minimization technique is applied to determine a set of weights for the point scatterers. We show in Chapter 3 that combining these two types of primitives yields better reconstruction performance than when each primitive type is used individually. We note that our focus of this effort was on the basis development and its feasibility rather than the recovery process or the removal of nuisance returns from measurements. This is due to the fact that replicating the dictionary-editing technique in [7] would also be well beyond the scope of this effort.

2.3 Bayesian Inference

Following the outcome of the first thrust area, we explored alternative recovery methods reported in the literature which emphasized that signal recovery may be possible even if the measurement process does not adhere to the RIP. We build upon the work in [44], where single- and multi-task BCS are implemented to recover the direction of arrival of incident plane waves over an array of antennas. We observe that

the Bayesian treatment of this problem enables key features that previous techniques lacked, such as the ability to generate estimates without a priori knowledge of the number of incident signals and the ability to perform estimates with only a single snapshot of measurements from the antenna array. These are very desirable traits in a Direction of Arrival (DOA) system, especially for radar warning systems as they need to be agile to the number of simultaneous threats and robust enough to generate estimates from sporadic signals.

Fundamentally, the Bayesian approach to generating regression models simply means that the estimates of the independent variables are informed by the dependent variables through their prior distributions. In other words, an estimate of the sparse vector $\mathbf{x}$ is informed by the measurements $\mathbf{y}$. This can be determined through Bayes' theorem where, for clarity, we provide the common terminology for each component:

$$\text{posterior distribution} = \frac{\text{likelihood} \times \text{prior}}{\text{marginal likelihood}} \Leftrightarrow p(\mathbf{x}|\mathbf{y}) = \frac{p(\mathbf{y}|\mathbf{x})p(\mathbf{x})}{p(\mathbf{y})}. \tag{2.4}$$

We see that in Bayesian formalism, all variables in the model are probability distributions rather than single values, indicated with $p(\cdot)$ and conditional distributions with '|'. We can generate a point estimate from the posterior distribution by taking the mode of the posterior distribution, known as the Maximum a Posteriori (MAP) estimate, $\hat{\mathbf{x}}_{\text{MAP}}$:

$$\hat{\mathbf{x}}_{\text{MAP}} = \arg\max_{\mathbf{x}} p(\mathbf{x}|\mathbf{y}) = \arg\max_{\mathbf{x}} p(\mathbf{y}|\mathbf{x})p(\mathbf{x}). \tag{2.5}$$

Because it is the mode of the distribution, $\hat{\mathbf{x}}_{\text{MAP}}$ is the point estimate with the highest likelihood of occurring. We note from Equation (2.5) that calculating the MAP estimate for $\mathbf{x}$ bypasses the need to calculate the denominator, $p(\mathbf{y})$ (i.e., the marginal likelihood). Moreover, $p(\mathbf{x})$ indicates that the $\hat{\mathbf{x}}_{\text{MAP}}$ is dependent on our assumptions of $\mathbf{x}$. Although we can specify any type of distribution for $p(\mathbf{x})$, conjugate priors can make the posterior more straightforward to solve (these types of prior distributions

complement the likelihood distributions such that the posterior distribution is of the same type as the prior distribution). The parameters corresponding to the prior distribution are referred to as hyperparameters. For example, a zero-mean Gaussian distribution would result in

$$p(\mathbf{x}|\alpha) = \prod_{n=1}^{N} \left(\frac{\alpha}{2\pi}\right)^{1/2} \exp\left(-\frac{\alpha}{2}x_n^2\right), \tag{2.6}$$

where α is the inverse variance hyperparameter of the Gaussian distribution. Because Gaussian distributions are self-conjugate, if we apply a Gaussian distribution with the hyperparameter σ^2 to the likelihood function to characterize the noise in the measurements, we are left with a Gaussian posterior distribution

$$p(\mathbf{x}|\mathbf{y}, \alpha, \sigma^2) = \frac{p(\mathbf{y}|\mathbf{x}, \sigma^2)p(\mathbf{x}|\alpha)}{p(\mathbf{y}|\alpha, \sigma^2)}, \tag{2.7}$$

where again the numerator is maximized for a MAP estimate and the denominator can be ignored.

The RVM formulation takes Bayesian principles one step further by calculating the full posterior distribution rather than just the point estimate from MAP. This leads to having to approximate the marginal likelihood, but also factors in the level of uncertainty on the estimates of the weights.

A complete derivation of the RVM technique is provided in [39, 45], where a sparsity promoting prior is applied to $\mathbf{x}$. This is done by applying a Gaussian distribution on $\mathbf{x}$ as before, but with two modifications: each element in $\mathbf{x}$ is an independent distribution with its own hyperparameter ($\boldsymbol{\alpha} = \alpha_1, \ldots, \alpha_M$) and we invoke an additional prior, a hyperprior, over the hyperparameters such that

$$p(\mathbf{x}|\boldsymbol{\alpha}) = \prod_{m=1}^{M} \left(\frac{\alpha_m}{2\pi}\right)^{1/2} \exp\left(-\frac{\alpha_m}{2}x_m^2\right) \tag{2.8}$$

and

$$p(\boldsymbol{\alpha}|a,b) = \prod_{m=1}^{M} \Gamma(\alpha_m|a,b), \tag{2.9}$$

where $\Gamma(\cdot)$ denotes the Gamma distribution with a, b as its parameters. The combination of a Gaussian prior and a Gamma hyperprior yields a Student-t distribution after we marginalize over α_m, which promotes the sparsity on the prior $p(\mathbf{x})$ we are seeking. The results of these developments are leveraged by [46] to formulate BCS as the CS problem of determining a sparse $\mathbf{x}$ into estimating the values for hyperparameters $\boldsymbol{\alpha}$ and σ^2, which equate to the inverse variances for $\mathbf{x}$ and the variance on the additive noise on $\mathbf{y}$.

BSBL, developed by [47], builds from the same theoretical approach as BCS, but offers a more efficient way to generate estimates for the hyperparameters than what was presented in [39]. It also provides the ability to enforce block sparsity within the sparse $\mathbf{x}$. This feature is similar to other non-Bayesian implementations (SPGL1 offers a group sparsity as well as reconstruction where there are multiple measurement vectors [34]), where a priori knowledge of the sparsity structure can be enforced during the optimization process. This is a useful feature in our application of DOA estimation because the measurements from the array are complex-valued. We show in Chapter 4 that enforcing a block structure with the real and imaginary components of the estimation of $\mathbf{x}$ improves its accuracy.

Very recent publications have presented numerical results from implementing BSBL for DOA estimation [48]. The work of Li et al. focused on using linear spatially separated arrays to perform DOA and polarization estimation and found that their approach performed better than other greedy methods (Block Orthogonal Matching Pursuit and Group Basis Pursuit). We note however that their results were generated with an ideal, uniformly spaced array. Moreover, while BSBL can provide estimates

with a single snapshot of voltages from the array, their results are generated using multiple snapshots of data.

In contrast, our concurrent development of this technique leverages findings from [49], a classical subspace method, which proposed that an arbitrarily spaced array can provide adequate DOA estimates via a maximum likelihood method and an orthogonalization of its calibration measurements. Using these developments in conjunction with BSBL allows us to generate accurate DOA estimates without requiring the array to consist of identical and linearly separated elements. This relaxes the requirements of how a DOA array should be constructed and readily accommodates the performance variations that often arise from manufacture and installation.

2.4 Theory of Characteristic Modes

The final effort explores the feasibility of a basis for sparse representation of scattering from electrically small targets. The impetus for this investigation comes from our early observations that the ISAR reconstruction technique from the first thrust area relied on isotropic point scatterers as the primary basis to describe all of the target scattering behavior. Even when supplemented with additional types of primitives, the bases in the dictionary would only be effective at higher frequencies (or where the target is electrically large) because the scattering behavior is spatially localized. It was evident that at lower frequencies, other types of scattering behavior would have a significant contribution to the target's RCS.

Non-localized scattering phenomena (resonant scattering, in particular) become more apparent when the wavelength of the incident field similar to the target's extents. This is well-demonstrated on a PEC sphere, where Figure 2.4 illustrates the RCS for a fixed frequency and the circumference of the sphere is varied from 0.1λ to 100λ. For diameters in the region near 1λ, known as the resonance region for this target,

the incident field has extended interactions with the target, where the scattering is highly dependent on the resonant current distributions over the entire target. The oscillations in the RCS are caused by how well the incident field couples with the structure to excite these resonant modes. At higher frequencies, the fields caused by the currents wrapping around the sphere are shed more rapidly and the specular return becomes the dominant backscattering contribution. As the frequency goes towards infinity, the surface wave contributions are evanescent and the backscatter return only varies as a function of the cross-sectional area of the sphere.

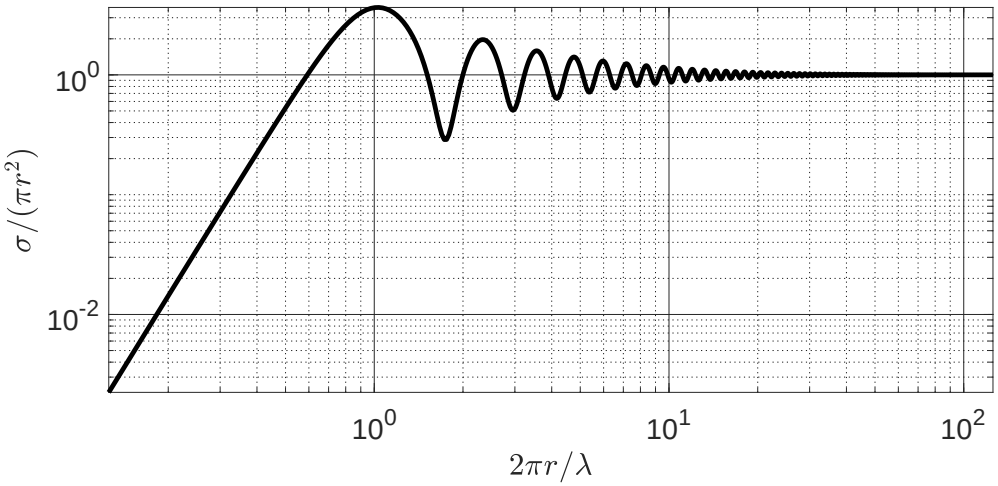

Figure 2.4: RCS of PEC sphere as a function of circumference.

Given that scattering behavior in the resonance region is caused by how the fields interact with extended portions of the target, it is clear that the scattering center approach would not be an effective basis for objects at this scale in terms of electrical size. Whereas the scattering center approach approximates far-field scattering by propagating effects from point sources, scattering caused by surface waves are heavily dependent on the overall geometry of the target. In order to capture these effects via

a basis, each element in the basis must inherently consider the entire shape of the target.

Theory of Characteristic Modes (TCM) provides a decomposition that addresses the aforementioned issues [50]. The theory is an extension of the MOM pioneered by Harrington and starts with the typical impedance matrix formulation of radiation and scattering geometries

$$\mathbf{ZJ} = \mathbf{V} \tag{2.10}$$

where $\mathbf{Z}$ represents the impedance operator, $\mathbf{J}$ represents weights for the currents on the geometry, and $\mathbf{V}$ represents excitation vector. Rather than decomposing the matrix to find an appropriate inversion operator and to ultimately determine scattering and radiation characteristics of the geometry, it was discovered that the real and imaginary components of the impedance matrix can be related via the generalized eigenvalue problem

$$\mathbf{XJ}_n = \lambda_n \mathbf{RJ}_n, \tag{2.11}$$

where $\mathbf{R} = \frac{\mathbf{Z}+\mathbf{Z}^*}{2}$, $\mathbf{X} = \frac{\mathbf{Z}-\mathbf{Z}^*}{2j}$, $\lambda_n = 1 + \nu_n$, $\mathbf{J}_n$ are the eigenvectors and ν_n are the eigenvalues for the nth mode ($n = 1, \ldots, N$ for a structure discretized into N edges). This derivation applies the boundary conditions on perfectly conducting bodies and shows that the impedance matrix defines the relationship between the tangential electric field and the surface currents on the conducting body [51].

Critically, the decomposition of Equation (2.10) into an eigenvalue problem implies that any arbitrarily shaped structure supports discrete current distributions, each defined by an eigenvector and eigenvalue pair. It is assumed that the level of discretization of the structure is sufficient (traditionally at least eight edges per wavelength for uniform meshes) whereby N characteristic current distributions can be calculated. However, this is analogous to the modes supported in a waveguide structure — while the structure can theoretically support an infinite number of modes,

only a subset of these modes are supported for a given frequency. Therefore, each resonant mode will have characteristic current $\mathbf{J}_n$ and corresponding small eigenvalue λ_n (we note that the majority of the Characteristic Mode Analysis (CMA) literature refers to λ_n as the eigenvalues instead of ν_n and that small eigenvalues indicate significant modes rather than large eigenvalues).

To demonstrate, Figure 2.5 illustrates the first nine modes of a rectangular plate. The plots depict the current distribution (in intensity and direction) and indicate

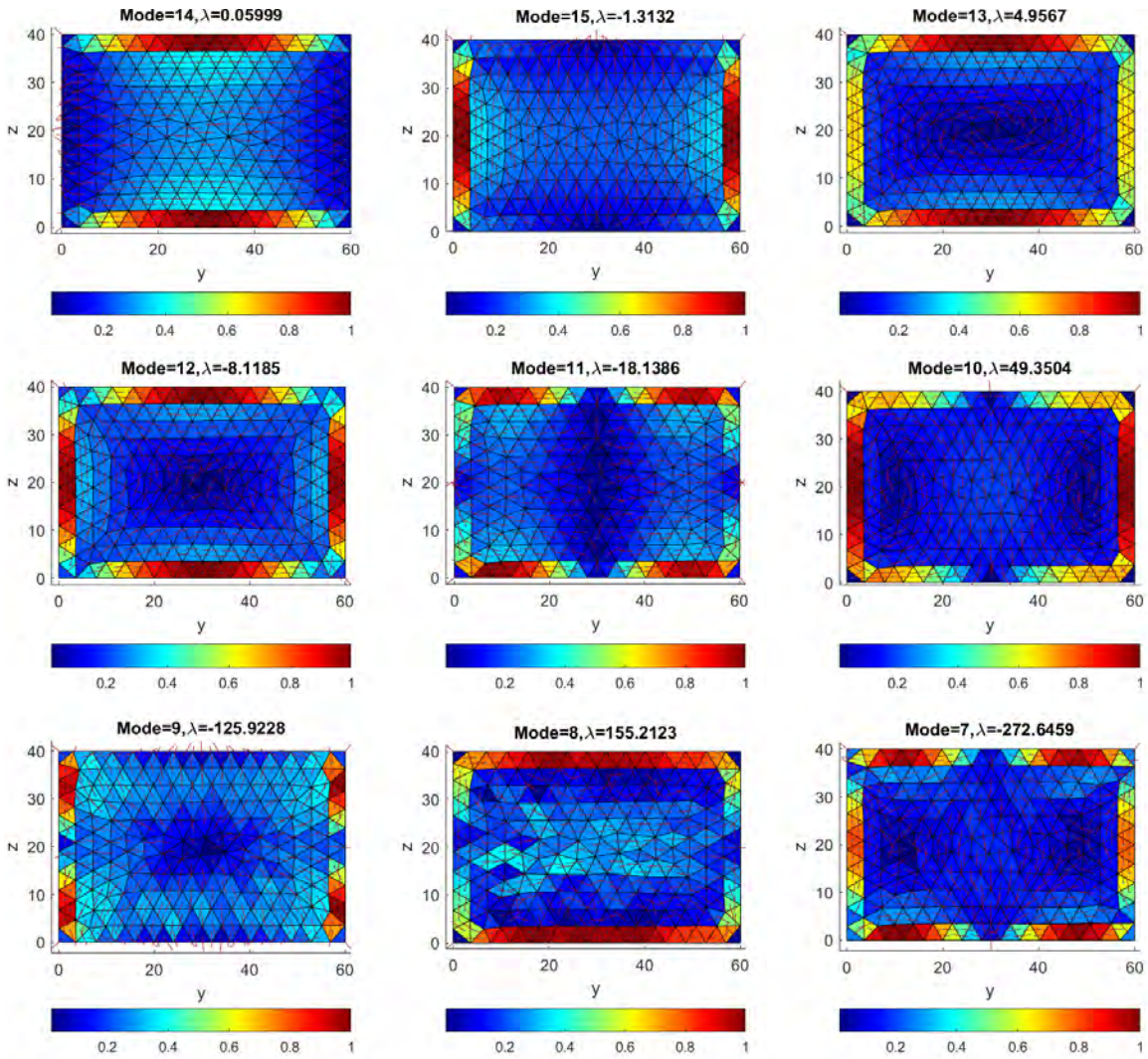

Figure 2.5: Characteristic modes of a plate.

that the distributions are orthogonal (a mathematical proof is provided in [50]). It can be seen that the ninth mode has an eigenvalue several orders of magnitude larger than the first, which indicates a mode that is not easily excited and therefore a small contributor to the overall radiation/scattering. Due to its orthogonality property, this further suggests that a basis can be derived from these distributions. Efforts in [52] show that the RCS can be decomposed into the characteristic fields, $\mathbf{E}_n$ which were derived from $\mathbf{J}_n$. We seek to replicate these results as a first step in determining how this basis could be used to expedite the measurement process.

While we are cognizant of their potential role as a sparse basis in the ISAR effort in the first thrust area, we note that it notably contrasts with the previously developed bases. Specifically, this basis would be tailored to a specific target, since they are derived from the impedance matrix of the discretized body. Given this, the basis may still be used as an element in the dictionary process to improve the performance of noise removal process and particularly useful in identifying defects and discrepancies between the as-measured and as-built scattering targets [6].

Given the constraints of the scope of our research efforts, we recognize that the modal decomposition of a scattering target may be also used to expedite the generation of wideband RCS data. Typical usage of MOM solvers to generate scattering and radiation predictions requires running each discrete frequency of interest individually. This is a time-consuming process since, for every frequency, we must repeat the decomposition of the impedance matrix. Another time-consuming process is the generation of far-field patterns after the decomposition. Each aspect angle is a separate voltage vector (the incident field) that needs to be processed with the decomposed impedance matrix. With a CMA-based approach, we can determine the modal currents with a single impedance matrix and generate data for multiple frequencies by weighting the modal currents with their respective eigenvalues. This

determines the current distribution on the body and is independent of the incident field. RCS can be calculated by determining the coupling between the incident field and the current distribution, which allows for straightforward generation of both monostatic and bistatic quantities.

We observed from the literature that, when evaluated over a range of frequencies, the eigenvalues for some targets have smooth variations and may be defined as continuous functions. This trait makes them more amenable to interpolation and may be a more effective alternative to direct interpolation of the RCS over the same frequency range. Therefore, once the results from [52] are replicated we use the modal plots to generate RCS predictions without directly appealing to the MOM process of decomposing the impedance matrix for every frequency of interest. This would utlimately expedite any application where a MOM code is tasked to generate wideband data, including [6].

III. Sparse Representation of Targets with Mixed Scattering Primitives

It is well known that far-field scattering from a complex geometry can be estimated by decomposing the target into simple scattering primitives and summing their individual responses. Reconstruction of electromagnetic field quantities with Isotropic Point Scatterer (IPS) as a basis is a fundamental principle in Synthetic Aperture Radar (SAR) and Inverse Synthetic Aperture Radar (ISAR) processing [1]. The use of non-isotropic scattering primitives has also been investigated in [2,3]. Moreover, in [4], a dense array of IPSs is used as a part of an overcomplete dictionary. Sparse representations enable discrimination of target returns from nuisance returns that can arise from the measurement process.

In this work, we also seek to reduce the number of scattering centers required by introducing a Wedge Diffraction Primitive (WDP) derived from Geometrical Theory of Diffraction (GTD)/Uniform Theory of Diffraction (UTD) theory. We use the WDP to capture known scattering mechanisms based on the target's far-field pattern and allow the IPSs to recover the remaining coherent differences. We limit the analysis of this approach to planar cuts of 2D geometries and compare the results to reference data generated by a 3D Method of Moments (MOM) code. A normalization factor is applied to translate 2D echo width predictions to 3D Radar Cross Section (RCS).

The use of multiple primitive types is also considered under the context of Compressive Sensing (CS). The theory states that the number of measurements required to successfully recover the sparse representation of a far-field pattern (via Basis Pursuit or other l_1-norm minimization algorithms) decreases substantially (even below the Nyquist sampling rate) as signal sparsity increases [5]. We posit that the sparsity of the far-field pattern representation can be improved by using WDPs to capture diffraction behavior and IPSs to capture the remaining difference between

the diffraction contributions and the original far-field pattern. For example, a large portion of the monostatic response from a 2D flat plate can be accurately represented with two WDPs located at the ends of the plate. In contrast, a solution with two IPSs can only capture the specular response and would require significantly more points to accurately reconstruct the sidelobes of the monostatic return.

While sparsity can be satisfied, the efficacy of this technique as an application for CS is also dependent on the bounds of the Restricted Isometry Property (RIP) of the measurement matrix [6]. Determining these bounds explicitly is an NP-hard problem, but numerical experiments can provide a cursory and empirical assessment of its performance.

In the following sections, we describe the theory behind reconstruction via scattering centers and describe the framework that was developed to perform the reconstruction with a mixed set of primitives. We then present two simple cases to validate our approach, discuss the implications of their results and describe additional areas of investigation.

Consider a collection of spatially distributed scattering centers, each associated with a complex coefficient that modulates its magnitude and phase [7]. By adjusting the location and the complex value of each scattering center, the superposition of every scattering center's far-field response may yield a pattern that matches the far-field response of an arbitrary target geometry. This concept is illustrated in Figure 3.1(a) and concisely summarized as

$$S_{IPS}^{pred}(k, \hat{\mathbf{r}}) = \sum_{n=1}^{N} \gamma_n \exp(-j2k\hat{\mathbf{r}} \cdot \mathbf{r}'_n), \tag{3.1}$$

where S_{IPS}^{pred} is the far-field value synthesized with the wavenumber k and observed from direction $\hat{r}$. S_{IPS}^{pred} is determined by the summation of N IPSs that are located at r'_n and modulated by the complex coefficient γ_n. The components of γ_n control the magnitude and phase delay applied to the IPSs, while the operating frequency

and the

expone

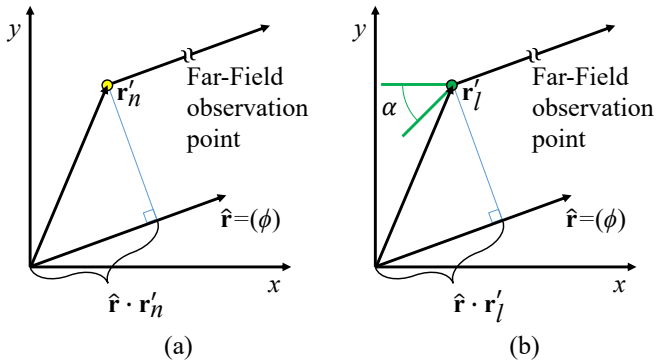

Figure 3.1: Far-Field approximation of a (a) IPS and (b) WDP.

WDPs, shown in Figure 3.1(b), are coherently summed together in a similar fashion as IPSs to generate far-field patterns. From [8], UTD diffraction coefficients reduce to GTD coefficients when the surfaces of the wedge are flat and the observation angles are not in the transition regions near the shadow boundaries. We implement 2D WDPs as

$$D^{s,h}(\phi, m) = \frac{-\exp(j\pi/4)\sin(\pi/m)}{2m\sqrt{2\pi k}} \left[\frac{1}{\cos(\pi/m)} \mp \frac{1}{\cos(\pi/m) - \cos(2\phi/m)} \right], \quad (3.2)$$

where $m = (2\pi - \alpha)/\pi$, α is the wedge angle and ϕ is the monostatic observation angle. In the second term between the brackets, the negative term corresponds to the soft polarization, while the positive term corresponds to the hard polarization (in our case, θ and ϕ polarization, respectively). This 2D analytic solution assumes that the diffraction edge is always aligned along the z-axis and extends towards infinity. The RCS of a finite wedge of width w can be determined by multiplying the 2D echo width by $2\pi w^2/\lambda$, where wavelength $\lambda = 2\pi/k$. The diffraction coefficient $D^{s,h}$ replaces the

IPS coefficient γ_n in (1) and yields

$$S_{WDS}^{pred}(k, \hat{\mathbf{r}}) = \sum_{l=1}^{L} D_l^{s,h} \exp\left(-j2k\hat{\mathbf{r}} \cdot \mathbf{r}_l'\right), \tag{3.3}$$

to generate the far-field monostatic backscatter of the L diffracting wedges.

We note that the formulation in (2) is valid for wedge angles of up to 180° and does not address dihedral effects. Moreover, the scattering pattern arising from WDPs exhibit asymptotic behavior for monostatic angles that are normal to the faces of the wedge due to their vicinity to the shadow boundaries. These singularities occur in pairs for finite length wedges and additional considerations need to be made when geometries contain dihedral or concave regions.

3.1 Optimization Framework

We use the IPS and WDP formulations to estimate a solution S_{FF}^{est} for S_{FF}^{ref} by considering

$$\begin{aligned} S_{FF}^{ref} \approx S_{FF}^{est} &= S_{WDS}^{pred} + \Delta p \\ &= S_{WDS}^{pred} + S_{FF}^{ref} - S_{WDS}^{pred} \\ &= S_{WDS}^{pred} + S_{IPS}^{pred}, \end{aligned} \tag{3.4}$$

where S_{WDS}^{pred} utilizes a priori information about the geometry to generate a coarse estimate of S_{FF}^{ref} and the coherent difference Δp is estimated with S_{IPS}^{pred}. An optimization framework, depicted in Figure 3.2, was designed to determine S_{WDS}^{pred} in a preprocessing stage andS_{IPS}^{pred} with a sparse optimization stage.

The framework was generalized to use a constrained minimization routine to estimate appropriate parameter values for multiple types of non-isotropic scattering primitives (including the WDP utilized in this study). We note that the determination of r_l' and the dependent variables of $D_l^{s,h}$ in (3) can be a non-trivial problem with many local minima, especially when a priori information is limited. Because our investigation is focused on the feasibility of reducing the number of IPSs, we bypass

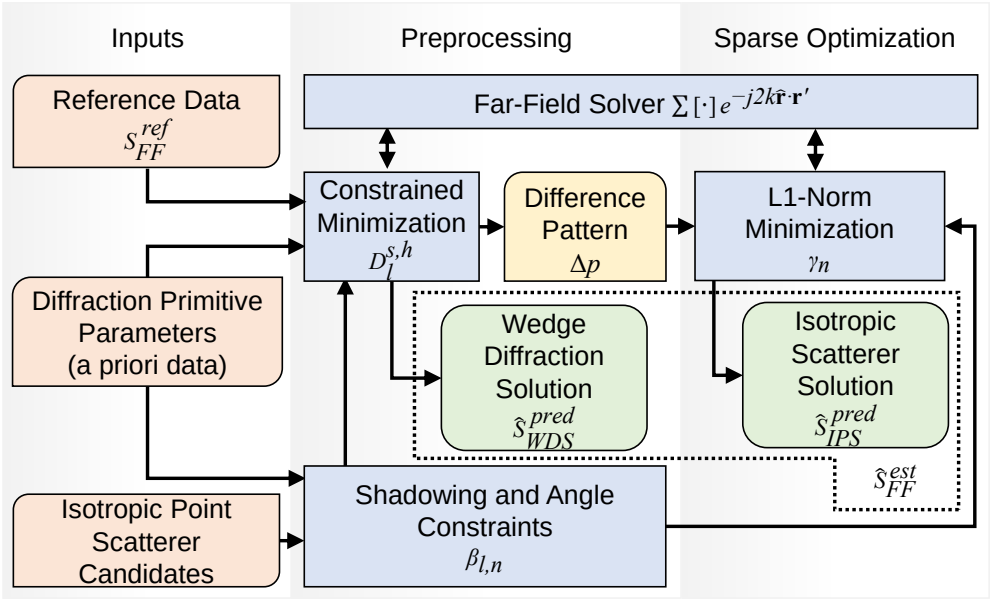

Figure 3.2: Optimization Framework.

the constrained minimization in these experiments and provide parameter values for the WDPs based on a priori knowledge of the scattering geometry as inputs instead.

The preprocessing stage synthesizes a far-field pattern from the WDPs and applies a global phase shift to the prediction that best matches the reference data. This is a necessary step in the event that the reference data and WDP prediction from the analytic geometry have different phase origins. The phase-shifted WDP solution is then coherently subtracted from the S_{FF}^{ref} to yield Δp.

Shadowed regions are also determined in the preprocessing stage of the framework to prevent WDPs and IPSs from radiating through the boundaries of the target geometry. This is performed by tracing a vector from each primitive and scattering center to all far-field observation points and determining whether the ray intersects a facet of the geometry [11].

Modifications to support shadowing and the phase shift of the WDP solution augment the model in (4) with additional modulation terms such that

$$\begin{aligned}\hat{S}_{FF}^{est}(k,\hat{\mathbf{r}}) &= S_{WDS}^{pred} + S_{IPS}^{pred} \\ &= \sum_{l=1}^{L} \beta_l \exp(j\psi) S_{WDS}^{pred} + \sum_{n=1}^{N} \beta_n S_{IPS}^{pred} \\ &= \sum_{l=1}^{L} \beta_l D_l^{s,h} \exp(-j[2k\hat{\mathbf{r}} \cdot \mathbf{r}_l' - \psi]) + \beta_n \gamma_n \exp(-j2k\hat{\mathbf{r}} \cdot \mathbf{r}_n'),\end{aligned} \tag{3.5}$$

where $\beta_{l,n}$ represent the shadowing and angle constraints applied to the WDPs and IPSs respectively and $\exp(j\psi)$ represents the phase shift applied to the WDP solution.

In the sparse optimization stage, determining appropriate values of $\mathbf{r}_n'$ and γ_n in (1) often relies on l_1-norm minimization techniques such as Basis Pursuit Denoising (BPDN) in [4]. We note that BPDN provides a solution that minimizes the sum of the magnitudes of the complex coefficients, whereas an l_0-norm minimized solution minimizes number of complex coefficients contributing to the solution (true sparsity). A solution arising from an l_1-norm minimization routine is a good approximation to the l_0-norm minimized solution when compressive sensing characteristics are met, namely that the dictionary that is used to represent the signal satisfies the RIP. Again, determining adherence to the RIP can be computationally intractable for non-random matrices, therefore we proceed to apply this technique with the understanding that l_1-norm minimized solutions may not strictly be the sparsest solution. In our framework, the SPGL1 library was leveraged to perform the BPDN optimization [9].

We note that primitive-based approaches are popular because generating far-field scattering from the primitives is straightforward. This is a key benefit and allows the optimization routine to iterate more quickly than in alternative approaches [10].

3.2 Numerical Experiments

We first apply our framework on a single flat plate, to demonstrate that the WDPs are implemented correctly and that BPDN can recover an adequate solution to Δp. Next, the framework is applied to an angled plate, which includes a dihedral response that cannot be captured with the WDPs and shall be recovered with the IPSs. Figure 3.3 illustrates the two test geometries that are used to validate our approach.

The flat plate geometry is a 1m $\times$ 0.1m plate with zero thickness, while the angled plate geometry consists of a 1m $\times$ 0.125m and a 0.5m $\times$ 0.125m plate joined at one end to form a 90° angle (the latter dimension of each geometry is used to translate 2D echo width to 3D RCS). While the flat plate has no thickness, two variations of the angled plate were generated: one with zero thickness and one with 0.01m thickness. The significance of the angled plate variations is discussed in Section IV-B.

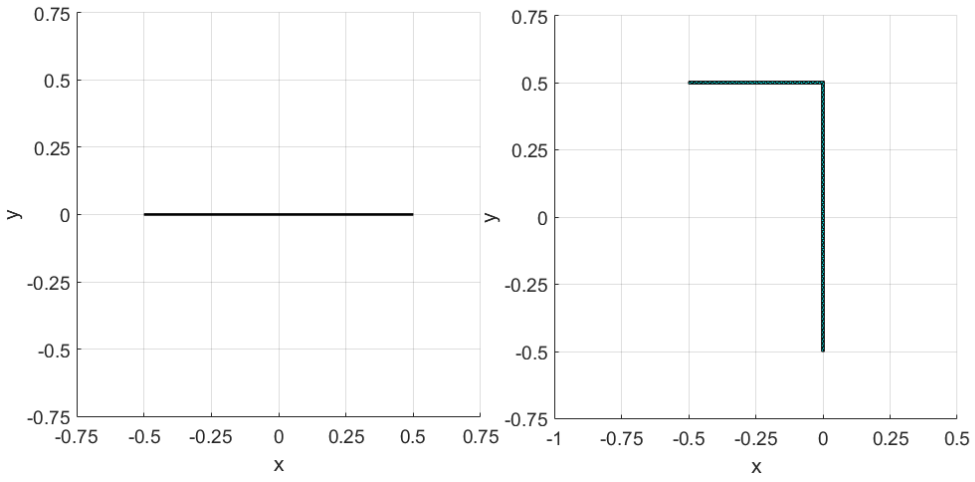

Figure 3.3: Flat plate and angled plate test geometries.

For all cases, only the points on the z=0 plane were used since the far-field patterns were limited to the xy-plane (elevation $\theta = 90°$, azimuth $\phi \in [0°, 360°]$) and there is no variation in either geometry in the z-direction. In all cases, we calculated the TM-polarized far-field backscatter response at 6 GHz ($\lambda = 0.05$m), ensuring that both targets are electrically large and amenable to high frequency approximations. Several mesh discretizations were generated to assess sparsity requirements for a given BPDN solution. Lastly, the BPDN parameters for error tolerance and maximum iterations were set to 10^{-3} and 10^3, respectively, and were held constant over all experiments.

The reference data S_{FF}^{ref} in our comparisons was generated with a MOM-based code to mitigate any contribution from measurement artifacts. We utilize a relative error norm as our metric for comparison, calculated as $\Sigma_{k,\hat{\mathbf{r}}} \left|\left| S_{FF}^{ref} - S_{FF}^{est} \right|\right|_2 / \left|\left| S_{FF}^{ref} \right|\right|_2$, where $\left|\left| \cdot \right|\right|_2$ is the l_2-norm.

3.2.1 Flat Plate.

Figure 3.4 illustrates our results from the flat plate geometry and compares the reference data against our method: the top plot compares the reference data S_{FF}^{ref} against the diffraction solution from the preprocessing stage $\hat{S}_{WDS}^{pred}$ as well as the combined solution $\hat{S}_{FF}^{est} = \hat{S}_{WDS}^{pred} + \hat{S}_{IPS}^{pred}$; the middle plot illustrates the performance of the sparse optimization stage by comparing the IPS solution $\hat{S}_{IPS}^{pred}$ with the difference pattern Δp that the optimization attempts to recover; finally, the bottom plot depicts the coherent difference between S_{FF}^{ref} and $\hat{S}_{FF}^{est}$.

$\hat{S}_{WDS}^{pred}$ was generated by defining two WDPs at the ends of the plate with $\alpha = 0°$. The singularities from each primitive sum to generate the specular lobe at $\phi = 90°$. We observe that the diffraction solution compares well with the reference data until the monostatic angle approaches the grazing angle of the flat plate (a known deficiency

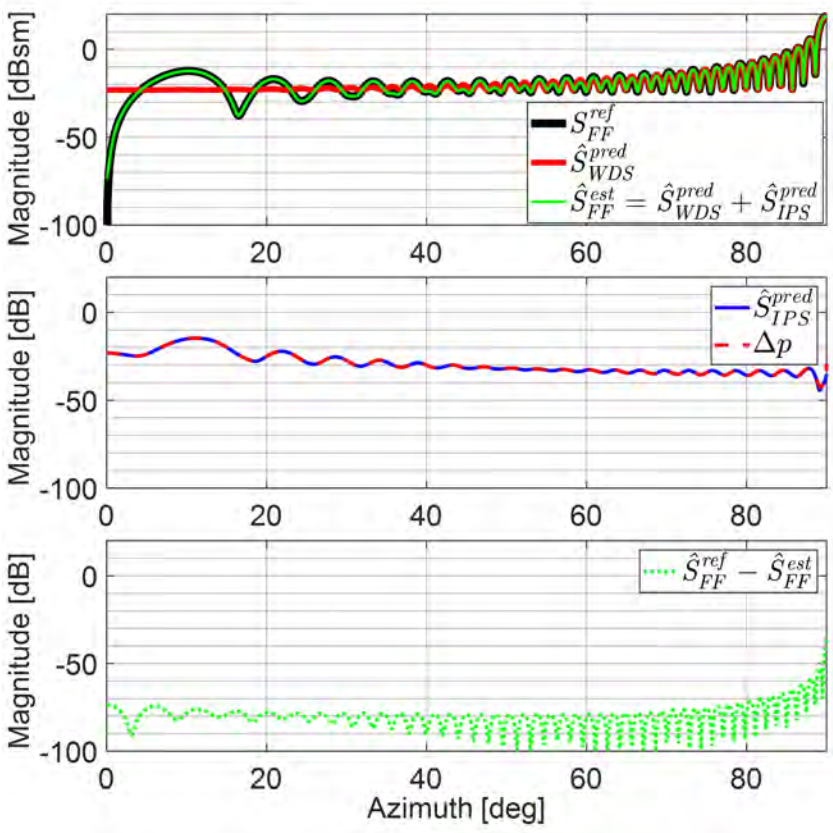

Figure 3.4: Reference, WDP and IPS solutions for a flat plate (magnitude). Discrepancies between the reference and WDP solution (top) are corrected with an IPS solution (middle) to yield low reconstruction error (bottom).

in GTD analytic solutions). The coherent difference from the preprocessing stage stays largely within the -20 and -40 dB range and yields a relative error of 0.0731.

After $\hat{S}_{WDS}^{pred}$is generated, Δp is supplied to BPDN to synthesize $\hat{S}_{IPS}^{pred}$. The result of the sparse optimization stage shows a well-converged solution and has a coherent difference that is largely below -60 dB. When the WDP and IPS solutions are combined to yield $\hat{S}_{FF}^{est}$, we see overlay agreement with S_{FF}^{ref}. The combined solution achieves a relative error of 0.0011.

In contrast to our combined method, traditional scattering center reconstruction of far-field data utilizes IPSs exclusively to reconstruct the reference data rather than the delta pattern. We can assess the efficacy of the traditional approach by calculating the relative error as a function of the number of IPSs used to perform the reconstruction, as shown in Figure 3.5. Using a $\lambda/3$ sampling to generate the IPSs candidates provides $N = 61$ points. We see that both methods require all points to achieve the lowest errors, and the traditional method achieves a relative error of 0.0019, compared to 0.0011 when the combined method is used (the WDP solution does not vary as a function of the number of IPSs).

We also observe that when scattering centers with the smallest magnitudes are removed from contributing to the far-field pattern, the error of the traditional approach increases more quickly than the combined approach. In this example, the traditional approach exceeds the error of the WDP solution when fewer than $N = 60$ points are used for the reconstruction.

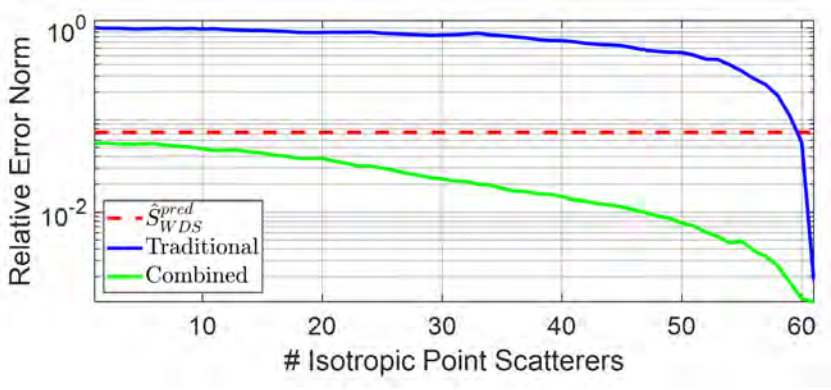

Figure 3.5: Relative error norm of the flat plate.

These results indicate that a solution generated from a combination of WDPs and IPSs can achieve a more accurate reconstruction than either of the two separately.

Moreover, for any desired level of error, the combined solution is sparser than the traditional method.

3.2.2 Angled Plate.

The angled plate geometry provides a more challenging far-field pattern to reconstruct than the flat plate. In addition to the flat plate responses, a strong dihedral response will occur in the far-field azimuth sector $\phi \in (180°, 270°)$. Knowing that the current implementation of WDPs cannot reconstruct the dihedral response, we limit their contributions to angles exclusive of the dihedral sector via β_l in (5).

We note that even with the applied angle constraints, the WDPs may be inaccurate outside of the dihedral region, as well. According to [12], UTD WDPs fail near the shadow boundaries on concave shapes due to the fact that one of the WDPs is shadowed by obstructing geometry. The authors propose a separate type of diffraction coefficient to address dihedral effects by tracking rays that have multiple diffraction and reflection interactions on the target. Without introducing a third type of scattering center into the framework, we apply two additional WDPs located on the shared edge of the two plates (both with $\alpha = 0°$). This is analogous to two independent flat plates, where the additional WDPs complement the primitives on the open edges of the angled plate and compensate for the singularities that arise from those primitives. In total, five WDPs are used: two for each flat plate and one for exterior corner of the angled plate and with $\alpha = 90°$. This arrangement yields a good approximation when compared to the reference data. The relative error norm over the far-field sector where the WDP solution is valid was calculated to be 0.0992 and is similar to the relative error norm achieved by the WDP solution for the flat plate geometry.

We note that IPSs will also encounter issues in pattern reconstruction of the angled plate due to the dihedral sector. We observed that the IPSs on a zero-

thickness angled plate failed to generate an adequate reconstruction since there is a large contrast in the far-field response of the dihedral and non-dihedral regions. Implementing a finite thickness model, shown in Figure 3.6, and enforcing shadow boundaries mitigated these effects: an optimization of the zero thickness geometry resulted in an error of 0.7210, while the finite thickness geometry achieved an error of 0.0477.

However, even with the finite thickness geometry, additional non-physical aberrations are evident in the solution. We can observe the source of these errors by considering the angle sectors where each IPS contributes to the far-field. These sectors are discretized and plotted as vectors in Figure 3.6.

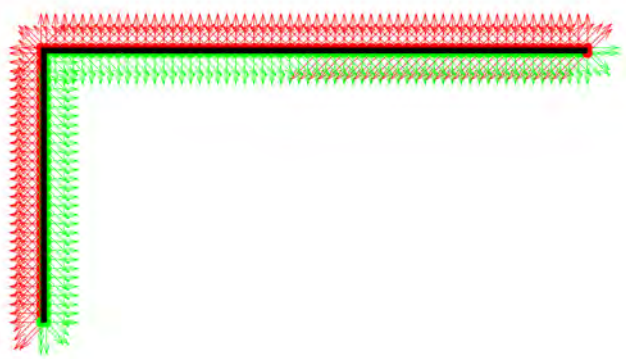

Figure 3.6: Active IPSs for $\phi \in [0°, 270°]$ (red vectors) and $\phi \in [270°, 360°]$ (green vectors).

The figure indicates that there are IPSs located in the interior region of the angled plate that contribute to both the dihedral and non-dihedral sectors of the far-field response. Moreover, the number of interior points contributing to the non-dihedral sector varies as the shadow boundary sweeps across the interior sector of

the angled plate from $\phi \in [116°, 180°]$ and $[270°, 296°]$. This variation causes the discontinuities in the far-field pattern shown in Figure 3.7 and we see that the severity of the discontinuities decrease when the rate of variation decreases, namely when angle approaches either of the normal incident angles ($\phi = 180°$ and $270°$).

If the IPSs from the finite thickness model are used in the proposed method to reconstruct Δp for the entire azimuth range $\phi \in [0°, 360°]$, these discontinuities significantly degrade the reconstruction in the regions where the $\hat{S}^{pred}_{WDS}$ is already very good: under this arrangement, the method achieves a relative error norm of 0.0964 (0.0905 for $\lambda/4$, 0.0830 for $\lambda/5$). While it is a slight improvement over the solution generated by WDPs alone, it does not provide a better solution than the traditional method. We speculate that, in addition to the discontinuities, the dynamic range of the delta pattern increases because the WDPs are restricted from contributing to the dihedral sector of S^{ref}_{FF}. These effects ultimately make Δp more difficult to reconstruct with IPSs.

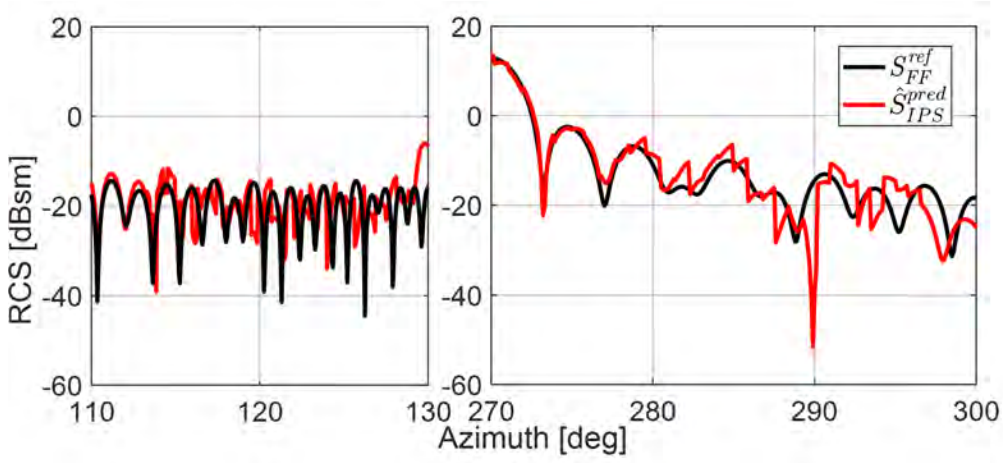

Figure 3.7: Discontinuities in non-dihedral sector of IPS solution due to interior IPS contributions.

As an alternative, we enforce additional constraints on the finite thickness model via β_n such that the interior and exterior IPSs only contribute to the non-dihedral and dihedral sectors, respectively. Using this strict separation, $\hat{S}_{FF}^{est}$ from the combined method yields an improved relative error norm of 0.0238 and exceeds the performance of the traditional method. The results of this experiment are shown in Figure 3.8.

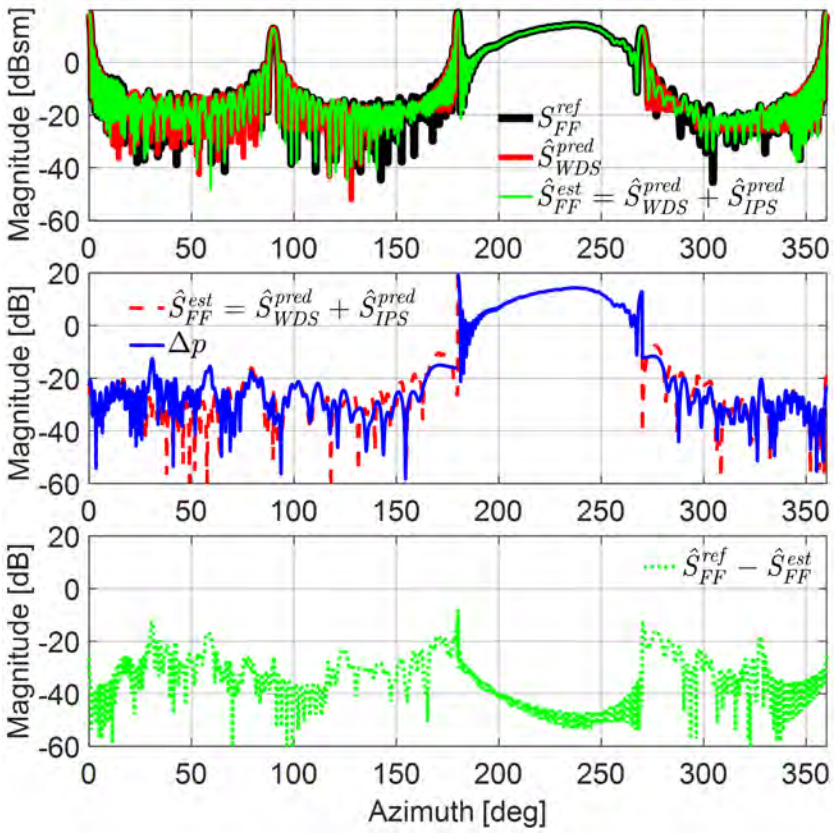

Figure 3.8: Reference, WDP and IPS solutions for an angled plate (magnitude only). Discrepancies between the reference data and WDP solution (top) are corrected with an IPS solution (middle) to yield low reconstruction error (bottom).

The figure also clearly shows the large dynamic range of Δp where much of the dihedral sector stays above 0 dB and non-dihedral sector stays largely below -20 dB.

With our proposed method of synthesizing $\hat{S}_{FF}^{est}$, the errors achieved mostly fall below -20 dB.

Mirroring the analysis performed on the flat plate, we assess the trade between relative error norm and the number of IPSs used in the reconstruction of S_{FF}^{ref} and Δp, shown in Figure 3.9. We note that the figure includes an additional dataset to show that, while the strict separation of the contributions of the inner IPSs to the dihedral sector and the outer IPSs to the non-dihedral sector was an effective strategy for synthesizing Δp, it was not effective when the IPSs were used to reconstruct S_{FF}^{ref}. We speculate that the configuration that enforces strict separation does not provide an adequate number of IPSs to generate the narrow lobes that are present near the edges of the dihedral region in the far-field reference pattern. Conversely, the more permissive shadowing scheme provides enough of these point scatterers to generate narrow (but discontinuous) peaks to match the far-field reference pattern well, but detrimentally impacts the solution when they are used to match Δp (which has lower and wider lobes).

We also observe a discontinuity in the solutions that rely exclusively on IPSs whereas the flat plate tests exhibited a monotonically decreasing error. This is because the magnitudes of the coefficients supporting the dihedral sector are significantly higher than those supporting the non-dihedral sector. For example, in the test case where Δp was recovered via IPSs only, the removal of the lowest magnitude coefficients from reconstruction will incrementally degrade the non-dihedral sector and only after the 39th largest coefficient is removed will the dihedral reconstruction degrade.

Overall, the results are consistent with those in the flat plate experiment. That is, the traditional approach that utilizes only IPSs to reconstruct far-field reference data is unable to reach the error levels that are achieved with the proposed approach. Moreover, if the smallest (in magnitude) non-zero coefficients are discarded from the

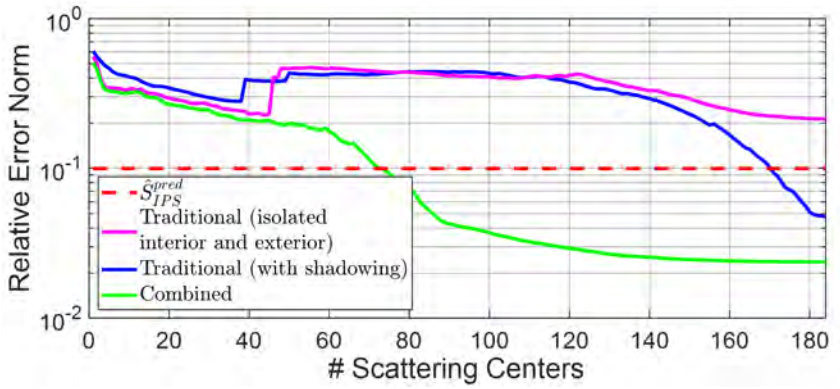

Figure 3.9: Relative error norm of the angled plate.

reconstruction, the degradation of the solution from the proposed method is more gradual than the traditional method.

Our numerical experiments are summarized in Table 1. We see with both geometries that a lower error is achieved when combining a WDP solution with an IPS solution to the delta pattern instead of the relying exclusively on WDPs or IPSs to reconstruct the far-field data. In the case of the angled plate, the result required manually setting boundaries on the range of angles where each primitive type contributes to the far-field pattern. Nonetheless, this is a valuable insight—if the primary goal is to find a compact representation of far-field data, this approach would prove to be very useful. With the proposed method, we can achieve a lower error with approximately the same number of point scatterers (WDPs and IPSs). Likewise, we have solutions that degrade more slowly with respect to how many IPSs are used to reconstruct the pattern when the IPSs are applied to a delta pattern rather than the far-field data.

Table 3.1: Relative Error and (total point scatterer count) of $\lambda/3$ discretized geometries

	Flat Plate	Angled Plate*
WDS Only	0.0731 (2)	0.0992 (5)
IPS Only	0.0019 (61)	0.0477 (184)
Combined	0.0011 (63)	0.0238 (189)

*WDS case evaluated for non-dihedral sector only.

3.3 Sparse Reconstruction Considerations for Compressive Sensing

In addition to investigating the reconstruction accuracy of the proposed method, we seek to understand how well IPSs perform as a sparse basis in the context of CS. With both the flat plate and angled plate geometries, we tested for solution convergence and robustness. Figure 3.10 depicts the results from multiple discretizations of the flat plate geometry and how their solutions degrade as the weakest scattering centers are incrementally removed from the solution.

CS literature states that the recovery of signal is robust to noise and reconstruction accuracy should degrade gracefully with a given basis set due to the RIP (more specifically, the Null Space Property) [13]. We can see that the IPS basis can used to reconstruct Δp in the proposed method and reconstruct S_{FF}^{ref} in the standard method. We noted previously that the degradation of $\hat{S}_{FF}^{est}$ in the proposed method is more gradual than the far-field reconstruction in the standard method and we see that this remains true for other discretizations as well. However, the data also indicates that the solutions generated by the BPDN are not optimally sparse. The delta pattern and far-field pattern do not vary with respect to discretization, yet the number of IPSs required to reconstruct those patterns does vary with respect to discretization.

We also observe that the numbers of candidate IPSs are $N = 61$, 81 and 101 for $\lambda/3$, $\lambda/4$ and $\lambda/5$, respectively. At 6 GHz, the plate is 20λ long and the solutions are effectively using all of the available scattering centers to determine a solution, even though it is known that a sparser solution exists (because the coarse discretizations are able to recover an equally accurate solution with fewer IPSs). While BPDN determines solutions with the smallest $\sum_n |\gamma_n|$, it does not guarantee a solution that minimizes the cardinality of γ unless other CS criteria are met. These findings suggest that a basis set from IPSs does not satisfy the RIP.

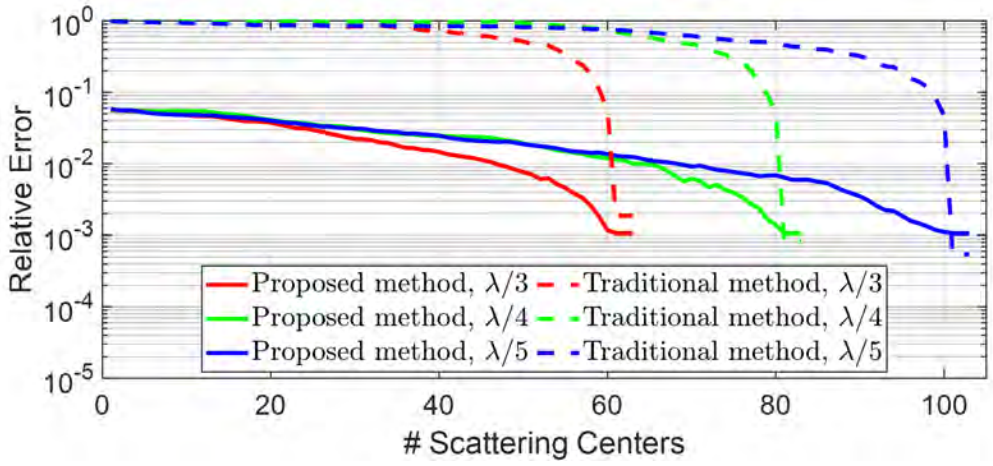

Figure 3.10: Robustness of proposed and traditional method solutions for $\lambda/3$ to $\lambda/5$ discretizations of the flat plate.

A similar analysis is performed on the data for the angled plate dihedral region, depicted in Figure 3.11. Again, the number of IPSs required to reach a given level of error depends on the number of available IPSs. The rate of degradation is different from the flat plate case, however: the presence of longer tails on the reconstructions with the proposed method suggest that they have converged and while they are not

ideal and optimally sparse solutions, they seem to be sparser and more robust than the reconstructions with the traditional method.

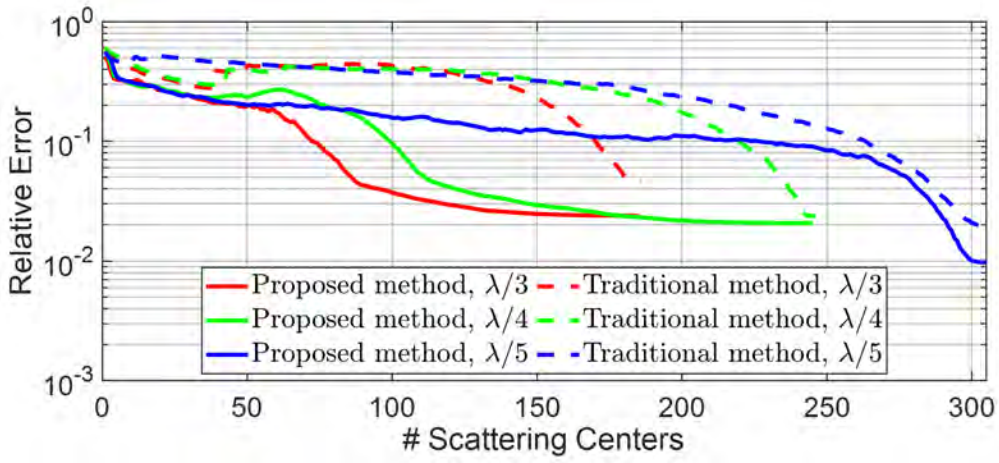

Figure 3.11: Robustness of proposed and traditional method solutions for $\lambda/3$ to $\lambda/5$ discretizations of the angled plate.

These numerical experiments show that, while the technique is successful in generating point scatterer based (WDP and IPS) representations of the targets, there may be limited utility as a basis for compressive sensing applications. The results show empirically that when a sparse representation of the target is used to generate far-field patterns (the traditional approach), perturbations in the sparse representation will introduce excessively large errors for the purpose of interpolation and extrapolation. The sparsity is slightly improved when IPS are employed to reconstruct delta patterns (the proposed approach), but their efficacy seems to be geometry dependent.

These initial results reveal areas that merit additional investigation. It would be prudent to integrate solutions for dihedral scattering mechanisms [14] into the framework which would allow the IPSs to recover a more simplified delta pattern. Additionally, we observed that the number of shadowed IPSs can vary rapidly

and would introduce unwanted discontinuities in synthesized solution. Tapering or adjusting the angles that an IPS contributes to may address this issue and would improve how the IPSs perform on concave targets. Lastly, the optimization framework can be expanded to support multiple frequencies, multiple polarizations, non-planar observation geometries and bistatic quantities to possibly aid the convergence of the optimization routines and expand its applicability to a wider variety of test cases.

3.4 Conclusion

Using WDPs in conjunction with IPSs to reconstruct far-field patterns shows merit in simple cases and when they are applied judiciously. In our numerical experiments, we show that this approach can reduce the overall number of scattering centers required to replicate the scattering response of a flat and a right-angled plate. We also observed that l1-norm minimization techniques may have difficulty finding maximally sparse solutions when IPSs are used as a basis set. Despite this, synthesized solutions are more robust when they are used to reconstruct a coherent difference pattern rather than the far-field data.

IV. Direction of Arrival via Block-Sparse Bayesian Learning with Polarized Non-Uniform Arrays

In this thrust we address the area of improving Direction of Arrival (DOA) performance. It was observed empirically that the basis developed in the first thrust likely does not satisfy the Restricted Isometry Property (RIP). An alternative approach to solving Compressive Sensing (CS) recovery problems asserts that Bayesian inference can be leveraged to bypass the need for the linear system to be RIP [5, 46]. We use this concept as a foundation for extending the utility of current DOA algorithms.

Orthogonalized basis vectors are used in lieu of steering vectors to improve the performance of Direction of Arrival (DOA) estimation. The proposed method overcomes several limitations of current state-of-the-art techniques: it allows the estimation of multiple simultaneous signals (an improvement over some Maximum Likelihood methods [49]), single-snapshot estimation with no a priori knowledge of the number of incident signals (an improvement over subspace methods [53]), estimation of polarized incident signals with non-isotropic array elements (an improvement over Bayesian Compressive Sensing [44]), and estimation with arrays of arbitrary configuration (an improvement over Sparse Bayesian Learning [54]). Computational simulations show good performance in DOA estimation when coupled with a Block-Sparse Bayesian Learning (BSBL) algorithm.

4.1 Introduction

Accurate and reliable DOA estimation has important applications in many fields, including communications and radar systems. These systems operate in increasingly challenging environments and must estimate the direction of multiple arbitrarily polarized incident signals without prior knowledge of the number of incoming signals

and with as few measurements as possible. Moreover, the sensing array may consist of antenna elements that have complex gain patterns and the elements of the array may deviate from their as-designed specifications due to manufacturing tolerances. While some of these issues have been addressed individually in the literature, none have addressed them collectively.

We propose an approach that addresses the aforementioned issues by combining aspects from several existing techniques. Many research efforts that consider the DOA estimation problem appeal to either subspace methods or, more recently, sparse methods derived from CS. Estimation via subspace methods such as Multiple Signal Classification (MUSIC) [10–13], Estimation of Signal Parameters via Rotational Invariance Technique (ESPRIT) [14–16], and Machine Learning (ML) [17–19] assume that the number of incident signals is less than the number of available measurements [53]. Conversely, sparse methods such as Bayesian Compressive Sensing (BCS) [44, 55–57] and Block-Sparse Bayesian Learning (BSBL) [47, 58, 59] only assume that the number of incident signals is less than the number of discretized sectors of the angle space [20]. Recent efforts propose a multi-resolution strategy to iteratively refine the DOA sectors to increase the accuracy and precision of the DOA estimates [60]. In our work, we incorporate an orthogonolization process derived from an ML approach [49] into BCS and BSBL. This modification, which we refer to as Steering Vector Orthogonalization (SVO), extends the utility of CS-based methods by enabling DOA estimates of polarized incident signals with an arbitrary configuration of array elements.

To date, few publications investigate the feasibility of sparse methods when applied to non-uniform arrays or arrays with non-isotropic antenna elements [48]. Our work demonstrates via computational simulations of SVO-enabled BCS and BSBL that the modified BSBL approach has superior performance in DOA estimation. The

next section describes our approach as a series of modifications to the generic snapshot model that is the basis for nearly all DOA techniques. The formulation section is then followed by simulation results, an assessment of algorithm performance, and suggestions for additional areas of investigation.

4.2 Problem Formulation

4.2.1 Snapshot Model for Arbitrary Arrays.

For an arbitrary array of M antenna elements and K incident signals, a single snapshot of measurements, $\mathbf{y} \in \mathbb{C}^{M\times 1}$, is a vector of voltage values from the feeds of each antenna element and is represented as

$$\mathbf{y} = \mathbf{\Phi}(\boldsymbol{\theta})\mathbf{x} + \mathbf{n}, \tag{4.1}$$

where $\boldsymbol{\theta}$=$[\theta_1, \ldots, \theta_N]$ is a set of DOA angles, $\mathbf{\Phi}(\boldsymbol{\theta}) \in \mathbb{C}^{M\times N}$ is a collection of $M\times 1$ steering vectors for those angles, $\mathbf{x} \in \mathbb{C}^{N\times 1}$ is a sparse vector with K non-zero values, and $\mathbf{n} \in \mathbb{C}^{M\times 1}$ is white Gaussian noise. Every DOA technique generates an estimate $\hat{\mathbf{x}}$ such that $\mathbf{\Phi}(\theta)\hat{\mathbf{x}}$ approximates $\mathbf{y}$ and is, ideally, also K-sparse with non-zero elements corresponding to the incident DOA angles in $\boldsymbol{\theta}$. In an arbitrary array, each element may have different gain and performance characteristics. Therefore, the first modification to the snapshot model is to represent the n=$[1, \ldots, N]$ steering vectors as

$$\mathbf{\Phi}(\theta_n) = \mathbf{g}(\theta_n) \odot \begin{bmatrix} \exp(\frac{j2\pi}{\lambda}\mathbf{r}_1\mathbf{s}(\theta_n)) \\ \vdots \\ \exp(\frac{j2\pi}{\lambda}\mathbf{r}_M\mathbf{s}(\theta_n)) \end{bmatrix}, \tag{4.2}$$

where $\odot$ is the Hadamard product, $\mathbf{g} \in \mathbb{C}^{M\times 1}$ accounts for the gain patterns for the M antennas, $\mathbf{r}_m$ for m =$[1, \ldots, M]$ is the position vector of the mth array element, and $\mathbf{s}(\theta_n)$ is the unit vector of a signal originating from the direction θ_n. $\mathbf{\Phi}(\theta)$ can

be determined through simulation or, when unknown perturbations of the antenna elements are present, via calibration by illuminating the array with a known signal.

4.2.2 Steering Vector Orthogonalization (SVO).

Per [17], the snapshot model is construed as a weighted sum of two voltage vectors generated from two known polarizations. That is, an incident planar field originating from θ_n and with polarization ψ can be represented as the sum of two complex-weighted DOA vectors from θ_n with orthogonal polarizations. Further, [49] demonstrates that the DOA vectors can be recast as an arbitrary pair of orthogonalized basis vectors. This implies that calibration via orthogonal polarizations is unnecessary and an orthogonal basis can be generated as a post-processing step. In our implementation, we utilize QR factorization to generate orthogonal vectors. With these changes, the second modification to (4.1) leads to

$$\mathbf{y} = \begin{bmatrix} \mathbf{U}_1(\boldsymbol{\theta}) & \mathbf{U}_2(\boldsymbol{\theta}) \end{bmatrix} \begin{bmatrix} \mathbf{x}_1 \\ \\ \mathbf{x}_2 \end{bmatrix} + \mathbf{n}, \tag{4.3}$$

where $\mathbf{U}_1(\boldsymbol{\theta}), \mathbf{U}_2(\boldsymbol{\theta}) \in \mathbb{C}^{M \times N}$ are arrays of the orthogonalized steering vectors (which span the same subspace as the original set of vectors) and $\mathbf{x}_1, \mathbf{x}_2 \in \mathbb{C}^{N \times 1}$ are K-sparse weight vectors. Ultimately, this orthogonalization and stacking procedure allows the signal model to describe an arbitrarily polarized incident planar field. The problem posed is to determine a sparse solution $\hat{\mathbf{x}}_1$ and $\hat{\mathbf{x}}_2$ that satisfies (4.3).

Sparse methods exploit the assumption of a K-sparse weight vector to generate solutions for linear systems that would otherwise be under-determined and ill-posed. Specifically, the Bayesian interpretation of CS is to determine the posterior distribution for each value in $\mathbf{x}$ through the likelihood function of $\mathbf{y}$ and a sparse prior on $\mathbf{x}$. We leverage the BCS routine from [61] which implements an efficient Relevance Vector Machine (RVM) algorithm. The technique solves for the posteriors by marginalizing over $\mathbf{x}$ and determining values for its hyperparameters instead [39]. As

noted in their work, and counter to traditional Bayesian theory, the marginalization of $\mathbf{x}$ also mitigates the need for informed (non-uniform) hyperpriors.

The BSBL approach has a similar provenance as BCS and also relies on the marginalization of $\mathbf{x}$. Variations of CS exist that exploit the commonality between multiple vectors of $\mathbf{y}$ to determine a sparse solution of $\mathbf{x}$. In particular, [47] reinterprets Multiple Measurement Vector (MMV) as a Single Measurement Vector (SMV) problem and enforces sparsity over groups within a single $\mathbf{x}$. With respect to (4.3), $\mathbf{x}_1$ and $\mathbf{x}_2$ should share the same sparsity pattern under most circumstances. That is, the indices of the non-zero values in $\mathbf{x}_1$ and $\mathbf{x}_2$ should be identical and therefore and can be taken advantage of by BSBL. We note that this assumption may fail when the polarization of an incident signal is perfectly aligned with one of the two orthogonalized basis vectors. While the likelihood of this occurring is low (especially when the antenna elements have non-uniform perturbations in their orientations), we reconcile the two solutions such that $\hat{\mathbf{x}}(n) = \max\left(|\hat{\mathbf{x}}_1(n)|, |\hat{\mathbf{x}}_2(n)|\right)$.

4.2.3 BCS and BSBL for Complex Weights.

A third modification to (4.1) is made to accommodate the BCS and BSBL formulations. Because the standard implementations only support real-valued weight vectors [47, 55], the arrays from (4.3) are recast such that, for $\alpha = [1, 2]$,

$$\mathbf{U}_\alpha(\boldsymbol{\theta}) = \begin{bmatrix} \mathrm{Re}(\mathbf{U}_\alpha(\boldsymbol{\theta})) & -\mathrm{Im}(\mathbf{U}_\alpha(\boldsymbol{\theta})) \\ \mathrm{Im}(\mathbf{U}_\alpha(\boldsymbol{\theta})) & \mathrm{Re}(\mathbf{U}_\alpha(\boldsymbol{\theta})) \end{bmatrix}, \ \mathbf{x}_\alpha = \begin{bmatrix} \mathrm{Re}(\mathbf{x}_\alpha) \\ \mathrm{Im}(\mathbf{x}_\alpha) \end{bmatrix}. \tag{4.4}$$

Substituting (4.4) into (4.3) yields $\mathbf{y} = \begin{bmatrix} \mathrm{Re}(\mathbf{y}) \\ \mathrm{Im}(\mathbf{y}) \end{bmatrix}$ and $\mathbf{y}$ can be reconstructed as $\mathbf{y} = \mathrm{Re}(\mathbf{y}) + j\,\mathrm{Im}(\mathbf{y})$.

Such a formulation treats the real and imaginary components of the complex weights as strictly independent variables. As noted in [62], this approach does not take advantage of the fact that the sparsity of the real and imaginary components of

$\mathbf{x}_\alpha$ are correlated. Namely, a non-zero element in $\mathbf{x}_\alpha$ is unlikely to be purely real or purely imaginary. This may be detrimental to the convergence to an accurate DOA estimate and we again appeal to the group-sparsity feature of BSBL to further reduce the space spanned by the basis vectors.

With these modifications, $\mathbf{\Phi}(\theta)$ and $\mathbf{x}$ from the original signal model in (4.1) are extended to sizes $2M \times 4N$ and $4N \times 1$, respectively. We note that under the concept of block sparsity, the column vectors of $\mathbf{\Phi}(\theta)$ are reordered so that, index-wise, the columns corresponding to each θ are contiguous.

4.3 Simulation Results

Two computational simulations are presented to demonstrate the efficacy of our modifications to BCS-DOA and BSBL-DOA. The first simulation is a validation effort to illustrate the advantage of SVO over non-SVO BCS and BSBL for generating DOA estimates of multiple polarized incident signals. The second simulation is a more comprehensive assessment of the DOA estimation performance over various combinations of incident angles, polarizations and array configurations.

4.3.1 Approach.

Simulations are performed using a computational tool to model planar incident fields impinging on a collection of dipole antennas. The software implements a Method of Moments (MOM) formulation, which provides full-wave electromagnetic solutions to the currents induced on the array and accounts for any mutual coupling effects that may arise when elements are in close proximity to one another [63]. The arrays are modeled as Perfect Electric Conductor (PEC) dipoles with a finite thickness and length. The simulation calculates the induced currents (which determine gain patterns $\mathbf{g}(\theta)$) and the input impedances at each antenna feed of the array (which determine voltage values for the steering vectors $\mathbf{\Phi}(\theta)$).

Figure 4.1 illustrates quantities of interest on a representative array placed in our reference coordinate system. To reduce the computational burden in our analysis, for all simulations, we restrict the DOA estimation to one parameter where azimuth is fixed to zero and elevation θ=$[0°, 90°]$. We recognize, however, that the algorithms can be generalized to perform DOA estimation for both azimuth and elevation. $\mathbf{s}_1$ and $\mathbf{s}_2$ represent two incident signals from the θ_1 and θ_2 direction and with polarizations

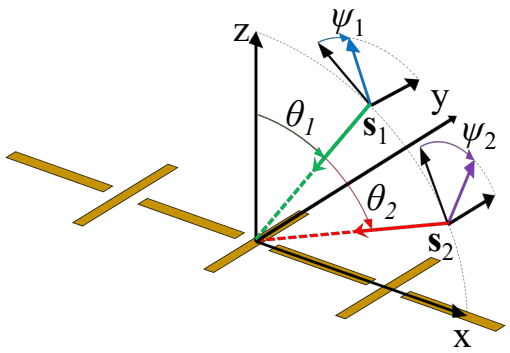

Figure 4.1: Reference coordinate system: a notional seven-element linear dipole array has two incident signals $\mathbf{s}_1$ and $\mathbf{s}_2$, with directions θ_1 and θ_2, and polarizations ψ_1 and ψ_2, respectively.

Figure 4.2 depicts three array configurations used in our simulations. For all three arrays, M=10 and consist of $\lambda/2$-length dipoles ($\lambda/10$ in width) and that the centers of each dipole (the feed locations) are constrained to the xz-plane.

Configuration (a) is an ideal linear array of dipoles where the alignment of each element alternates between the x- and y-axis and the feeds of each dipole are equally spaced $\lambda/2$ apart. Configuration (b) is a perturbed linear array where the dipoles are no longer perfectly aligned with the axes. The perturbations on the orientation of each element is defined by a tilt vector, whose values, in degrees, are drawn from a

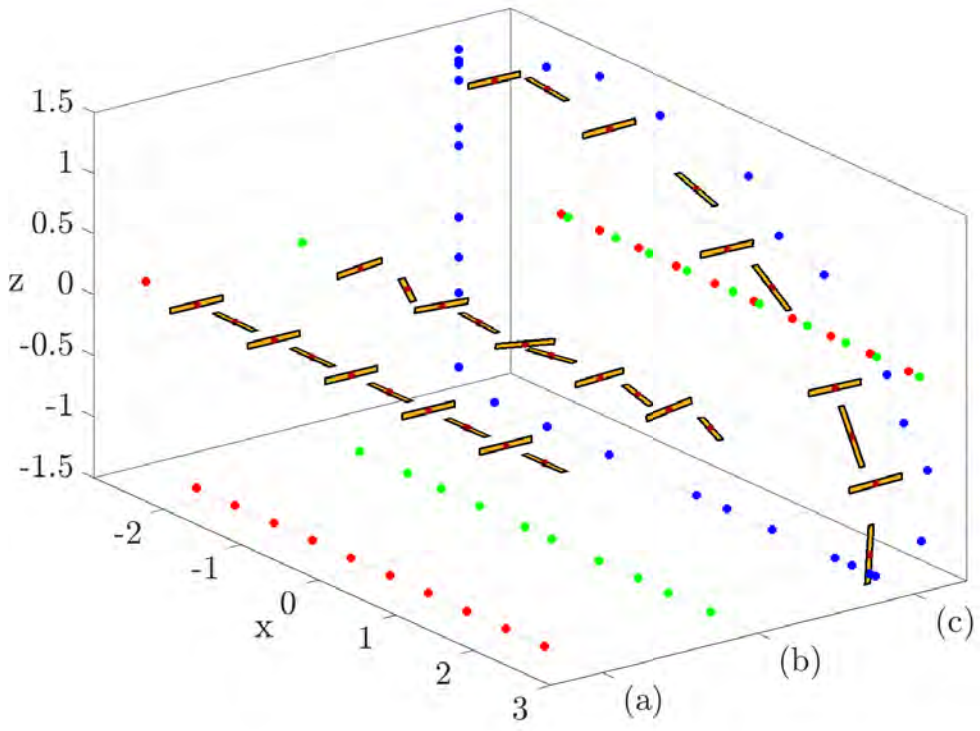

Figure 4.2: (a) Ideal linear, (b) Perturbed linear, and (c) Perturbed conformal array configurations. Feed locations are projected onto Cartesian planes to indicate the non-uniform separation of the array elements in (b) and (c).

normal distribution $\mathcal{N}(0,0.1)$. The spacing between the elements (in the x-direction) is also perturbed by a random value in the uniform distribution $\mathcal{U}(-0.25,0.25)\lambda$. Configuration (c) conforms an array to a quarter ellipse, where both the alignment and the spacing (in both the x- and z-direction) of the dipoles are altered with the same process and random distributions as the perturbed linear array.

4.3.2 SVO Validation.

The ideal linear array is employed to determine the effectiveness of SVO on BCS- and BSBL-DOA estimation of three fixed incident signals (K=3) and across multiple polarization combinations. The angular space spans θ=[0°,90°] in N=91

sectors. The incident angles θ_k, are set to $\{20°, 35°, 62°\}$ and the polarizations ψ_k are randomly generated for the first trial. Subsequent trials jointly rotate the polarization vectors over 175° discretized into P=36 sectors (the angular difference between the polarization vectors, $\Delta\psi = \{\psi_1 - \psi_2, \ldots, \psi_{K-1} - \psi_K\}$, remains constant). Gaussian noise $\mathcal{N}(0, 10^{-6})$ is added to the real and imaginary components of the voltage vector. This translates to approximately -87 dBm of noise power and was selected initially to make the recovery problem non-deterministic.

Figure 4.3 illustrates our simulation results for the four combinations of with and without SVO for BCS and BSBL. Each trial p=1, ..., P, yields a complex-valued weight vector and we depict the DOA estimate as $\hat{\mathbf{x}}_p(n) = |\hat{\mathbf{x}}_p(n)| / \max(|\hat{\mathbf{x}}_p(n)|)$. Regardless of method, the DOA estimation is poor without SVO (Figures 4.3(a) and (c)). BCS fails to estimate the correct DOA solution in many polarization combinations, while BSBL provides correlated estimates with many false positives. With SVO, BCS performs slightly better than without, while SVO BSBL shows nearly perfect DOA estimation performance.

These results suggest that without SVO, $\mathbf{\Phi}(\theta)$ only consists of a single set of DOA vectors and is an insufficient basis to span signals from other polarizations. With SVO, the basis set is doubled, but BCS often converges to incorrect solutions and is likely due to a severely overcomplete basis. Using BSBL to enforce grouping of non-zero elements within $\hat{\mathbf{x}}$ mitigates this by leveraging the block sparsity of the solution to discriminate within the larger basis.

Although we focus on single-snapshot performance in this study, the results from this simulation imply that SVO-BSBL will also work well in a multi-snapshot construct. We observe that, over multiple snapshots, the DOA of the incident signals may vary only slightly in angle or polarization. As such, the simulation results show very little angular spread in the DOA estimates across all polarizations ψ_k.

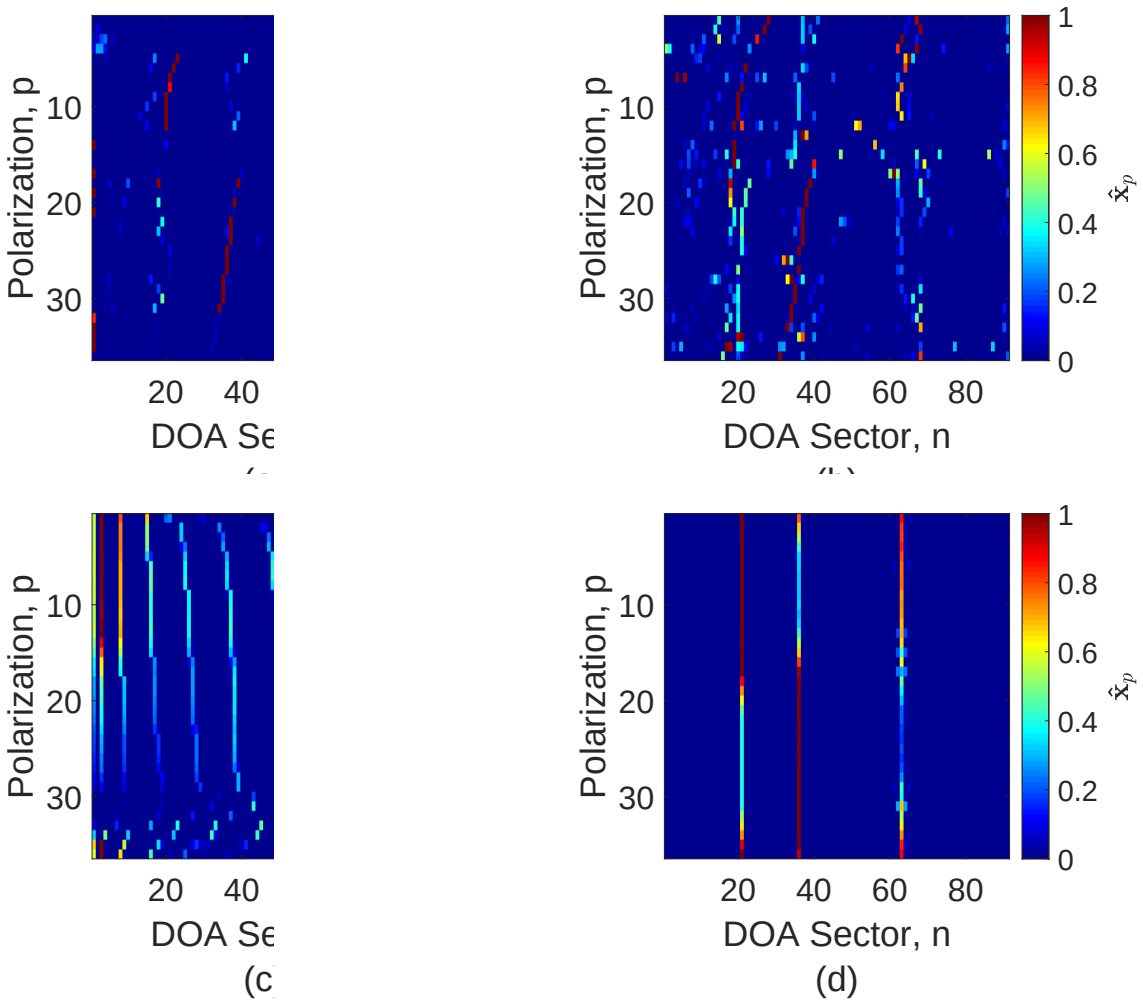

Figure 4.3: SVO validation: (a) BCS without SVO, (b) BCS with SVO, (c) BSBL without SVO, and (d) BSBL with SVO. Accurate reconstruction is achieved with SVO-BSBL, while others show significant false estimation errors.

4.3.3 Impact of Signal and Array Variations on SVO.

While the previous simulation demonstrates good SVO-BSBL performance for a specific set of incident signals with fixed angle separation, it is well known that the performance of DOA estimation algorithms often suffer when the incident signals are not adequately separated [64]. In addition, estimation performance is highly

dependent on the configuration of the array. The second simulation characterizes how SVO performs with respect to these issues.

In contrast to the previous simulation, the three array configurations in Figure 4.2 are evaluated with two incident signals instead of three. Moreover, each pair of incident signals is varied in both polarization ψ_k and separation $\Delta\psi$. The angular space spans [0°,90°] in 5° increments (N=19), $\Delta\psi$ spanned [0°,90°] in 15° increments (P=7), and ψ_k spanned [0°175°] in 5° increments (Q=36). The performance metric

$$\Delta\mathbf{x}(\theta_1, \theta_2) = \sum_{q=1}^{Q} \sum_{p=1}^{P} \sum_{n=1}^{N} |\hat{\mathbf{x}}(n) - \mathbf{x}(n)| \tag{4.5}$$

measures accuracy of estimate $\hat{\mathbf{x}}$ for each DOA combination.

Figures 4.4–4.6 summarize the performance of the three array configurations in this simulation. Each figure is a composite plot, illustrating the SVO-BCS performance in the upper diagonal and the SVO-BSBL performance in the lower diagonal, for each pair of θ_k. We observed $\Delta\mathbf{x}$ is symmetric across the diagonal when no noise is applied and nearly symmetric in simulations with noise set to $\mathcal{N}(0, 10^{-3})$ (approximately -27 dBm of noise power).

For the ideal linear array with no noise applied, SVO-BSBL generally performs better than SVO-BCS, but both perform poorly when one of the incident signals is near end-fire angles of the array ($n = 19$). This is a known issue [65], and is likely compounded by the fact that array elements are separated by exactly $\lambda/2$. We also see performance degradation where the $\theta_{1,2}$ are similar. We surmise that, in these cases, $\hat{\mathbf{x}}$ estimates two signals in the same sector, which is correct on the main diagonal but incorrect elsewhere, causing the banded behavior seen in Figures 4.4 and 4.5. For SVO-BCS, the mean and median values of $\Delta\mathbf{x}$ were 355.7 and 214, respectively; for SVO-BSBL mean and median values of $\Delta\mathbf{x}$ were 80.5 and 0, respectively.

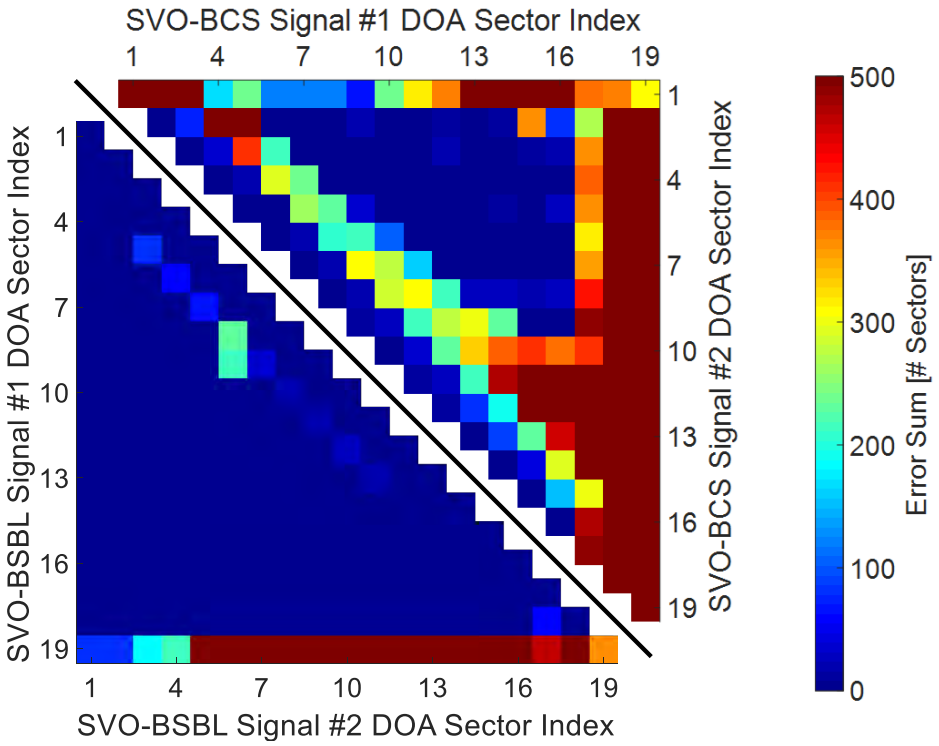

Figure 4.4: Ideal linear array performance, noise variance=0. For SVO-BSBL, accurate DOA estimates are achieved in most angle and polarization permutations except near end-fire and closely separated sectors.

On the perturbed linear array with measurement noise added, we observe that $\hat{\mathbf{x}}$ in the end-fire region improve due to the spatial variation of the elements in the x-axis, but performance is slightly degraded for other combinations of $\theta_{1,2}$. Nevertheless, BSBL still outperforms BCS by a significant margin, especially when the two incident angles are well separated. In contrast to the previous case, the results can vary due to the non-deterministic noise values, but the variance over multiple simulations was observed to be minor. In the trial shown in Figure 4.5, for SVO-BCS, the mean and median values of $\Delta\mathbf{x}$ were 153 and 125.5, respectively; for SVO-BSBL, the mean and median values of $\Delta\mathbf{x}$ were 8.2 and 0, respectively.

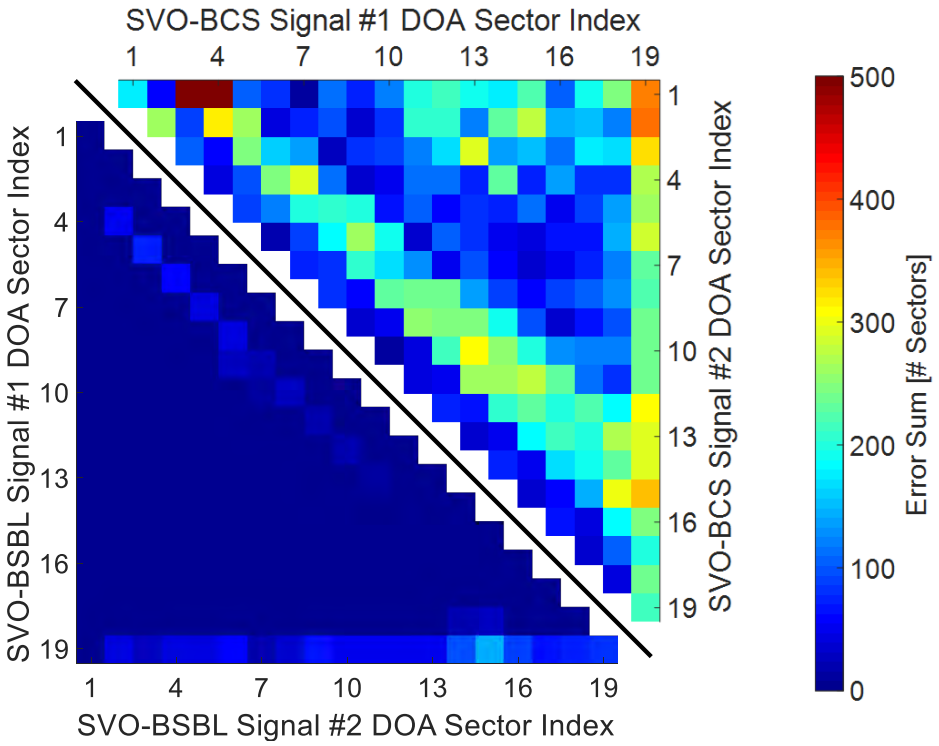

Figure 4.5: Perturbed linear array performance, noise variance=10^{-3}. DOA estimates improve under both methods, but SVO-BSBL continues to exhibit better performance than SVO-BCS.

Finally, with the conformal array and with noise applied, we observe SVO-BSBL maintains good estimation performance throughout all combinations of DOA and polarizations and continues to outperform SVO-BCS. Issues near the endfire region are resolved with the conformal array. A moderate level of error is diffuse across all DOA pairs with SVO-BCS, but the error statistics remain constant between the perturbed linear array and the conformal array: in the trial shown in Figure 4.6, for SVO-BCS, the mean and median values of $\Delta\mathbf{x}$ were 136.7 and 92, respectively; for SVO-BSBL, the mean and median values of $\Delta\mathbf{x}$ were 9.5 and 0, respectively. The banding from previous results is resolved due to the spatial diversity of the conformal

array elements, which improves the array's sensitivity to phase differences between two closely separated signals [66].

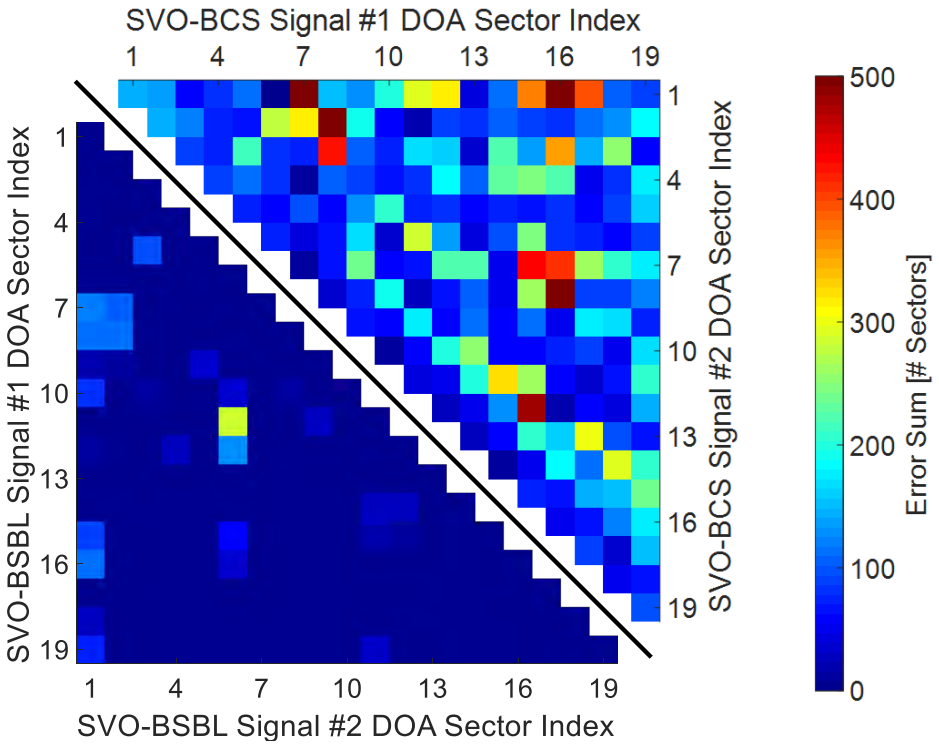

Figure 4.6: Perturbed conformal array performance, noise variance=10^{-3}. Further improvements in DOA estimation are seen in the end-fire and closely separated sectors of the SVO-BSBL result.

4.4 Conclusion

Our computational simulations with SVO applied to both BCS and BSBL show that the SVO-BSBL technique is a viable solution to generating accurate DOA estimates in non-ideal environments. We demonstrate good performance with a single snapshot measurement of multiple polarized signals incident on a perturbed, non-uniform array of dipole antennas.

Given these results, it would be prudent to further investigate the robustness of this technique. Trade studies may be performed to understand its performance under lower SNR scenarios, with multiple snapshots of measurements, other array configurations (non-uniform elements), and expanding the formulation for DOA estimates in azimuth and elevation.

V. Scattering Interpolation via Theory of Characteristic Modes

5.1 Introduction

The final thrust area for this dissertation is an investigation of characteristic modes as an alternative basis set. The primary driver for such a basis is to address non-localized scattering phenomena that occurs when the frequency of the illuminating radar falls within the resonance region of the target. These distributed effects are poorly represented with the bases we investigated previously and the unique properties of characteristic modes seem well-suited to address this shortcoming.

Developing such a basis may ultimately enable the use of Inverse Synthetic Aperture Radar (ISAR) reconstruction and noise removal techniques proposed in [6] at lower frequencies or for smaller targets. While one of the long term goals is to incorporate the Theory of Characteristic Modes (TCM)-derived basis into these techniques, our efforts to date primarily consist of an assessment and verification of the theory. We note that most of the applied research available in the Characteristic Mode Analysis (CMA) literature has focused on radiation for antenna design and performance characterization. However, because the underlying theory is based on Method of Moments (MOM), much of the formulation should be equally applicable to scattering problems as well. Given this, as an intermediate step, we reinterpret the formulation for scattering problems and leverage TCM principles to interpolate (and extrapolate) Radar Cross Section (RCS) quantities from a limited set measurements.

5.2 Theoretical Framework

TCM is based on an eigendecomposition of the linear model that underpins MOM. The electric field boundary condition states that the tangential component of the electric field is zero at a Perfect Electric Conductor (PEC) interface. In other

words, for an incident field $\mathbf{E}^i$, the sum of its tangential component with the tangential component of the scattered field $\mathbf{E}^s$ must be zero at the boundary between PEC and free-space, i.e.,

$$-\mathbf{E}^s_{\tan} = \mathbf{E}^i_{\tan}. \tag{5.1}$$

The scattered field at any point in free-space $\mathbf{r}'$ can be determined from integrating the currents over all points $\mathbf{r}$ on the target's surface S and radiating to the observation point via the free-space Green's function $G(\mathbf{r}, \mathbf{r}') = (e^{-jk|\mathbf{r}-\mathbf{r}'|})/(4\pi|\mathbf{r}-\mathbf{r}'|)$. This leads to the linear model

$$[\mathbf{Z}(\mathbf{J})]_{\tan} = \mathbf{E}^i_{\tan}, \tag{5.2}$$

where

$$\mathbf{Z}(\mathbf{J}) = \frac{jk_0\eta_0}{4\pi}\left(\int_S \mathbf{J}(\mathbf{r}')G(\mathbf{r},\mathbf{r}')dS' + \frac{1}{k_0^2}\nabla\int_S \nabla'\cdot\mathbf{J}(\mathbf{r}')G(\mathbf{r},\mathbf{r}')dS'\right). \tag{5.3}$$

which follows from the Helmholtz wave equation using the electric and magnetic vector potentials [50]. The linear operator $\mathbf{Z}$ is known as the impedance operator and $\mathbf{J}$ represents weights for the currents on the geometry. $\mathbf{Z}$ operates on the unknown weights in $\mathbf{J}$ to determine an equivalent scattered electric field that cancels the incident field. From a linear algebra perspective, inverting the impedance operator will yield the unknown current distribution over the body.

Computationally, the $\mathbf{Z}$ is implemented as an $N \times N$ matrix that represents a discretization of the scattering target into a mesh of triangular facets with a total of N edges. The Rao-Wilton-Glisson (RWG) basis function is applied over each pair of triangles to represent the current over two triangles. Applying the Galerkin method, where the basis functions are also used as the testing functions, yields a symmetric impedance matrix [67].

The symmetry of $\mathbf{Z}$ provides several favorable properties. Critically, it guarantees that $\mathbf{Z}$ is diagonalizable and it allows the real and imaginary components ($\mathbf{Z}$ =

$\mathbf{R} + j\mathbf{X}$) to be $\mathbf{R} = \frac{\mathbf{Z}+\mathbf{Z}^*}{2}$ and $\mathbf{X} = \frac{\mathbf{Z}-\mathbf{Z}^*}{2j}$, respectively. Given the eigenvalue problem

$$\mathbf{Z}(\mathbf{J}_n) = \upsilon_n \mathbf{W}(\mathbf{J}_n) \tag{5.4}$$

and allowing $\mathbf{W} = \mathbf{R}$ and $\upsilon_n = 1 + j\lambda_n$, Equation (5.4) reduces to the generalized eigenvalue problem

$$\begin{aligned} (\mathbf{R} + j\mathbf{X})(\mathbf{J}_n) &= (1 + j\lambda_n)\mathbf{R}(\mathbf{J}_n), \\ \mathbf{X}\mathbf{J}_n &= \lambda_n \mathbf{R}\mathbf{J}_n. \end{aligned} \tag{5.5}$$

Because $\mathbf{R}$ and $\mathbf{X}$ are real and symmetric, the eigenvectors $\mathbf{J}_n$ and eigenvalues λ_n are also real and $\mathbf{J}_n$ are orthogonal. This derivation implies that the original impedance operator formulation can be decomposed into a basis of characteristic modes: $\mathbf{J}_n$ are independent current distributions (characteristic currents) with corresponding weights λ_n that indicate the significance of each mode $n = 1, \ldots, N$. An orthonormal basis can be created by ensuring the inner product $\langle \mathbf{J}_n^*, \mathbf{R}\mathbf{J}_n \rangle = 1$ for all n.

From this generalized eigenvalue problem formulation, other quantities are defined to facilitate analysis. Because the characteristic modes are orthogonal, the total current distribution on the target $\mathbf{J}$ can be determined through the superposition of the characteristic currents and, likewise, the radiated fields from the target $\mathbf{E}$ can be determined by the superposition of the characteristic fields

$$\begin{aligned} \mathbf{J} &= \sum_n a_n \mathbf{J}_n, \\ \mathbf{E} &= \sum_n a_n \mathbf{E}_n, \end{aligned} \tag{5.6}$$

where each characteristic current is weighted with a complex coefficient a_n. Substituting Equation (5.6) into Equation (5.2) and and taking the inner product with $\mathbf{J}_m$ on both sides yields

$$\sum_n a_n \langle Z(\mathbf{J}_n), \mathbf{J}_m \rangle = \left\langle \mathbf{E}^i_{\tan}, \mathbf{J}_m \right\rangle. \tag{5.7}$$

Because the characteristic currents are orthogonal, there is only one non-zero term in the summation on the left hand side of Equation (5.7) and we see that

$$a_n = \frac{\langle \mathbf{E}^i_{\tan}(\mathbf{r}), \mathbf{J}_n \rangle}{1 + j\lambda_n}. \tag{5.8}$$

We note that the numerator of Equation (5.8) is referred to as the *modal excitation coefficient*. Equation (5.8) clearly indicates that, while the characteristic currents $\mathbf{J}_n$ and characteristic fields $\mathbf{E}_n$ are independent of excitation, the overall current distribution formed on the body $\mathbf{J}$ and the overall fields scattered by the body $\mathbf{E}$ are not. They both depend on the modal excitation coefficient, which represents how the tangential incident field of the source $\mathbf{E}^i_{\tan}$ couples with the characteristic current $\mathbf{J}_n$ for each mode. Intuitively, from an antenna perspective, the radiation of the body depends on the location of the feed. Likewise, from a scattering perspective, the RCS depends on the direction (and polarization) of the incident field. Additionally, the magnitude of the denominator in Equation (5.8) is referred to as the *modal significance* ($\text{MS} = |1/(1 + j\lambda_n)|$). This term is also consistent with the previous assertion that modes with smaller eigenvalues correspond to characteristic currents that have larger contributions to the overall current and field distributions.

5.3 Methodology

Using the concepts highlighted in the previous section, we investigate the feasibility of using a TCM-derived basis to perform RCS interpolation across frequencies and angles. Much of the literature is focused on antenna design and creating geometries to exploit characteristic modes for efficient radiation. Of the few that pertain to scattering, it was shown that the overall RCS can also be decomposed into its characteristic modes. We first attempt to replicate the results found in [52], which presents results of a numerical RCS reconstruction experiment of the NASA Almond target.

The scattering target, shown in Figure 5.1, is a common benchmark RCS target for numerical codes and radar range tests because it provides a combination of specular and non-localized scattering effects. It also has a simple parametric description which facilitates the repeatability of experiments [68]. The model is 0.25 m in length and was discretized into 974 triangular facets (1461 edges). At 1.2 GHz, the target is approximately 1 wavelength long with a mesh density of 25 samples per wavelength; at 2 GHz, the target is 1.67 wavelengths long with a mesh density of 15 samples per wavelength. The mesh is sufficiently dense for all frequencies of interest (0.5 GHz to 2 GHz) and was used in all of our evaluations to ensure consistency in the results.

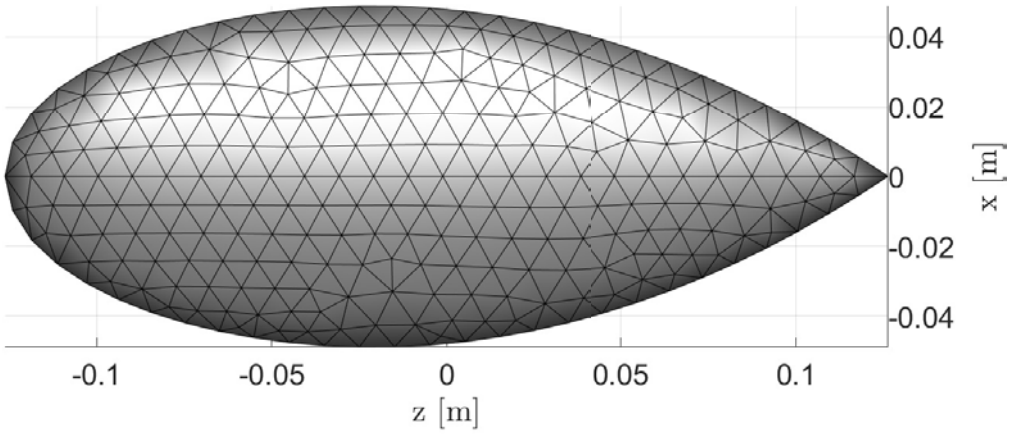

Figure 5.1: NASA Almond geometry.

We propose two methods to generate RCS predictions without performing the full MOM process. In the first method, we recall from Equation (5.6) that the total scattered field can be reconstructed as a weighted sum of the characteristic fields. The weight term a_n is a function of the eigenvalue, characteristic current and the incident

electric field for a given mode n and incident angle. If these terms are relatively constant for small deviations in frequency and/or can accurately be interpolated, then RCS predictions from the interpolated values may be feasible. Figure 5.2 illustrates the behavior of the eigenvalues between 0.5 and 2 GHz. We see that the although the number of significant modes ($\lambda_n \approx 0$) increases as a function of frequency, each mode has a stable trajectory across the frequencies of interest.

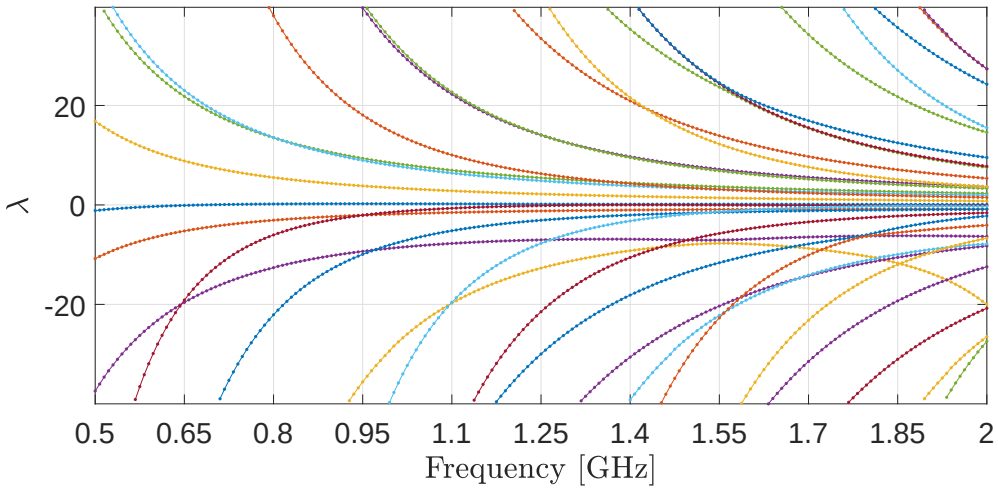

Figure 5.2: Trajectory of the first 50 eigenvalues of the NASA Almond.

With respect to the characteristic currents, Figure 5.3 shows, for the first mode, that the distributions remain similar for small deviations in frequency for the lowest, center, and highest frequency of interest. Correspondingly, the characteristic fields, shown in Figure 5.4, are determined from the characteristic currents, and they too show very similar patterns for small deviations in frequency.

Through interpolation of the eigenvalues λ_n, we can determine the weights a_n for the characteristic currents and fields for adjacent frequencies without the computational expense of decomposing the impedance matrix. We theorize that this

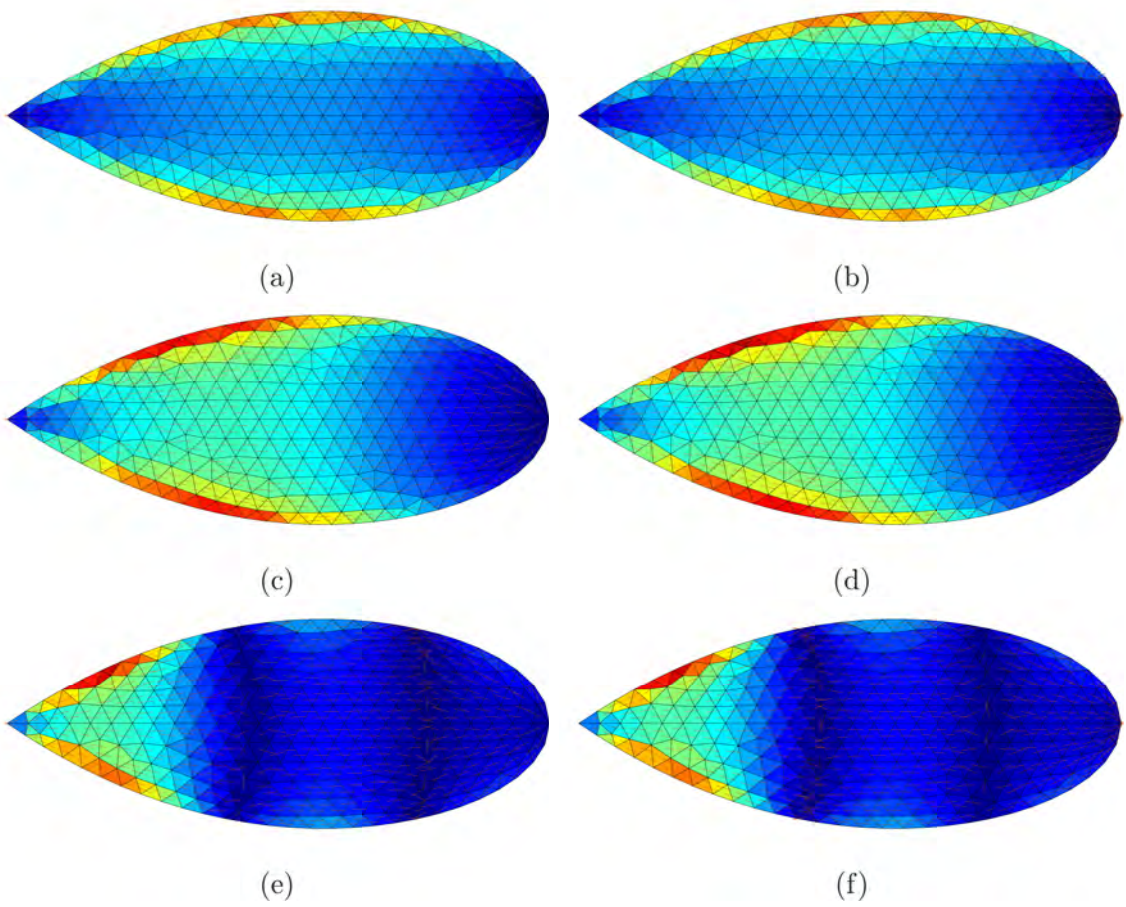

Figure 5.3: Characteristic currents of the first mode for (a) 0.5 GHz, (b) 0.525 GHz, (c) 1.2 GHz, (d) 1.225 GHz, (e) 1.975 GHz, and (f) 2 GHz.

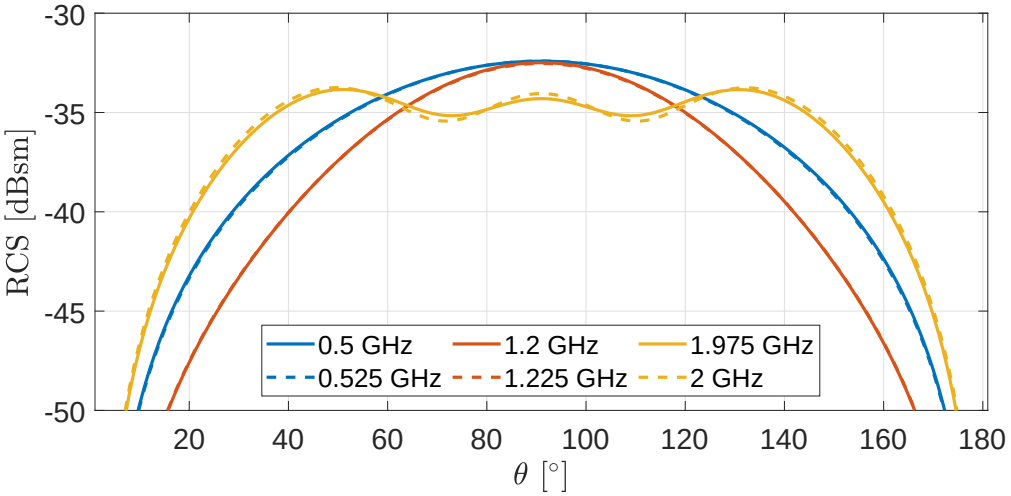

Figure 5.4: Comparison of characteristic fields (magnitude) from the first mode for 0.5, 0.525, 1.2, 1.225, 1.975, and 2 GHz.

interpolation should perform better than a direct interpolation of the RCS predictions, since the TCM basis captures the inherent resonances of the target that the direct RCS interpolation would not.

In the second method, we leverage the orthogonality property of the modal currents to determine a sparse solution for a traditionally underdetermined problem. That is, like the previous thrust areas, we use a sparsity-promoting solver to determine a solution for the eigenvalues of each modal current distribution. The weights are then used to generate RCS predictions for monostatic angles that were not directly measured and provided to the solver. This approach also assumes that the signal we are attempting to reconstruct has a sparse representation. Figure 5.5 shows, as a function of modal significance, the number of the characteristic currents required to reconstruct the signature over the frequency band of interest. Again, we see that while the level of sparsity decreases as a function of frequency, the number of significant modes is still minimal relative to the number of modes that the target can theoretically

support. We speculate that these characteristics satisfy the fundamental tenets of Compressive Sensing (CS) and may enable recovery of full signature patterns with a limited number of measurements.

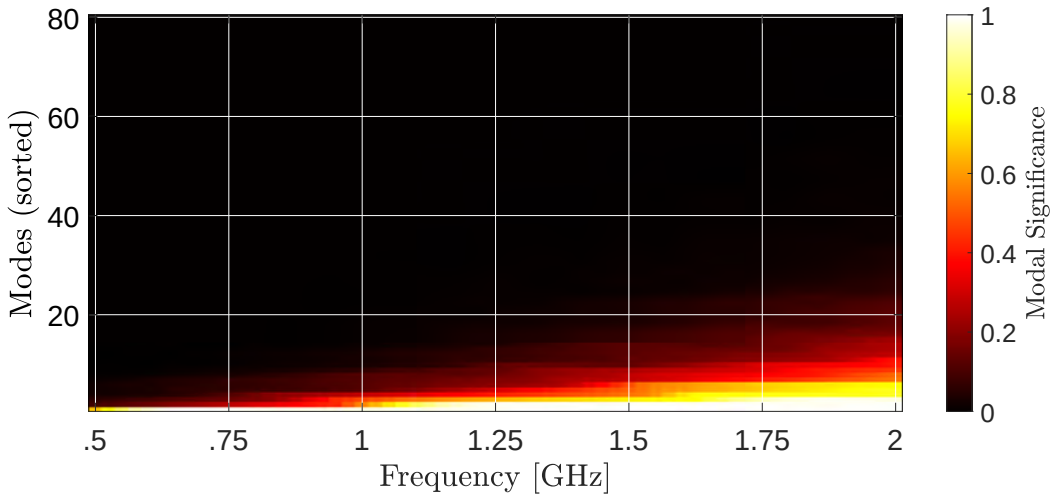

Figure 5.5: Sparsity of significant modes. The number of modes with high modal significance values drops off quickly for all frequencies of interest.

To facilitate our investigation, we leverage an open-source CMA library for MATLAB [69]. The software provides a convenient means of generating an impedance matrix and most of the the salient CMA quantities to perform our analysis. The routines generally followed the numerical implementation described in [50, 70]. The library was developed primarily for radiation problems, therefore additional code was developed to generate planar incident fields and to calculate far-field quantities for RCS calculations (specifically, the quantities to compute the modal excitation coefficient in Equation (5.8)). The CMA routines also follow an unconventional coordinate system where the body is rotated instead of altering the direction of the incident and scattered field. Using this system, the polarization and direction vectors

for the incident field remain static in our routines and the tangential component of the electric field $\mathbf{E}^i_{\tan}$ is calculated by taking the dot product of the incident field and the normal vector for each facet of the mesh.

5.4 Numerical Experiments and Observations

5.4.1 Reference Data Discrepancies.

With respect to replicating the results found in [52], a common reference dataset must first be established. We utilized the MOM-based RCS routine in MATLAB to generate reference data for the NASA Almond and compared it to the reference data cited in Bouche. It was observed that the reference data reported in Bouche was offset from the MATLAB predictions by approximately 20 dB, as shown in Figure 5.6.

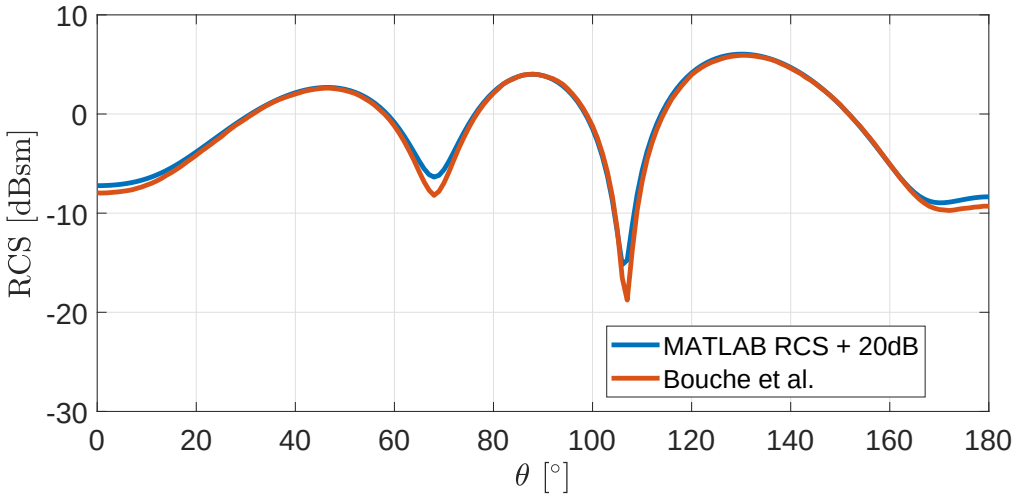

Figure 5.6: Reference dataset is overpredicting by 20 dB.

A third government-sponsored MOM code was leveraged to resolve this discrepancy. There was near overlay agreement between the results from MATLAB and the government-sponsored codes, lending credence to the MATLAB predictions. Given this result, we speculate that a normalization issue exists in the code that

Bouche used to generate the reported results. In fact, follow-on work from [71] which uses the same theoretical concepts and codebase presents a slightly different expression for the RCS quantity. While neither paper annotates their plots with units, RCS is generally assumed to be reported as a ratio relative to a square meter (dBsm). These discrepancies further suggest that the MATLAB predictions are the more accurate reference data set.

5.4.2 Replication of Prior Results.

Using the sample code provided by [69] and additional routines we developed, we observed that our CMA reconstruction of RCS predictions suffers from normalization issues as well. Figure 5.7 shows that the reconstructed 1.2 GHz signature, using the first 16 modes to be consistent with the reconstruction results reported in Bouche, needed to be offset by 7 dB to align with Bouche and 27 dB to align with the MATLAB predictions. While the general shape seems to be consistent with the reference data, the RCS predictions for aspect angles near the tip and back of the target diverge by approximately 1 dB. Further, the nulls that are present in the reference data are not captured well with our reconstruction.

Figure 5.8 illustrates the MATLAB and CMA reconstruction (with the offset applied) across all frequencies between 0.5 GHz and 2 GHz (in 0.025 GHz increments), as well as a third plot depicting the absolute difference between the two data sets. In all cases, a maximum of 23 modes were used to reconstruct the signature for each frequency.

Qualitatively, the majority of the discrepancies appear to occur either near nulls or where the reference signature drops below 0 dBsm. While it is common for the sharp nulls of an RCS pattern to drift slightly in angle or magnitude due to numerical precision of the computations, the severity of the discrepancies observed in these results suggest other underlying issues are involved.

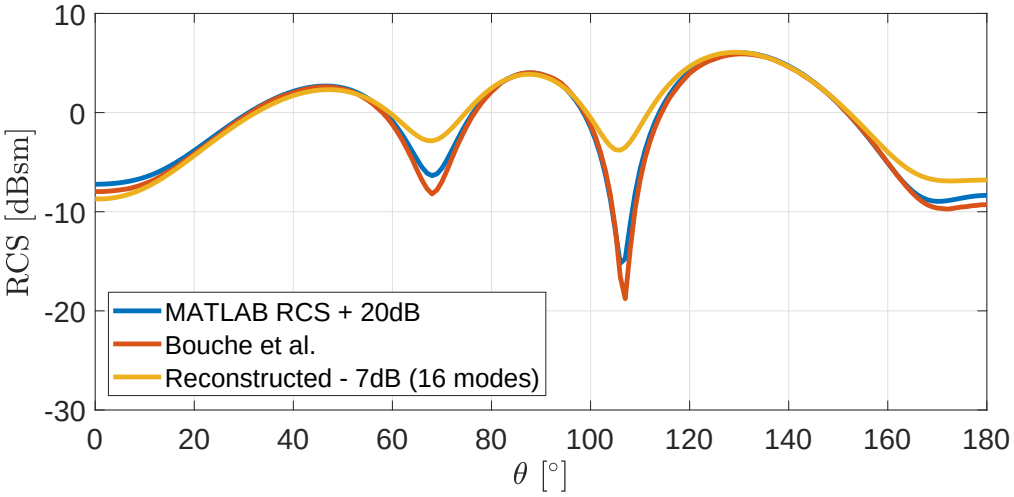

Figure 5.7: CMA reconstruction for 1200MHz using first 16 modes.

Our review of the source code did not uncover any inconsistencies between the implementation and the formulation presented in [50]. However we note that, while they may be consistent, there may be issues inherent with formulation. In one of the few resources that cover the computational implementation of CMA [72], the authors describe two methods for computing the far-field quantity: either through the computation of the radiation vector with surface currents over each facet or by interpreting the edges of the mesh as an infinitesimally small dipole and integrating over all the edges to compute a far (or near) field pattern. The trade between these methods is primarily accuracy at the expense of computation time. The CMA code we leveraged for this study implements the dipole method and therefore a future effort should investigate the latter approach.

We also observe from our experiments that the level of agreement does not necessarily improve monotonically as we increase the number of modes contributing to the far-field. This is unexpected behavior because it is assumed that including additional modes will always improve the accuracy of the reconstruction and

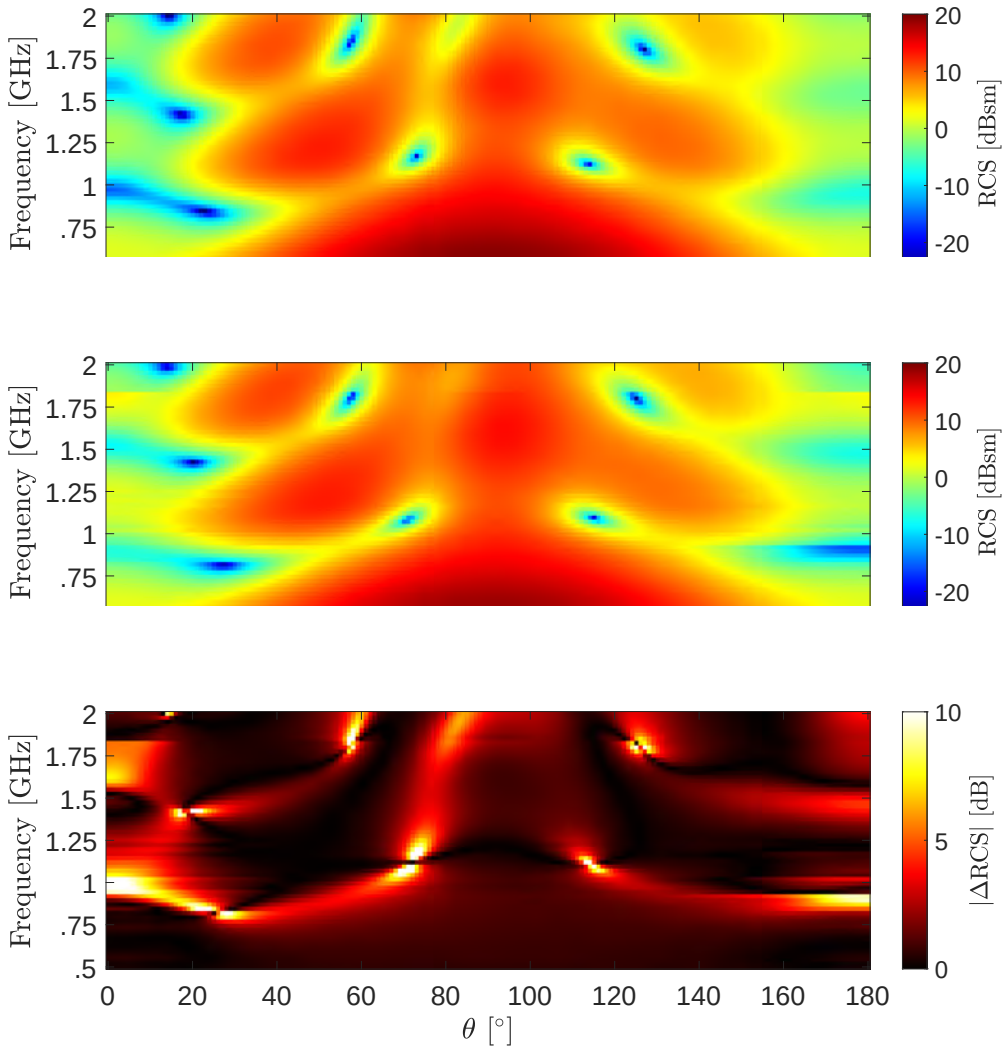

Figure 5.8: RCS predictions from MATLAB (top), CMA reconstructed (middle), and the magnitude difference (bottom).

eventually converge to the standard MOM prediction. In this experiment, going beyond the first 23 modes introduced artifacts and yields poorer reconstruction for some frequencies, as shown in Figure 5.9. This behavior is acknowledged in other references [72] which attribute these spurious modes to several possibilities, such as ill-conditioned impedance matrices and over-discretized meshes of the target.

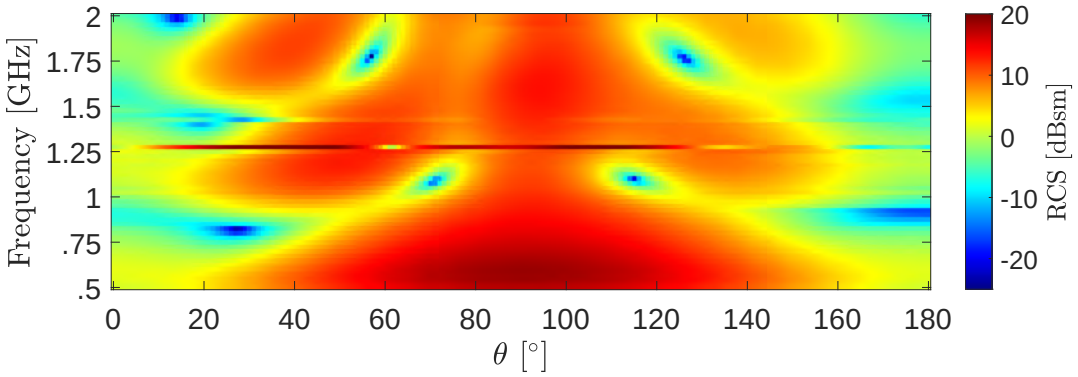

Figure 5.9: RCS Reconstruction with first 24 modes.

In a similar vein, we also see that there are discontinuities in the reconstruction across frequencies. In the CMA-reconstructed data shown in Figure 5.8, there is a sharp shift in the signature in the 0° to 20° and 160° to 180° sectors near 1.8 GHz that is likely non-physical. We observed that these discontinuities arise whenever the set of the most significant modes changes. To illustrate this, if the entire range of frequencies is reconstructed with only the three most significant modes, as shown in Figure 5.10, discontinuities in the plot occur at at 0.8 and 1.6 GHz. These frequencies correspond to particular intersections of the modes in the modal significance plot, shown in Figure 5.11. Specifically, at these frequencies, the mode represented in

red overtakes the mode represented in yellow at 0.8 GHz and, similarly, where the mode represented in cyan overtakes the mode represented in orange at 1.6 GHz. We note that the discontinuities in the far-field reconstruction only occur when there is a change in the set of the most significant modes and not necessarily where there is a change in the ranking. For example, there is no discontinuity in the RCS plot at 0.95 GHz, where the modes represented by the red and orange curve swap ranks.

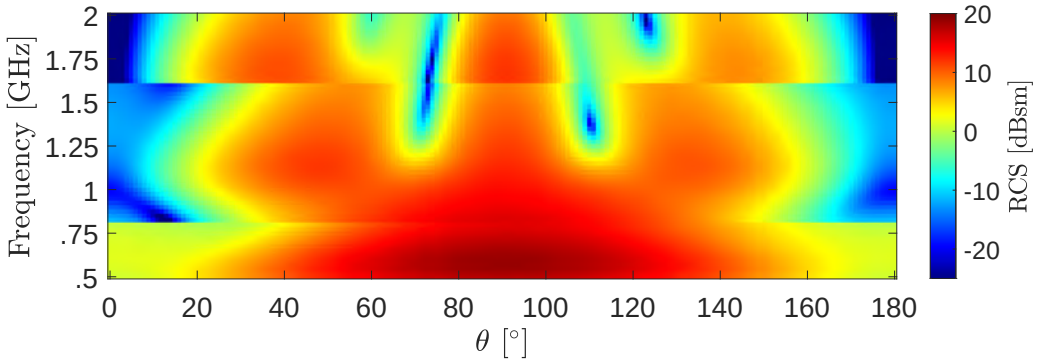

Figure 5.10: RCS Reconstruction with first three modes.

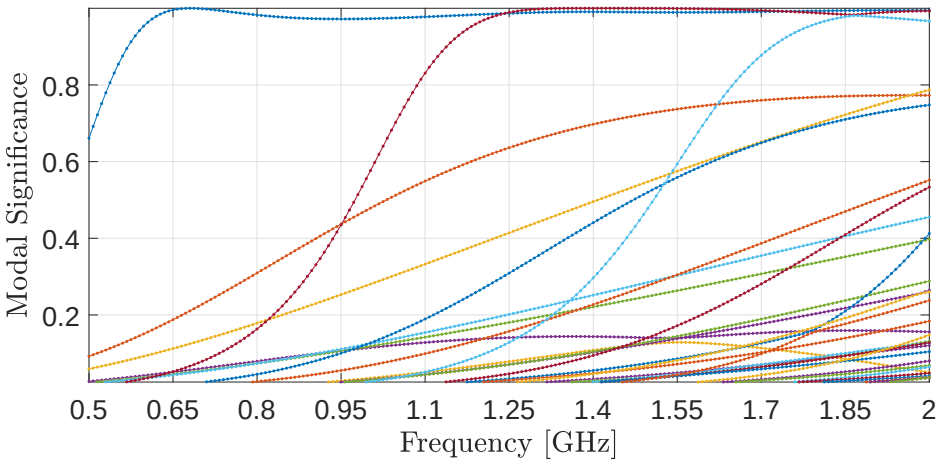

Figure 5.11: Modal significance for NASA Almond.

The discontinuities are especially prominent in Figure 5.10 because the three modes have high modal significance values. This observation suggests that the reconstruction shown in Figure 5.8 using 23 modes has not converged. This is corroborated by the fact that the discontinuity near 1.8 GHz with 23 modes (shown in Figure 5.8) is largely resolved when a 24th mode is introduced (shown in Figure 5.9). However, due to the artifacts introduced by the spurious modes discussed previously, a more accurate reconstruction can not be achieved until the spurious modes are identified and omitted from the reconstruction process.

Incidentally, with respect to the convergence of the reconstruction results, we note that a number of references indicate that modal significance values greater than $1/\sqrt{2}$ may be used to discriminate between significant from non-significant modes [50]. However, this metric was not valid from our empirical observations of the NASA Almond target. From Figure 5.5, we see that only one to six modes are above this threshold for the entire frequency band. However, many more modes were required to achieve a reasonable reconstruction. We also note that Bouche required at least 17 modes to achieve the reported results.

5.4.3 RCS Predictions via Eigenvalue Interpolation.

Due to unresolved issues with validating the scattering reconstruction, an end-to-end test of the technique could not be performed. Instead, we present an assessment of the feasibility of the interpolation approach as a separate exercise from the reconstruction results in the previous section. To do this, we use our previously reconstructed results as our reference data instead of the predictions generated by the MATLAB RCS routine. Doing so prevents us from confounding the errors from the CMA implementation with errors in the interpolation.

As shown previously, the frequency range of interest was limited to 0.5 to 2 GHz and RCS predictions were generated in increments of 0.025 GHz. The most basic

implementation of the interpolation approach is to allow the characteristic currents to span 0.05 GHz. That is, every other frequency is calculated by reusing the modal currents from an adjacent frequency in a nearest neighbor approach. The eigenvalues would normally be generated via an interpolation scheme. However, as a proof-of-concept, we use the CMA-calculated values to make a preliminary assessment of the approach. The results of this experiment are shown in Figure 5.12.

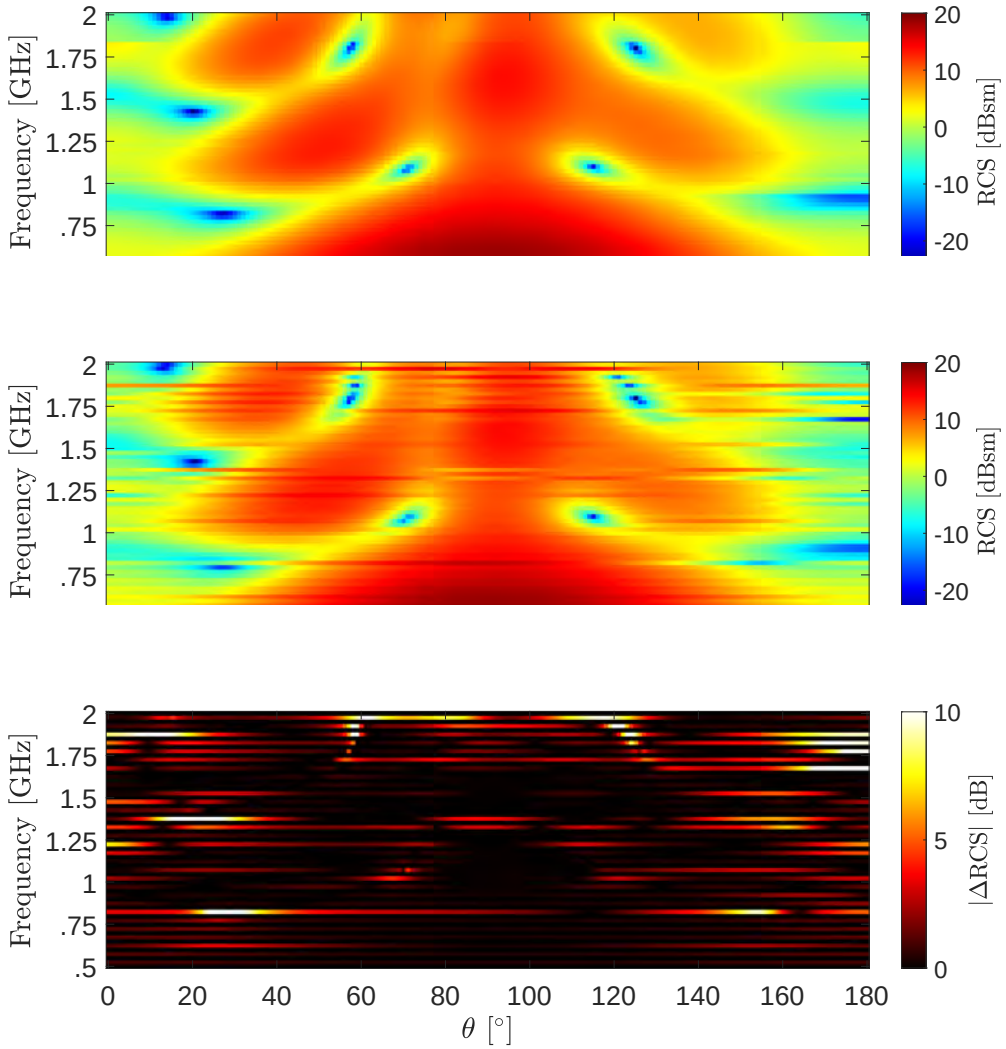

Figure 5.12: Performance of Interpolation of CMA eigenvalues.

The approach achieves mixed results and there are clearly large discontinuities between each frequency in the interpolated results. This is an unexpected result because most of the components contributing to the modal excitation coefficient do not vary greatly over small perturbations in frequency. Moreover, the level of error exhibited by the approach seems to be concentrated around the higher frequencies of the bandwidth. This may be due to the fact that there are more modes (with higher modal significance values) contributing to the higher frequencies, therefore may suffer from more accumulated error due to the interpolation.

A second attempt at this interpolation approach involved recalculating the tangential component of the incident electric field for each frequency. Whereas in the previous experiment only the denominator of Equation (5.8) varies, we now account for the fact that the incident electric field is a function of frequency and therefore should vary along with the eigenvalue in the interpolation. Although this requires recomputing the tangential component of the electric field on each facet of the mesh, we can still avoid the regeneration of the impedance matrix for every frequency. However, as Figure 5.13 shows, accounting for the variation in $\mathbf{E}^i_{\tan}$ yields minimal improvement in the interpolation performance.

We surmise that the interpolation approach does not provide adequate performance because, while the magnitude of the characteristic fields remains constant for small variations in frequency, the phase does not. As Figure 5.14 illustrates, these phase shifts are neither constant across frequencies, angles, nor modes. The small changes in phase likely cause a significant cumulative effect on the reconstruction. Because the change in phase increases as a function of frequency, this may also explain why the interpolation performance is worse at higher frequencies.

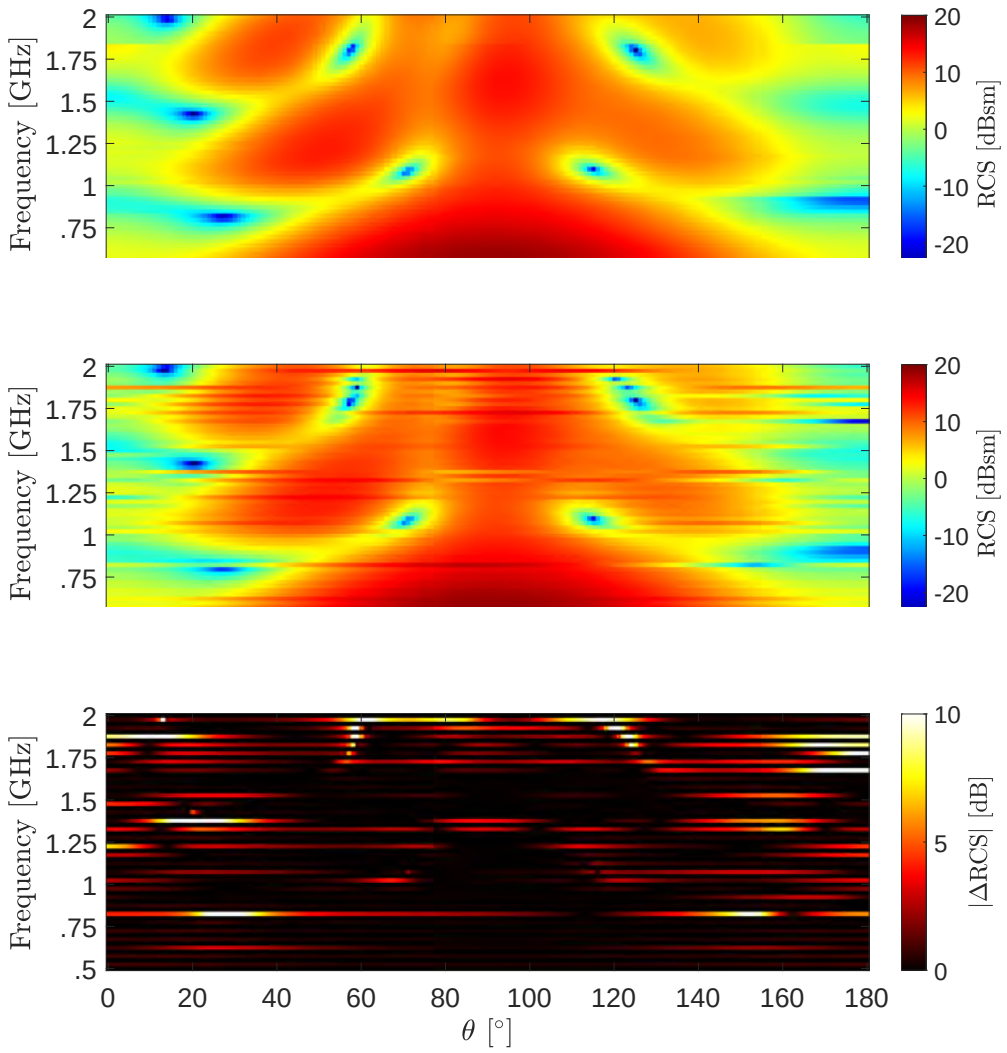

Figure 5.13: Performance of Interpolation of CMA eigenvalues ($\mathbf{E}^i_{\tan}$ recalculated).

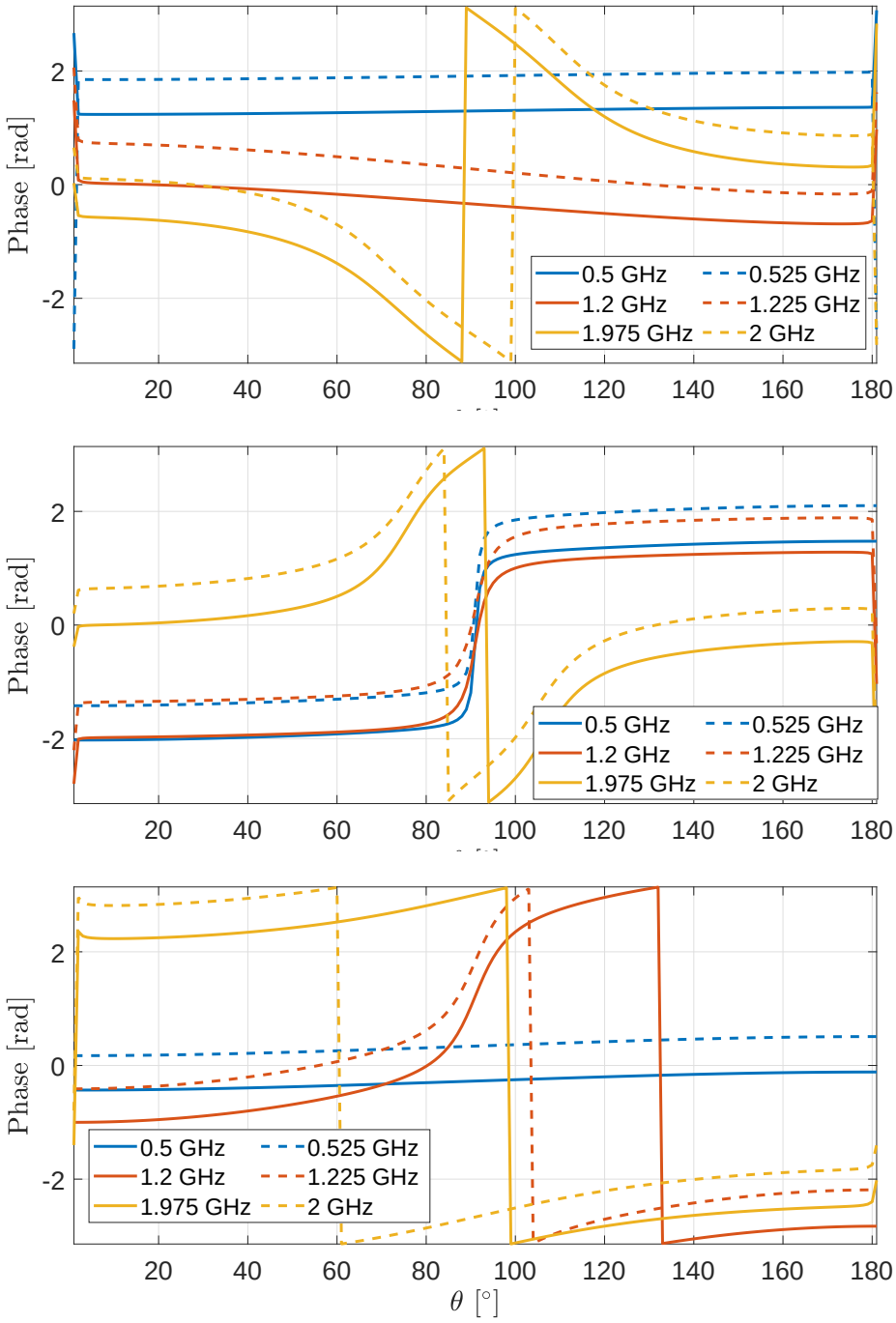

Figure 5.14: Comparison of the phase of the characteristic fields from the first (top), second (middle), and third (bottom) modes for 0.5, 0.525, 1.2, 1.225, 1.975, and 2 GHz.

5.4.4 Mode-Tracking Ambiguities.

Through our numerical simulations of the first interpolation schemes, we observe additional limitations to the applicability of the proposed method. Computing the eigenvalues over a frequency band yields a series of points, shown in Figure 5.15, that seem easily interpretable as the modal curves shown previously in Figure 5.2.

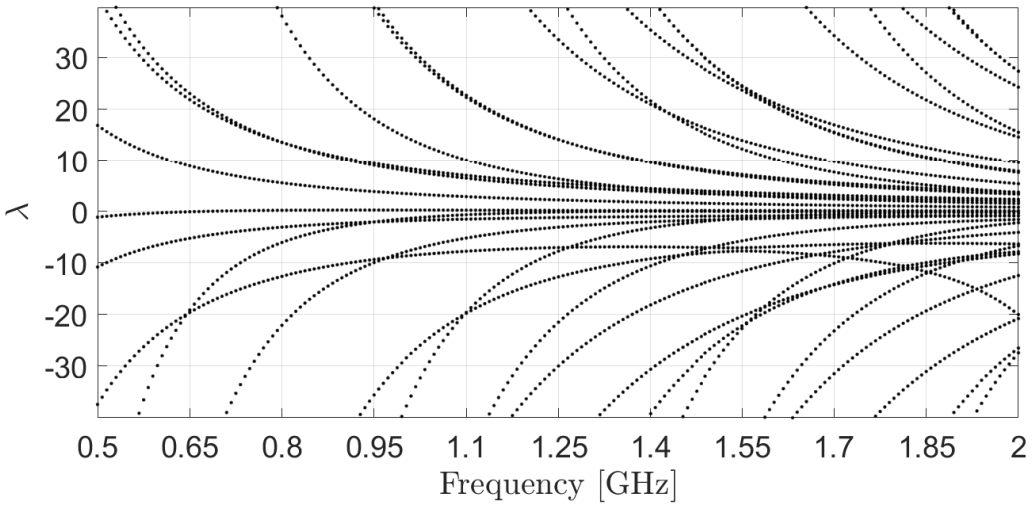

Figure 5.15: Eigenvalues for NASA Almond.

However, tracking the evolution of the modes over a band of frequencies is a non-trivial issue. In the case of the NASA Almond, most of the modal curves seem to monotonically converge to zero, but there are some that do not. We also observe small oscillations in the modes as they approach zero at the higher frequencies. In regions where the the modes cross over, the trajectory of the mode may be unclear. An example of this is shown in Figure 5.16.

Because of these ambiguities, an eigenvalue may be incorrectly associated to a characteristic current, resulting in an errors in the RCS reconstruction. Moreover, the tracking ambiguities are further exacerbated at higher frequencies, where many of

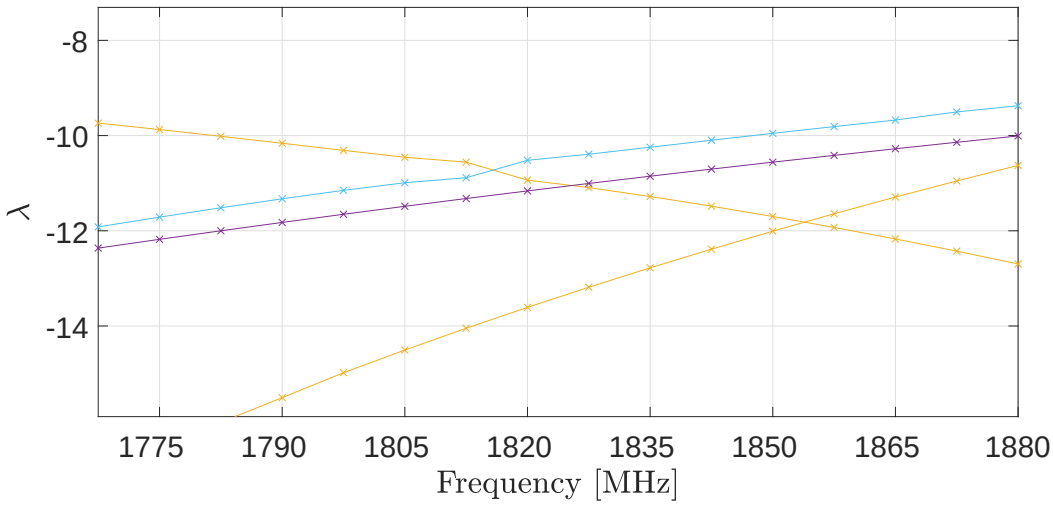

Figure 5.16: Ambiguity in mode tracking.

the modes are approaching zero. We found that these ambiguities can sometimes be resolved by increasing the sampling rate and performing an eigenvalue decomposition at an intermediate frequency to refine the trajectories. However, this may not always be sufficient since numerical noise from the eigenvalue decomposition may provide inaccurate values. Solutions to this tracking issue have been cited and proposed in [50, 73, 74], but were beyond the scope of this effort.

5.4.5 Interpolation and Extrapolation via CMA as a Sparse Basis.

Whereas the first interpolation scheme sought to generate RCS predictions for frequencies that were not directly measured or computed, the second scheme seeks to interpolate and extrapolate RCS predictions for monostatic angles that were not directly measured or computed. Recall that the MOM formulation states that the far-field RCS of a target is the result of an induced current distribution over the target. Moreover, TCM states that this current distribution is a weighted sum of characteristic currents and only a limited number of these modal distributions is necessary to reconstruct the overall current distribution. The proposed scheme

leverages characteristic modes as a sparse basis and uses a sparse solver to estimate a solution for the currents over the entire scattering target with only a limited set of far-field observations. From this estimate of the overall current distribution, RCS predictions can be generated for the missing observation angles.

Algebraically, we return to the linear model, $\mathbf{y} = \mathbf{A}\mathbf{x}+\mathbf{n}$. In this application, $\mathbf{y}$ is an $M \times 1$ vector of monostatic complex-valued far-field measurements, $\mathbf{A}$ is an $M \times N$ operator that maps the charateristic fields to the total scattered field, $\mathbf{x}$ is the sparse $N \times 1$ vector of weights for each mode, and $\mathbf{n}$ is an $M \times 1$ vector of measurement noise. Similiar to previous applications, $M < N$ and yields a classically underdetermined system.

To generate this system, we recall from Equation (5.6) that the total scattered field is a summation of the characteristic fields $\mathbf{E}_n$ that are weighted by the complex term, a_n. We can further isolate sparse parameter such that A is a collection of N $M \times 1$ column vectors, where

$$\mathbf{A}(n) = \mathbf{E}_n \left\langle \mathbf{E}^i_{\tan}, \mathbf{J}_m \right\rangle \tag{5.9}$$

and each element in the vector $\mathbf{x}$ is related to the modal significance

$$\mathbf{x}(n) = \frac{1}{1 + j\lambda_n} \tag{5.10}$$

for all modes $n = 1, \ldots, N$. As shown in Figure 5.5, most of the elements in $\mathbf{x}$ should be zero in the frequency range of 0.5 to 2 GHz.

Similar to the first interpolation approach, we use synthesized data instead of the MOM solutions from MATLAB as the set of measurements $\mathbf{y}$ to bypass the unresolved issues with our CMA reconstruction. The measurement values are perturbed from their ideal values with the addition of noise via $\mathbf{n}$. In all of our numerical simulations, we apply -20 dBm of white Gaussian noise to each measurement to make the sparse recovery problem non-deterministic.

Because the sparse vector of modal weights $\mathbf{x}$ is complex-valued, we again appeal to the Block-Sparse Bayesian Learning (BSBL) sparse solver to take advantage of the group sparsity between the real and imaginary terms of each weight. We again assume that $\mathbf{x}(n)$ is unlikely to be purely real or imaginary and the same modification found in the Direction of Arrival (DOA) thrust area (specifically, Equation (4.4)) is applied. Given a limited set of far-field observations, the solver is tasked to determine a sparse solution for the weight vector such that the currents on the body support the far-field observations. The solution for $\mathbf{x}$ is then used to generate far-field predictions of the target at unmeasured sectors (additional rows of $\mathbf{A}$).

The first numerical simulation aimed to interpolate the NASA Almond 2 GHz RCS data. The sparse solver was provided with $M = 19$ measurements uniformly spaced between 0° to 180°. The measurements values were selected from the reference dataset and perturbed by -20 dBm of white Gaussian noise. The results illustrated

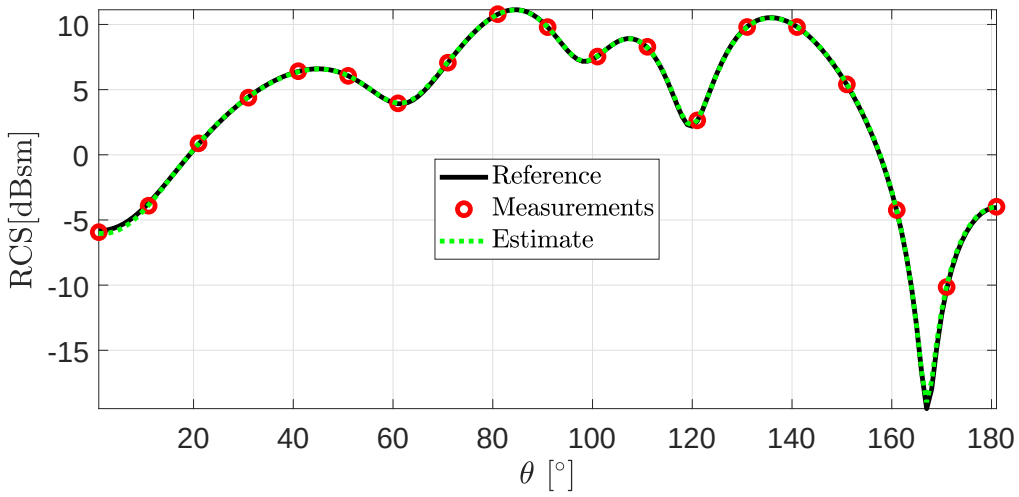

Figure 5.17: Scattering estimate from CMA-BSBL interpolation (19 uniform samples).

in Figure 5.17 show overlay agreement with the reference data and captures the

deep null near 180° that a standard interpolation algorithm would have missed. It is important to note, however, that the estimate of $\mathbf{x}$ generated by BSBL does not match the weights that were used to generate the reference and measurement data, as shown in Figure 5.18 This result indicates that there is an inconsistency between

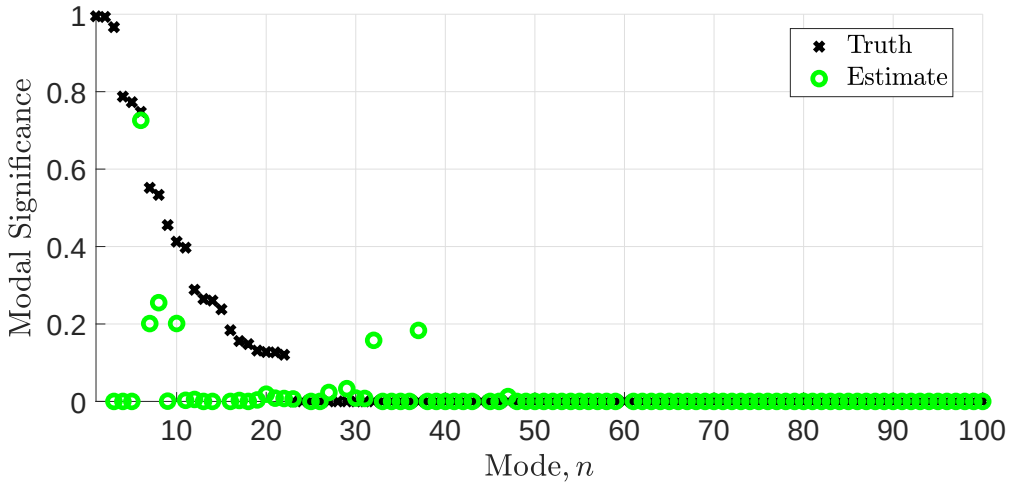

Figure 5.18: Modal significance estimate from CMA-BSBL interpolation (19 uniform samples).

the theory and our observed results. Namely, in addition to the sparsity seen in Figure 5.5, TCM states that the modal currents are orthogonal. This satisfies the general requirements for a CS-amenable problem and implies that there is a unique solution to the weight parameters. It is unclear why our results are able to achieve overlay agreement (in both magnitude and phase) using a different distribution of weights and remains an open question.

The next simulation is identical to the previous one, except a random selection of 20 measurements from the 180 degree sector was chosen and provided to the sparse solver instead of a uniformly spaced set of measurements. We again see overlay agreement between the interpolated result and the reference data shown in

Figures 5.19. In this example, the RCS estimate accurately tracks many of the features of the reference data and clearly demonstrates the efficacy of this interpolation scheme. Instead of interpolating the RCS data directly, the sparse solver successfully generates a feasible solution such that the overall current distribution supports the given far-field measurements. This approach to inverse scattering is aided by the fact that the current distribution is not completely arbitrary. Rather, the distribution is determined by the geometric properties of the scatterer and therefore has a limited set of resonant modes it can support. This effectively reduces the search space of feasible current distributions and allows the interpolation scheme to predict trends in in the far-field data that a general interpolation scheme cannot.

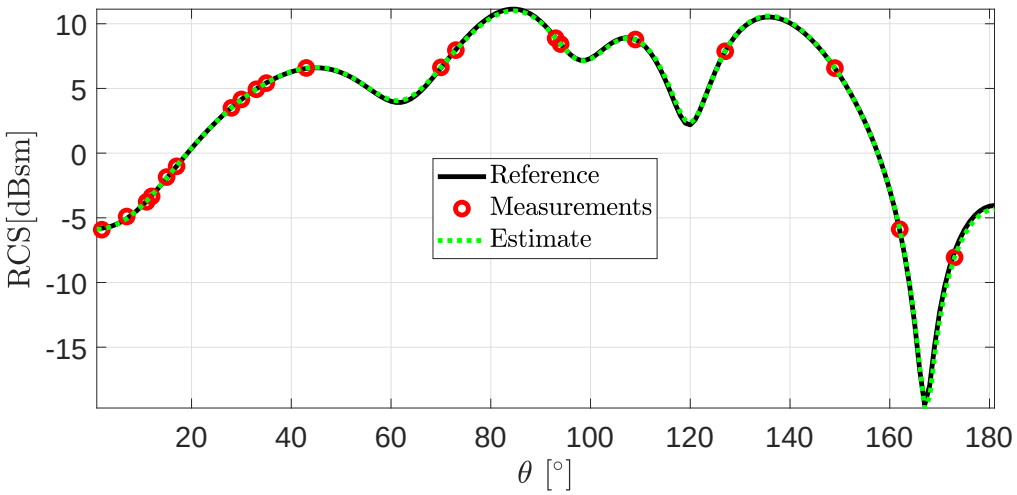

Figure 5.19: Scattering estimate from CMA-BSBL interpolation (20 random samples).

We note that the performance of the interpolation depends not only on the noise added to the measurements, but the location of the provided measurements as well. Intuitively, there is more uncertainty in the estimate of the target's current distribution if the provided measurements are not informative of the currents at

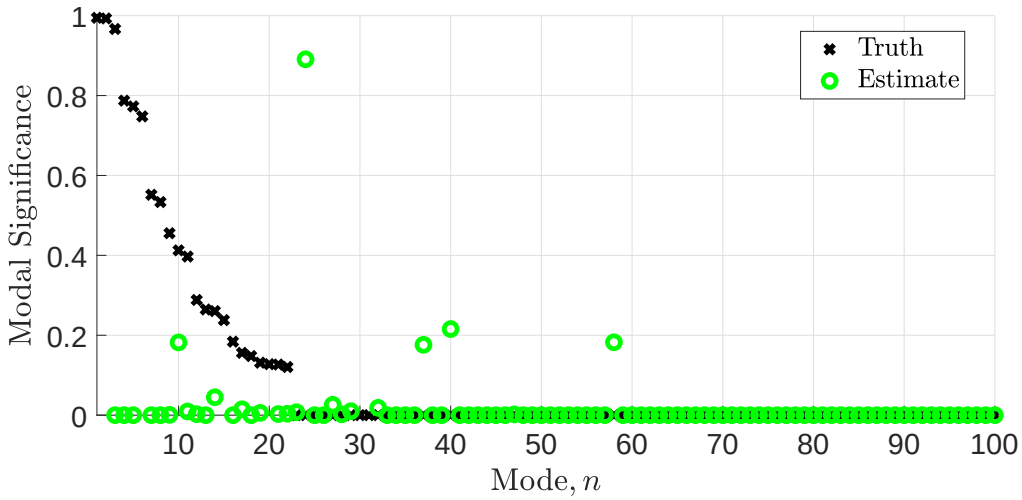

Figure 5.20: Modal significance estimate from CMA-BSBL interpolation (20 random samples).

certain aspect angles or locations. This can be seen in some of the trials where the random samples were in the less informative angles. While the sparse basis of characteristic currents is well suited to capture distributed scattering phenomena, there are limitations in how well it can perform where there are sharp discontinuities in the current distribution or in shadowed areas of the target.

Given this, it is clear that the extrapolation performance of the proposed scheme would be relatively limited when compared to the interpolation simulations. In our first extrapolation experiment, one contiguous half of the far-field data ($M = 91$ measurements from 0° to 90°) was provided to the BSBL solver. We also applied the extrapolation approach to the 1.2 GHz data where the current distribution has less oscillatory behavior (see Figure 5.3) and fewer modes will be necessary for adequate characterization.

The results shown in Figure 5.21 show that, even though an entire contiguous 90° sector is omitted, the approach is still capable of predicting the lobe centered at 130°. We note, however, that the variance of these estimates is significant — Figure 5.22

shows 50 trials of the simulation overlaid with the reference data. The plot indicates that, while the estimates of the current distribution are accurate enough to predict the remaining features in the signature between 91° and 180°, the approach is sensitive to the noise in the provided measurements and introduces significant variations in the extrapolated data.

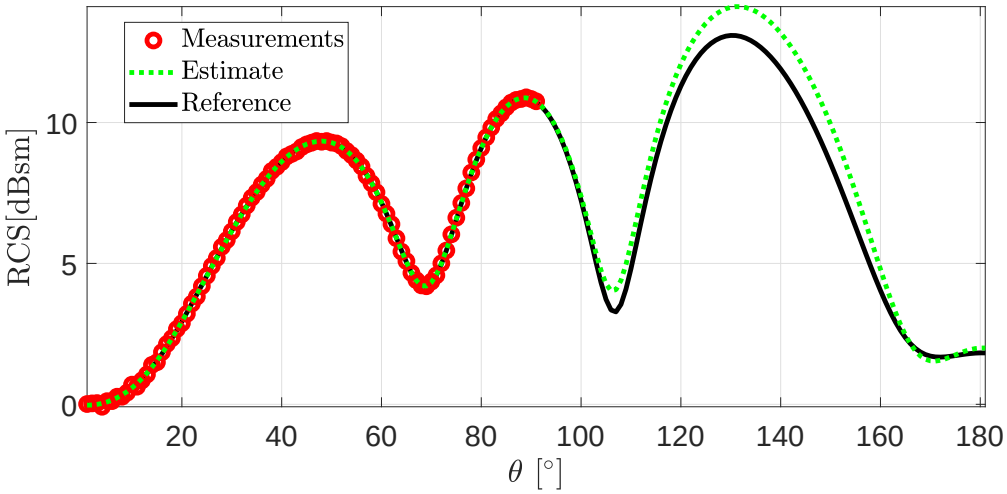

Figure 5.21: CMA-BSBL 1.2 GHz extrapolation ($0° - 90°$).

Finally, we show one additional extrapolation simulation, where we include multiple adjacent frequencies to the sparse solver. Using multiple frequencies in the extrapolation scheme may help the BSBL routine determine a more accurate sparse solution for $\mathbf{x}$. This is similar to the argument made in the previous interpolation scheme where we leverage the fact that adjacent frequencies will likely have the same set of significant modes (but the weights may be different). Therefore, we can enforce group sparsity across the adjacent frequencies such that a non-zero weight in one frequency will favor solutions where the mode is also non-zero in the other frequencies. We test this hypothesis by providing the solver $M = 121$ measurements uniformly spaced between 31° and 151° and extrapolate five frequencies between 1.9 and 2

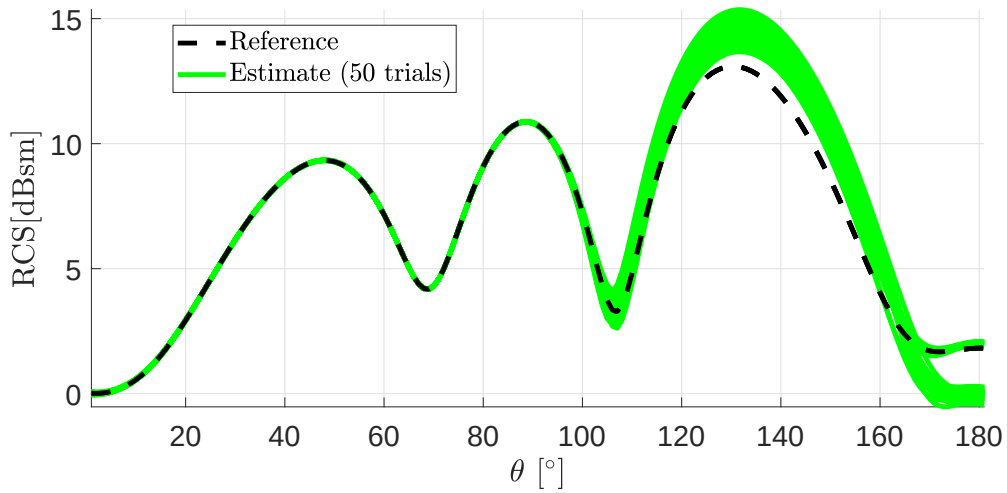

Figure 5.22: 50 trials of CMA-BSBL 1.2 GHz extrapolation ($0° - 90°$).

GHz. Ten trials of this simulation were performed and, for clarity, we focus on the performance of the extrapolation on the center frequency. Figures 5.23 and 5.24 qualitatively illustrates the reduction variance when five adjacent frequencies are used instead of one.

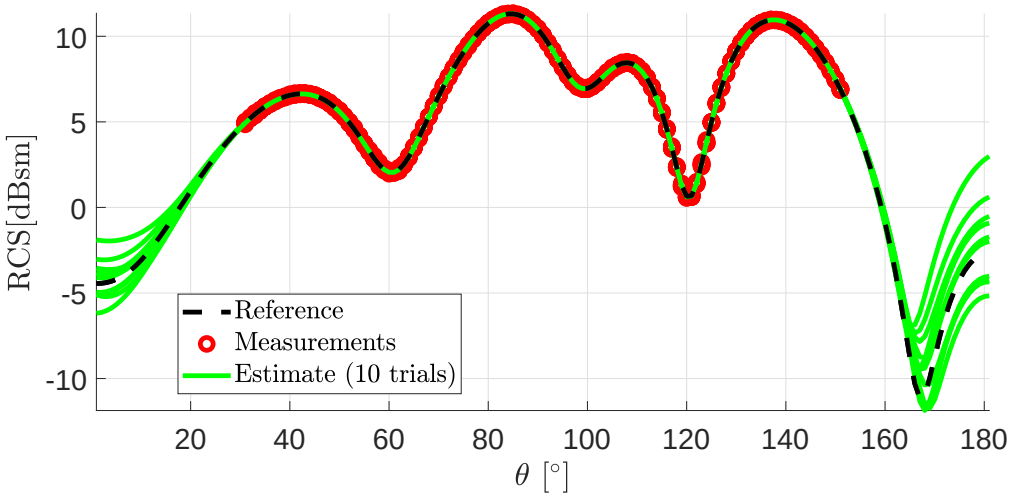

Figure 5.23: CMA-BSBL 1.95 GHz extrapolation over one frequency with measurements between $31° - 151°$.

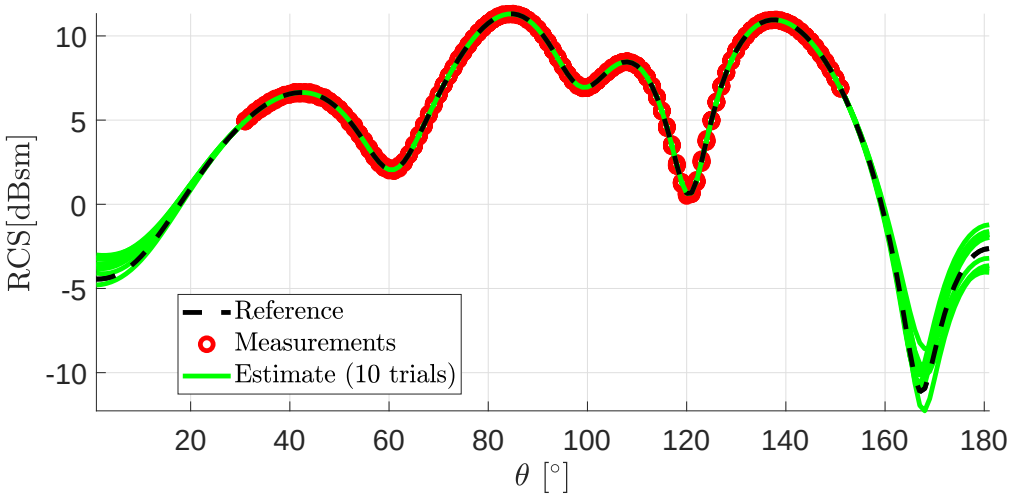

Figure 5.24: CMA-BSBL 1.95 GHz extrapolation over five frequencies with measurements between $31° - 151°$.

5.5 Areas for Future Investigation

Our experiments with CMA have thus far seen mixed results. While the theory presented in the literature is sound, our attempts to replicate the findings that were previously reported in the literature have had limited success. Applying the theory to a practical problem and investigating the feasibility of an interpolation scheme also revealed other practical limitations.

Clearly, there are issues with the implementation of CMA we are working with. In addition to the inconsistencies between the results reported in Bouche and our evaluations with two MOM-based codes, our attempt to replicate the results with an open source and freely available CMA code also required a significant offset to show agreement with the reference data. We believe that there is a normalization or constant factor that has been omitted from the computation. Future efforts should focus on identifying the root cause of this. Alternatively, we note that CMA has grown in popularity such that it is being supported as a feature in some

commercially available codes, including FEKO and HFSS. Leveraging commercially-developed codes may offer more quality assurance (but may also limit the flexibility since the source code is generally not available) and provide additional clarity on the applicability of CMA in scattering problems.

We also observed instances where the inclusion of additional modes in the reconstruction detrimentally affects the reconstruction. This behavior has not been explicitly identified in the literature, but some of the research that focuses on the applied and computational aspects of CMA offer some potential explanations of what we observed empirically. It would be prudent to generate predictions of other types of targets to see if this behavior is observed and to determine if they are caused by mesh discretization and/or numerical accuracy of the codes.

From our analysis, it is also clear that some modal tracking algorithm must be implemented in order to accurately reconstruct and interpolate scattering patterns over multiple frequencies, even for smaller targets where the eigenvalues vary smoothly. While our experiment only encompassed the NASA Almond target, it is reasonable to believe that other types of targets will have eigenvalues and modes that cross over each other or have slight oscillations that have significant impacts on the RCS reconstruction. Again, some commercially available codes may provide these features as well.

Of the two interpolation schemes we investigated, the second method that leveraged CMA as a sparse basis for BSBL holds the most promise. We have demonstrated that the method can accurately interpolate far-field RCS data using a very limited set of measurements and outperforms general interpolations methods. We also demonstrated that the scheme can provide reasonable extrapolation performance, especially when additional frequencies are solved with BSBL simultaneously.

While these simulation results are promising, this proof-of-concept also raises additional questions. Notably, in our CMA-BSBL investigation, we observed that sparsity can be synthetically satisfied by increasing the density of the mesh. The theory behind CMA simply states that a target discretized into N edges will have an $N \times N$ impedance matrix and can, theoretically, support N modes. It would be prudent to investigate how mesh density affects the interpolation and extrapolation performance.

Another open question is the extrapolation capabilities of CMA-BSBL. Because the method attempts to describe the currents on the body in order to generate scattering quantities, it is unclear whether the extrapolation can provide accurate estimates on other types of targets. For example, if a target has a significant scattering feature (e.g. a cavity), it would be helpful to characterize the extrapolation accuracy in several measurement configurations, such as having the cavity completely hidden from the measurements or to only provide shallow or grazing measurements to the sparse solver.

Additional extensions may include the application of the method to additional types of targets and to increase the frequencies of interest. Although beyond the scope of our current work, Harrington and his contemporaries have several papers the outlined the application of CMA to non-PEC objects [75–77]. Successful application of our interpolation scheme to these recent innovations in CMA may greatly expand the utility of out interpolation method.

VI. Conclusions

Through this document, we have investigated the concept of sparse basis representation of electromagnetic phenomena. We provided a review of the fundamental concepts behind sparse bases and how they are critical to a successful application of compressed sensing. We discussed the current state-of-the art with respect to Compressive Sensing (CS) formulations as well as the recent developments in their adoption into the electromagnetic community. We highlighted the confluence of CS and Machine Learning (ML) and the shift to leverage Bayesian inference to further enhance the utility of sparse bases in problems of interest to the electromagnetic community. We also recognized the limitations of sparse bases and the tendency for bases to be tailored for the class of problems at hand. From this body of knowledge, we identified three areas in which sparse bases and Bayesian inference may improve upon existing approaches.

In the first research area, we investigated the use of primitive-based scattering centers to augment isotropic point scatterers in Radar Cross Section (RCS) reconstruction. Our review of the literature revealed that methods to remove artifacts from RCS measurements rely heavily on the use of an overcomplete dictionary and an l_1-minimization routine to separate nuisance returns from the desired ones. While these dictionaries do not strictly adhere to the Restricted Isometry Property (RIP), they have shown to be very effective in this application. Critically, the performance of this approach requires the basis to be efficient in characterizing the scattering phenomena present in the measurements.

Until recently, the bases considered in this approach were developed to address several types of nuisance returns but the desired returns were characterized by the Isotropic Point Scatterer (IPS) basis exclusively. We hypothesized that specular

scattering from a target can be more efficiently represented by introducing non-isotropic scattering centers into the reconstruction process. Our contribution in this area explored the use of one such alternative basis, a Wedge Diffraction Primitive (WDP) derived from Geometrical Theory of Diffraction (GTD) and Uniform Theory of Diffraction (UTD) theory, to reduce the overall number of scattering centers that is required to represent the RCS of a target. Our simulations of a flat plate and an angled plate showed that a more accurate reconstruction is possible with the addition of the WDP basis, but requires a judicious placement of these points on the target. Future efforts may consider implementing an optimization approach to site these primitives prior to (or in parallel with) the l_1-minimization routine for RCS reconstruction.

Our process of implementing and evaluating the WDP revealed issues regarding shadowing on concave targets that introduced artificial discontinuities in the reconstruction results. Most of the IPS elements that contributed to the reconstruction were used to correct these discontinuities. More efficient representations of the RCS may be achieved if a dihedral basis were included in the overcomplete dictionary, as well. These findings were published in [9].

The second research area investigated the application of sparse bases in the Direction of Arrival (DOA) estimation problem. The extensive body of literature regarding DOA focused on refining subspace methods that were developed nearly fifty years ago. And yet, these methods still require a priori knowledge of the number of signals incident on the array to generate a DOA estimate. More recent literature appealed to CS approaches with the recognition that, in most applications, the DOA problem only considers a limited number of simultaneous signals within a large range of directions and is a naturally sparse problem.

Our contributions in this area focused on using two sparse methods, Bayesian Compressive Sensing (BCS) and Block-Sparse Bayesian Learning (BSBL), to generate

DOA estimates of multiple simultaneous incident signals with non-uniform antenna arrays. The key innovation in our treatment of this problem is to use orthogonalized basis vectors in lieu of the standard steering vectors to achieve a generalized method for DOA estimation with an arbitrarily configured array. With the steering vectors orthogonalized, each antenna in the array may have a unique non-isotropic gain pattern and can be in a non-uniformly spaced or aperiodic arrangement. This, in addition to the single-snapshot and blind estimation capabilities afforded by sparse methods in general, provides a flexible and robust approach to DOA estimation that addresses many of the limitations of existing approaches.

Using the proposed method, our numerical simulations showed that the group sparsity feature of BSBL significantly improved the accuracy of DOA estimates when compared to BCS. We demonstrated this effect with several notional arrays under multiple testing configurations that varied the number, direction and polarization of the incident signals to be estimated. The results of these simulations consistently indicate that this is a viable DOA technique that warrant additional investigation.

To further validate this approach, it would be prudent to explore its resiliency to more substantial levels of noise. Additionally, the range of element and array configurations can be expanded to further characterize the DOA estimation performance in multiple dimensions and possibly provide polarization estimates of the incoming signals, as well. These findings will be submitted for review to IEEE Sensors Letters.

The last research area explored the use of characteristic modes as another basis for RCS reconstruction in low frequency and/or electrically large scattering targets. Our review of the literature showed that the application of the Theory of Characteristic Modes (TCM) focused almost exclusively on radiation and antenna performance optimization. We reinterpreted the theoretical framework in the context

of electromagnetic scattering and attempted to verify TCM principles and apply the theory through two proposed interpolation schemes.

Due to limited resources, some of the discrepancies we discovered between the results from our implementation of Characteristic Mode Analysis (CMA) and results found in the literature were not completely rectified. Although we also found differences between the published results and our evaluations with two well-validated Method of Moments (MOM) codes, it is likely that a normalization factor was omitted from our implementation. It is very likely that a commercially-developed code with CMA capabilities would be in agreement with our MOM results. Therefore, any future efforts in this area will need to redress these discrepancies, either through tracing the root cause in our implementation or through the use of another code. Other inconsistencies were observed between the theory and our empirical results, such as spurious modes (which prevented monotonic improvements in the reconstruction accuracy) and discontinuities in the reconstructed results due to changes in the set of contributing significant modes.

With respect to the interpolation schemes, we saw limited success in the first approach, which attempted to generate RCS predictions by reusing the characteristic fields over multiple frequencies. It was determined that the change in phase in the characteristic fields had a cumulative effect that negatively impacted the accuracy of the interpolated results, especially at higher frequencies. One possible alternative is to interpolate the characteristic field (particularly the phase) data to generate a more accurate estimation of the phase at the interpolated frequency.

The second interpolation approach, which leverages the sparsity of the characteristic modes as a basis, showed much more promising results. Using the NASA Almond as the scattering target, we utilized the BSBL solver to generate a sparse solution of weights for each characteristic mode and to infer a current

distribution over the body with only a limited set of measurements. We observed excellent interpolation performance and the solver was able to accurately predict features in the signature that a standard, general-purpose interpolation algorithm would not. We also showed that extrapolation performance was reasonably effective, predicting general features in the RCS pattern, but was very sensitive to the noise in the provided measurements. Extrapolation performance can be further improved when multiple adjacent frequencies are solved simultaneously with BSBL solver.

To our knowledge, this is one of the first investigations into the use of characteristic modes as a sparse basis. While our preliminary investigation yielded new insights, they invariably provoked additional questions that merit further investigation. One of the more compelling questions to answer is the relationship between interpolation success and sparsity. Specifically, if sparsity can be satisfied by artificially increasing the density of the mesh, the utility of this interpolation approach may extend to scattering beyond the resonance region of a target. Additionally, implementing this interpolation approach with a CMA formulation that accommodates non-PEC materials would significantly broaden the scope of applicable scattering targets of interest.

It is clear from our efforts in the three thrust areas that there are many potential avenues for sparse bases to be applied to electromagnetics. While the fundamental tenets of CS may not always be rigorously satisfied, sparse bases and CS-derived solvers can still be quite effective in generating satisfactory solutions to relevant problems and are further improved when applied in the context of Bayesian inference. We maintain that the areas we have focused on have benefited from our contributions, raised compelling questions, and are burgeoning paths for continued development.

Appendix A: Scattering Primitives Based on an Approximation to Physical Optics Solutions

In another SAR application, [41] developed several canonical scattering models and pursued their use in target detection and feature extraction from three-dimensional bistatic measurements. The 3D canonical shapes, derived from 2D primitives, are analytic solutions that parameterized the high frequency scattering behavior of simple shapes, such as a flat plate and a dihedral, based on spatial properties (i.e., dimensions and orientation). The solutions from these formulas matched well against numeric solutions generated by a well-validated, industry standard Physical Optics (PO) solver. Because they provided an efficient means of replicating scattering behavior from elemental shapes, they seemed well suited as additional bases for the point scattering model described in the previous section.

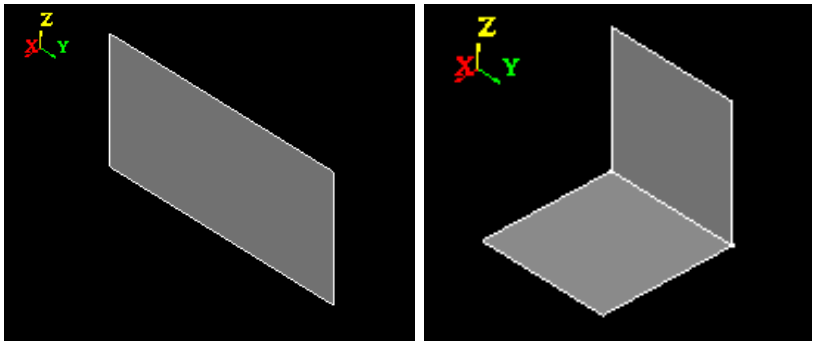

Figure A.1: Plate and Dihedral geometry.

To introduce directed scattering centers, an additional operation is applied to each of the scattering points in Equation (3.1)

$$S_{FF}^{pred}(k,\hat{r}) = \sum_{n} M\gamma_n e^{-j2k\hat{r}\cdot\vec{r}'}. \tag{A.1}$$

This is consistent with the model presented in [41] where the operator is a function of the incident field to the point, as well as the point's spatial parameters: location, dimensions and orientation. The operator, M, effectively modulates each scattering center according to its spatial properties and the incident field. For the complex primitives, the operator applies the monostatic form of the analytic solutions to the canonical shapes. Likewise, for isotropic scatterers, the operator is inactive and simply multiplies the point by a series of ones.

The simplest and most useful primitives (with respect to the types of targets we are interested in) were pursued first: the flat plate and the dihedral. The monostatic analytic solutions (approximates to the PO solutions) were formed by equating the transmit and receive angle pairs ($\theta_t = \theta_r$, $\phi_t = \phi_r$):

$$M_{flat} = \frac{jk}{\sqrt{\pi}} A\text{sinc}\left[kL\sin(\phi)\cos(\theta)\right]\text{sinc}\left[kH\sin(\theta)\right]; \theta = \left[-\frac{\pi}{2}, \frac{\pi}{2}\right], \phi = \left[-\frac{\pi}{2}, \frac{\pi}{2}\right]; A = LH \tag{A.2}$$

$$M_{dihedral} = \frac{jk}{\sqrt{\pi}} A\text{sinc}\left[kL\sin(\phi)\cos(\theta)\right] \times \begin{cases} \sin(\theta); \theta = \left[0, \frac{\pi}{4}\right] \\ \cos(\theta); \theta = \left[\frac{\pi}{4}, \frac{\pi}{2}\right] \end{cases}, \phi = \left[-\frac{\pi}{2}, \frac{\pi}{2}\right]; A = 2LH \tag{A.3}$$

where L and H are the length and height of the canonical scatters, respectively. In this form, the canonical shapes are oriented along the +x and +z axes (centered at the origin) and alternate poses of the primitives will need to have rotations applied to correct their scattering response. Translations of the primitives around the scene are handled via the differential range of the primitive to the phase center of the scene (origin).

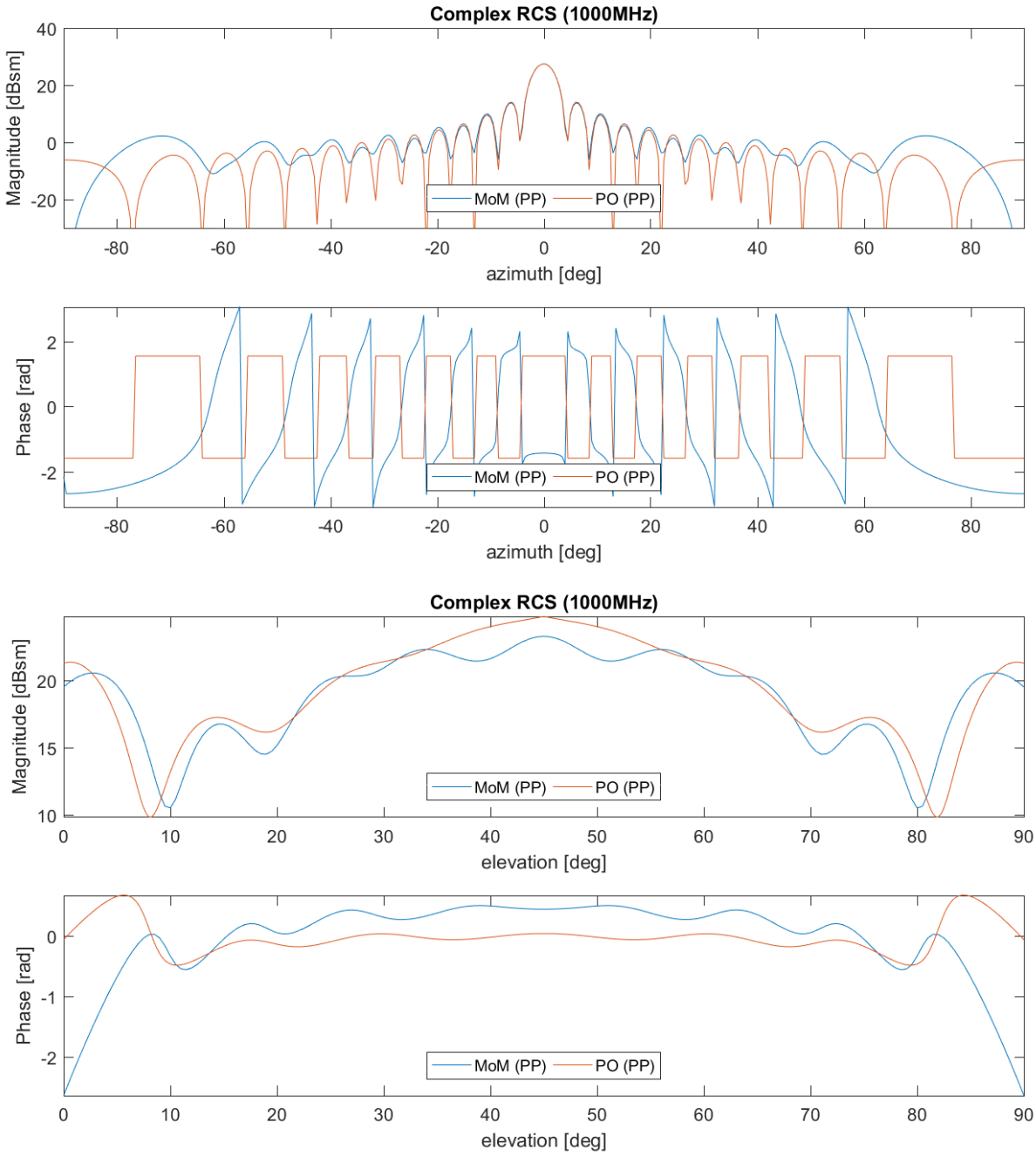

Figure A.2: MoM vs approximated PO solution of a 2×1 m plate at (top) and 1×1 m dihedral (bottom) at 1GHz, $\phi\phi$ polarization.

Appendix B: Non-Linear, Constrained Minimization of Primitive Spatial Parameters

The primary goal of the project is to determine a primitive-based representation of a complex scattering target. To that end, some a priori knowledge of the target is available and is used to generate a coarse representation of the target prior to making use of SPGL1 to recover the remaining discrepancies between the coarse predictions (σ_{prim}) and the measurements (σ_{truth}). One extension of this is to explore whether optimization can be applied to automatically site, pose, and dimension the complex primitives. In contrast to the SPGL1 process of determining a sparse solution of weights for a cloud of isotropically scattering points, the determination of the spatial parameters is not intuitively sparse (an argument was made in to exploit the Group Sparsity form of SPGL1 to site each primitive, but the other spatial parameters do not seem well suited for sparse representation). Therefore, we must appeal to another method of optimization. The most immediate solution would be to utilize the Optimization Toolbox for MATLAB, specifically the constrained nonlinear solver, *fmincon* [78]. We constrain the spatial parameters to reasonable ranges (a bounded region of where the primitive should be located, a limited range of feasible orientations, and a bound on each of the dimensions) to limit the extents of the search space as much as possible. We also provide the solver with the forward operator to map the parameter space to the space of far-field patterns. Lastly, we provide an objective function to the solver that provides a metric with which to evaluate solutions from the forward model against the measurement dataset. Unlike SPGL1, *fmincon* only requires the forward operator to converge to a solution.

We note that the solution space, unless highly constrained, will likely have many local minima and the solver may converge on one of these solutions rather than the

global minimum. Therefore, it is imperative to provide as small of a search space as possible and to seed the optimization with the best guess of where the solution should be in order for this minimization to succeed. This can be done by limiting the range of the parameters, as described above, as well as by providing a large set of measurements (frequencies and/or angles) to the solver. This will, ideally, allow the objective function to discriminate between solutions more easily (differences between the datasets will be more apparent when the datasets being compared at each iteration are large).

Bibliography

[1] "U.S. Air Force photo by Samuel King Jr./Released, Public domain, via Wikimedia Commons." https://upload.wikimedia.org/wikipedia/commons/2/2a/40th_Flight_Test_Squadron_F-16_Fighting_Falcon_sits_in_the_anechoic_chamber.jpg.

[2] R. G. Baraniuk, "Compressive sensing [lecture notes]," *IEEE Signal Processing Magazine*, vol. 24, no. 4, pp. 118–121, 2007.

[3] "Cylinder Cavity and Tube Measurements with and without RAM." Lab Exercise, EENG 627, Department of Electrical and Computer Engineering, Air Force Institute of Technology, Spring 2017.

[4] J. M. Gilmore, "Operational Test and Evaluation FY 2015 Annual Report," 2016. [Online.] Available: https://www.airforcemag.com/PDF/DocumentFile/Documents/2016/2015DOTEAnnualReport.pdf.

[5] A. Massa, P. Rocca, and G. Oliveri, "Compressive sensing in electromagnetics - A review," *IEEE Antennas and Propagation Magazine*, vol. 57, no. 1, pp. 224–238, 2015.

[6] I. Lahaie, M. Blischke, S. Cossmann, B. Fischer, and M. Hawks, "Model-Based optimization using l1 minimization for reducing the uncertainty in radar cross-section (RCS) measurements and predictions," *Proceedings of the 2017 19th International Conference on Electromagnetics in Advanced Applications, ICEAA 2017*, no. 1, pp. 840–843, 2017.

[7] B. Fischer, I. Lahaie, M. Hawks, and T. Conn, "On the Use of Basis Pursuit and a Forward Operator Dictionary to Separate Specific Background Types from

Target RCS Data," *AMTA 36th Annual Meeting and Symposium*, pp. 85–90, 2014.

[8] I. J. LaHaie, G. D. Dester, and M. H. Hawks, "An efficient basis for decomposition of cavity returns in inverse synthetic aperture radar (isar) measurements using basis pursuit," in *2019 International Conference on Electromagnetics in Advanced Applications (ICEAA)*, pp. 0563–0568, 2019.

[9] J. Lee, P. J. Collins, and J. A. Jackson, "Sparse Representation of Targets with Mixed Scattering Primitives," *Applied Computational Electromagnetics Society Journal*, vol. 35, no. 6, pp. 630–638, 2020.

[10] W. Dong, M. Diao, L. Gao, and L. Liu, "A low-complexity DOA and polarization method of polarization-sensitive array," *Sensors*, vol. 17, no. 5, 2017.

[11] R. K. Howell, "d-MUSIC, a real time algorithm for estimating the DOA of coherent sources using a single array snapshot," in *1999 IEEE International Conference on Acoustics, Speech, and Signal Processing*, vol. 5, pp. 2881–2884 vol.5, March 1999.

[12] Wong, Linshan Li, and Zoltowski, "Root-MUSIC-based direction-finding and polarization estimation using diversely polarized possibly collocated antennas," *IEEE Antennas and Wireless Propagation Letters*, vol. 3, pp. 129–132, 2004.

[13] M. Lin and L. Yang, "Blind calibration and DOA estimation with uniform circular arrays in the presence of mutual coupling," *IEEE Antennas and Wireless Propagation Letters*, vol. 5, pp. 315–318, 2006.

[14] C. El Kassis, J. Picheral, and C. Mokbel, "EM-ESPRIT Algorithm for direction finding with nonuniform arrays," in *2007 IEEE/SP 14th Workshop on Statistical Signal Processing*, pp. 453–457, Aug 2007.

[15] Y. Wu and H. C. So, "Simple and accurate two-dimensional angle estimation for a single source with uniform circular array," *IEEE Antennas and Wireless Propagation Letters*, vol. 7, pp. 78–80, 2008.

[16] J. Lin, X. Ma, S. Yan, and C. Hao, "Time-frequency multi-invariance ESPRIT for DOA estimation," *IEEE Antennas and Wireless Propagation Letters*, vol. 15, pp. 770–773, 2016.

[17] E. R. Ferrara and T. M. Parks, "Direction finding with an array of antennas having diverse polarizations," *IEEE Transactions on Antennas and Propagation*, vol. 31, no. 2, pp. 231–236, 1983.

[18] W. Fang, Y. Lee, and Y. Chen, "Maximum likelihood 2-d DOA estimation via signal separation and importance sampling," *IEEE Antennas and Wireless Propagation Letters*, vol. 15, pp. 746–749, 2016.

[19] M. J. Abedin and A. S. Mohan, "Maximum likelihood method for near-field parameter estimation using v-shaped antenna arrays," in *Asia-Pacific Microwave Conference 2011*, pp. 737–740, Dec 2011.

[20] A. Massa, P. Rocca, and G. Oliveri, "Compressive sensing in electromagnetics - a review," *IEEE Antennas and Propagation Magazine*, vol. 57, pp. 224–238, Feb 2015.

[21] R. J. Garbacz and R. H. Turpin, "A Generalized Expansion for Radiated and Scattered Fields," *IEEE Transactions on Antennas and Propagation*, vol. 19, no. 3, pp. 348–358, 1971.

[22] Y. C. Eldar and G. Kutyniok, *Compressed Sensing: Theory and Applications*. Cambridge university press, 2012.

[23] S. Foucart and H. Rauhut, *A Mathematical Introduction to Compressive Sensing*. Applied and Numerical Harmonic Analysis, New York, NY: Springer New York, 2013.

[24] E. J. Candes and T. Tao, "Decoding by linear programming," *IEEE Transactions on Information Theory*, vol. 51, no. 12, pp. 4203–4215, 2005.

[25] D. L. Donoho, "Compressed sensing," *IEEE Transactions on information theory*, vol. 52, no. 4, pp. 1289–1306, 2006.

[26] M. F. Duarte, M. A. Davenport, D. Takhar, J. N. Laska, T. Sun, K. F. Kelly, and R. G. Baraniuk, "Single-pixel imaging via compressive sampling," *IEEE signal processing magazine*, vol. 25, no. 2, pp. 83–91, 2008.

[27] R. Baraniuk and P. Steeghs, "Compressive radar imaging," *IEEE National Radar Conference - Proceedings*, no. April, pp. 128–133, 2007.

[28] L. Carin, D. Liu, and Y. Xue, "In situ compressive sensing," in *2007 2nd IEEE International Workshop on Computational Advances in Multi-Sensor Adaptive Processing*, pp. 105–108, 2007.

[29] K. Aberman and Y. C. Eldar, "Sub-nyquist sar via fourier domain range-doppler processing," *IEEE Transactions on Geoscience and Remote Sensing*, vol. 55, no. 11, pp. 6228–6244, 2017.

[30] Y. Arjoune, N. Kaabouch, H. El Ghazi, and A. Tamtaoui, "Compressive sensing: Performance comparison of sparse recovery algorithms," *2017 IEEE 7th Annual Computing and Communication Workshop and Conference, CCWC 2017*, 2017.

[31] S. Ament, "CS6220 Lecture Notes : Basis Pursuit De-noising , LASSO , and Compressed Sensing." Lecture Notes, 2017.

[32] D. L. Donoho, "For most large underdetermined systems of linear equations the minimal l_1-norm solution is also the sparsest solution," *Comm. Pure Appl. Math.*, vol. 59, no. 6, pp. 797–829, 2006.

[33] E. van den Berg and M. P. Friedlander, "Probing the pareto frontier for basis pursuit solutions," *SIAM Journal on Scientific Computing*, vol. 31, no. 2, pp. 890–912, 2008.

[34] E. van den Berg and M. P. Friedlander, "SPGL1: A solver for large-scale sparse reconstruction," December 2019. https://friedlander.io/spgl1.

[35] J. Romberg, "L1-magic," 2005. [Online.] Available: https://statweb.stanford.edu/~candes/l1magic/.

[36] M. S. Andersen, J. Dahl, and L. Vandenberghe, "CVXOPT: Python Software for Convex Optimization," Apr 2020. https://cvxopt.org/index.html.

[37] Y. Zhang and W. Yin, "Rice University, L1-Related Optimization Project." https://www.caam.rice.edu/~optimization/L1/2007/09/software_08.html.

[38] A. Massa and F. L. Teixeira, "Guest editorial: Special cluster on compressive sensing as applied to electromagnetics," *IEEE Antennas and Wireless Propagation Letters*, vol. 14, pp. 1022–1026, 2015.

[39] M. Tipping, "Sparse Bayesian Learning and the Relevance Vector Mach," *Journal of Machine Learning Research*, vol. 1, pp. 211–244, 2001.

[40] J. A. Jackson, *Three-dimensional feature models for synthetic aperture radar and experiments in feature extraction.* PhD thesis, The Ohio State University, 2009.

[41] J. A. Jackson, B. D. Rigling, and R. L. Moses, "Canonical scattering feature models for 3D and bistatic SAR," *IEEE Transactions on Aerospace and Electronic Systems*, vol. 46, no. 2, pp. 525–541, 2010.

[42] G. B. Hammond and J. A. Jackson, "SAR canonical feature extraction using molecule dictionaries," *IEEE National Radar Conference - Proceedings*, no. 1, 2013.

[43] K. R. Varshney, M. Çetin, J. W. Fisher, and A. S. Willsky, "Sparse Representation in Structured Dictionaries With Application to Synthetic Aperture Radar," *IEEE Transactions on Signal Processing*, vol. 56, no. 8, pp. 3548–3561, 2008.

[44] M. Carlin, P. Rocca, G. Oliveri, F. Viani, and A. Massa, "Directions-of-Arrival Estimation Through Bayesian Compressive Sensing Strategies," *IEEE Transactions on Antennas and Propagation*, vol. 61, no. 7, pp. 3828–3838, 2013.

[45] M. E. Tipping, "Bayesian inference: An introduction to principles and practice in machine learning," *Advanced Lectures on Machine Learning*, pp. 1–19, 2004.

[46] S. Ji, Y. Xue, and L. Carin, "Bayesian Compressive Sensing papers," *IEEE Transactions on Signal Processing*, vol. 56, no. 6, pp. 2346–2356, 2008.

[47] Z. Zhang and B. D. Rao, "Extension of SBL algorithms for the recovery of block sparse signals with intra-block correlation," *IEEE Transactions on Signal Processing*, vol. 61, pp. 2009–2015, April 2013.

[48] B. Li, W. Bai, G. Zheng, X. He, B. Xue, and M. Zhang, "BSBL-based DOA and polarization estimation with linear spatially separated polarization sensitive array," *Wireless Personal Communications*, vol. 109, no. 3, pp. 2051–2065, 2019.

[49] H. Lee and R. Stovall, "Maximum likelihood methods for determining the direction of arrival for a single electromagnetic source with unknown polarization," *IEEE Transactions on Signal Processing*, vol. 42, pp. 474–479, Feb 1994.

[50] Y. Chen and C.-F. Wang, *Characteristic Modes*. Hoboken, NJ: John Wiley & Sons, Inc, jun 2015.

[51] R. F. Harrington and J. R. Mautz, "Theory of Characteristic Modes for Conducting Bodies," *IEEE Transactions on Antennas and Propagation*, vol. 19, no. 5, pp. 622–628, 1971.

[52] D. Bouche, F. Collino, Y. Morel, and O. Vacus, "Characteristic current decomposition and radar cross-section analysis for perfectly electrically conducting bodies," *IMA Journal of Numerical Analysis*, vol. 35, no. 1, pp. 454–477, 2013.

[53] A. Paulraj, B. Ottersten, R. Roy, A. Swindlehurst, G. Xu, and T. Kailath, "Subspace methods for directions-of-arrival estimation," *Handbook of Statistics*, vol. 10, pp. 693–739, 1993.

[54] Z. Liu, "DOA and polarization estimation via signal reconstruction with linear polarization-sensitive arrays," *Chinese Journal of Aeronautics*, vol. 28, no. 6, pp. 1718–1724, 2015.

[55] S. Ji, Y. Xue, and L. Carin, "Bayesian compressive sensing," *IEEE Transactions on Signal Processing*, vol. 56, pp. 2346–2356, June 2008.

[56] R. Wei, Q. Wang, and Z. Zhao, "Two-dimensional DOA estimation based on separable observation model utilizing weighted l1-norm penalty and Bayesian compressive sensing strategy," in *2017 4th International Conference on Information Science and Control Engineering (ICISCE)*, pp. 1764–1768, July 2017.

[57] L. Xi, S. Fangfang, Z. Guanghui, and S. Guangming, "Low complexity DOA estimation approach through multitask Bayesian compressive sensing strategies," in *2015 IEEE International Conference on Signal Processing, Communications and Computing (ICSPCC)*, pp. 1–4, Sep. 2015.

[58] Y. Pan, N. Tai, S. Cheng, and N. Yuan, "Joint estimation of DOA and mutual coupling via block sparse Bayesian learning," in *2015 IEEE International Conference on Signal Processing, Communications and Computing (ICSPCC)*, pp. 1–6, Sep. 2015.

[59] H. Cui, H. Duan, and H. Liu, "Off-grid DOA estimation using temporal block sparse Bayesian inference," in *2016 IEEE International Conference on Digital Signal Processing (DSP)*, pp. 204–207, Oct 2016.

[60] P. Rocca, M. A. Hannan, M. Salucci, and A. Massa, "Single-snapshot DoA estimation in array antennas with mutual coupling through a multiscaling BCS strategy," *IEEE Transactions on Antennas and Propagation*, vol. 65, no. 6, pp. 3203–3213, 2017.

[61] S. Ji, D. Dunson, and L. Carin, "Multitask compressive sensing," *IEEE Transactions on Signal Processing*, vol. 57, no. 1, pp. 92–106, 2009.

[62] Q. Wu, Y. D. Zhang, M. G. Amin, and B. Himed, "Complex multitask Bayesian compressive sensing," *ICASSP, IEEE International Conference on Acoustics, Speech and Signal Processing - Proceedings*, pp. 3375–3379, 2014.

[63] MathWorks, "Antenna Toolbox," Dec. 2019. https://www.mathworks.com/help/antenna/index.html.

[64] B. Halder and T. Kailath, "Efficient estimation of closely spaced sinusoidal frequencies using subspace-based methods," *IEEE Signal Processing Letters*, vol. 4, pp. 49–51, Feb 1997.

[65] M. Hawes, L. Mihaylova, F. Septier, and S. Godsill, "Bayesian compressive sensing approaches for direction of arrival estimation with mutual coupling effects," *IEEE Transactions on Antennas and Propagation*, vol. 65, pp. 1357–1368, March 2017.

[66] H. Gazzah, "Optimum antenna arrays for isotropic direction finding," *IEEE Transactions on Aerospace and Electronic Systems*, vol. 47, no. 2, pp. 1482–1489, 2011.

[67] K. F. Warnick, ed., *Numerical Methods for Engineering: An Introduction using MATLAB® and Computational Electromagnetics Examples*. Electromagnetic Waves, Institution of Engineering and Technology, 2011.

[68] A. C. Woo, M. J. Schuh, M. L. Sanders, H. T. Wang, and J. L. Volakis, "Benchmark Radar Targets for the Validation of Computational Electromagnetics Programs," *IEEE Antennas and Propagation Magazine*, vol. 35, no. 1, pp. 84–89, 1993.

[69] Z. T. Miers, "Characteristic modes matlab software," October 2015. https://www.characteristicmodes.org/software/.

[70] R. F. Harrington and J. R. Mautz, "Computation of Characteristic Modes for Conducting Bodies," *IEEE Transactions on Antennas and Propagation*, vol. 19, no. 5, pp. 629–639, 1971.

[71] S. Morvan and O. Vacus, "RCS analysis and classification in the Low Frequency domain," *2014 International Radar Conference, Radar 2014*, no. 1, pp. 5–8, 2014.

[72] M. Capek, P. Hamouz, P. Hazdra, and J. Eichler, "Implementation of the Theory of Characteristic Modes in MATLAB," *IEEE Antennas and Propagation Magazine*, vol. 55, no. 2, pp. 176–189, 2013.

[73] M. Capek, V. Losenicky, L. Jelinek, and M. Gustafsson, "Validating the Characteristic Modes Solvers," *IEEE Transactions on Antennas and Propagation*, vol. 65, no. 8, pp. 4134–4145, 2017.

[74] M. Masek, M. Capek, L. Jelinek, and K. Schab, "Modal tracking based on group theory," *IEEE Transactions on Antennas and Propagation*, vol. 68, no. 2, pp. 927–937, 2020.

[75] R. Harrington, J. Mautz, and Yu Chang, "Characteristic modes for dielectric and magnetic bodies," *IEEE Transactions on Antennas and Propagation*, vol. 20, no. 2, pp. 194–198, 1972.

[76] F. Hu and C. Wang, "Integral equation formulations for characteristic modes of dielectric and magnetic bodies," *IEEE Transactions on Antennas and Propagation*, vol. 64, no. 11, pp. 4770–4776, 2016.

[77] H. Alroughani, J. L. T. Ethier, and D. A. McNamara, "Observations on computational outcomes for the characteristic modes of dielectric objects," in *2014 IEEE Antennas and Propagation Society International Symposium (APSURSI)*, pp. 844–845, 2014.

[78] "MATLAB: Optimization Toolbox (fmincon)." [Online.] Available: https://www.mathworks.com/help/optim/ug/fmincon.html.

REPORT DOCUMENTATION PAGE

Form Approved
OMB No. 0704–0188

1. REPORT DATE *(DD–MM–YYYY)*	2. REPORT TYPE	3. DATES COVERED *(From — To)*
24–12–2020	Doctoral Dissertation	Oct 2016–Dec 2020

4. TITLE AND SUBTITLE

Sparse Bases and Bayesian Inference of Electromagnetic Scattering

5a. CONTRACT NUMBER

5b. GRANT NUMBER

5c. PROGRAM ELEMENT NUMBER

6. AUTHOR(S)

Lee, John, Contractor, Riverside Research

5d. PROJECT NUMBER

5e. TASK NUMBER

5f. WORK UNIT NUMBER

7. PERFORMING ORGANIZATION NAME(S) AND ADDRESS(ES)

Air Force Institute of Technology
Graduate School of Engineering and Management (AFIT/EN)
2950 Hobson Way
WPAFB, OH 45433-7765

8. PERFORMING ORGANIZATION REPORT NUMBER

AFIT-ENG-DS-20-D-010

9. SPONSORING / MONITORING AGENCY NAME(S) AND ADDRESS(ES)

N/A

10. SPONSOR/MONITOR'S ACRONYM(S)

N/A

11. SPONSOR/MONITOR'S REPORT NUMBER(S)

12. DISTRIBUTION / AVAILABILITY STATEMENT
DISTRIBUTION A. Approved for public release: distribution unlimited.

13. SUPPLEMENTARY NOTES
This work is declared a work of the U.S. Government and is not subject to copyright protection in the United States.

14. ABSTRACT
Many approaches in CEM rely on the decomposition of complex radiation and scattering behavior with a set of basis vectors. Accurate estimation of the quantities of interest can be synthesized through a weighted sum of these vectors. In addition to basis decompositions, sparse signal processing techniques developed in the CS community can be leveraged when only a small subset of the basis vectors are required to sufficiently represent the quantity of interest. We investigate several concepts in which novel bases are applied to common electromagnetic problems and leverage the sparisty property to improve performance and/or reduce computational burden.

The first concept explores the use of multiple types of scattering primitives to reconstruct scattering patterns of electrically large targets. Using a combination of isotropic point scatterers and wedge diffraction primitives as our bases, a 40% reduction in reconstruction error can be achieved.

Next, a sparse basis is used to improve DOA estimation. We implement the BSBL technique to determine the angle of arrival of multiple incident signals with only a single snapshot of data from an arbitrary arrangement of non-isotropic antennas. This is an improvement over the current state-of-the-art, where restrictions on the antenna type, configuration, and a priori knowledge of the number of signals are often assumed.

Lastly, we investigate the feasibility of a basis set to reconstruct the scattering patterns of electrically small targets. The basis is derived from the TCM and can capture non-localized scattering behavior. Preliminary results indicate that this basis may be used in an interpolation and extrapolation scheme to generate scattering patterns over multiple angles.

15. SUBJECT TERMS
Bayesian Compressive Sensing, inverse scattering, Characteristic Moda Analysis

16. SECURITY CLASSIFICATION OF:			17. LIMITATION OF ABSTRACT	18. NUMBER OF PAGES	19a. NAME OF RESPONSIBLE PERSON
a. REPORT	b. ABSTRACT	c. THIS PAGE			Dr. Peter J. Collins (ENG)
U	U	U	Distribution A	130	19b. TELEPHONE NUMBER *(include area code)* (937) 255-3636 x7256 Peter.Collins@afit.edu